STUDIES OF PZT/EPOXY AND PMN-PT/EPOXY COMPOSITES FOR ULTRASONIC TRANSDUCER APPLICATIONS

CHENG KEI CHUN

M. PHIL.

THE HONG KONG
POLYTECHNIC UNIVERSITY

2000

STUDIES OF PZT/EPOXY AND PMN-PT/EPOXY COMPOSITES FOR ULTRASONIC TRANSDUCER APPLICATIONS

SUBMITTED BY

CHENG KEI CHUN

FOR THE DEGREE OF

MASTER OF PHILOSOPHY IN PHYSICS

AT

THE HONG KONG POLYTECHNIC UNIVERSITY

AUGUST 2000

ABSTRACT

Two piezoelectric materials, lead zirconate titanate (PZT) and lead magnesium niobate-lead titanate (PMN-PT), have been characterized by using the resonance method and laser interferometry. PMN-PT (with 0.33PT) single crystal is an important new piezoelectric material for ultrasonic transducer and actuator applications. The stiffness constants and piezoelectric coefficients of PMN-PT are important parameters which have been measured in the present work. These are essential data if the crystal is to be used in device fabrication, but some of them are presently not available in the literature.

Two types of composites have also been studied in this work:

1. Ring-shaped PZT/epoxy composites have been produced for fabricating Langevin sandwich-type transducers for high power ultrasonic applications, e.g. in the driver of an ultrasonic wire bonding transducer. The composites were prepared by a dice-and-fill technique in which poled PZT rings were cut in different patterns using a diamond saw. The grooves in the ceramic were filled with epoxy. Four composite rings were bolted together between two metal front and back plates to form the sandwich transducer. The performances of these composite transducers were characterized. It was found that the use of composite rings instead of ceramic rings in the sandwich transducer could eliminate the coupling of radial modes to the useful axial mode, thereby increaseing significantly the efficiency of the transducer. The composites have lower

mechanical quality factor and the transducer fabricated using these rings have broader bandwidth. A US patent has been filed based on this work.

2. PMN-PT single crystals are reported to have very high electromechanical coupling factor k_{33} (> 90%) compared to PZT (k_{33} ~ 60%). In order to exploit the advantage of the extra-high k_{33} of the crystal, a 1-3 PMN-PT/epoxy composite which PMN-PT rods embedded in an epoxy matrix has been fabricated by the dice-and-fill technique. Original results on the study of the coarsely-diced 1-3 PMN-PT/epoxy composite have been obtained and reported in this thesis.

ACKNOWLEDGEMENTS

I would like to thank my chief supervisor, Prof. H.L.W. Chan, and co-supervisor, Prof. C.L. Choy, for their constant guidance, support and patience throughout the course of the research work, and for established the project which I found interested and useful.

I would also like to extend special thanks to Dr. Q.F. Zhou, Dr. G.R. Li, Dr. J.H. Hu, Mr. D.M. Lei, Dr. K.W. Kwok and Dr. K.H. Pang for their helpful supports and suggestions.

Thanks are also due to good friends including (in no particular order) Mr. W.Y. Ng, Dr. Beatrix Ploss, Dr. N. Chong, Mr. Marcos Lam, Mr. Koko Lam, Mr. K.W. Tang, Mr. H.L. Li, Miss Mable Tsang and Miss Wendy Fung for their constant encouragement.

I gratefully acknowledged the financial support from the Industrial Support Fund (ISF, AF 147/98). Last, but not least, I would like to express my great appreciation to my family for their constant support and encouragement during the research study.

TABLE OF CONTENTS

LIST OF FIGURE CAPTIONS

page

LIST OF TABLE CAPTIONS

page

LIST OF SYMBOLS

Symbol	Description	SI unit
f_r	resonance frequency	Hertz
f_a	anti-resonance frequency	Hertz
ρ	density	kg/meter^3
σ	planar Poisson's ratio	
ω	angular frequency	Hertz
k_p	planar electromechanical coupling factor	
k_{31}	transverse electromechanical coupling factor	
k_{33}	longitudinal electromechanical coupling factor	
k_t	thickness electromechanical coupling factor	
k_{15}	shear electromechanical coupling factor	
Q_M	mechanical quality factor	
$\tan\delta=1/Q_E$	dissipation factor at 1 kHz	
d_{ip}	piezoelectric charge coefficient	meter/Volt or coulomb/Newton
d_h	hydrostatic charge coefficient	meter/Volt or coulomb/Newton
g_{ip}	piezoelectric voltage coefficient	Volt meter/Newton meter^2/coulomb
e_{ip}	piezoelectric coefficient	coulomb/meter^2
h_{ip}	piezoelectric coefficient	Volt/meter or Newton/coulomb
c_{ip}^E	elastic stiffness constant at constant electric field	Newton/meter^2
c_{ip}^D	elastic stiffness constant at constant charge density	Newton/meter^2
s_{ip}^E	elastic compliance at constant electric field	meter^2/Newton
s_{ip}^D	elastic compliance at constant charge density	meter^2/Newton
N_1	transverse frequency constant	Hertz-meter
N_3	longitudinal frequency constant	Hertz-meter

N_t	thickness frequency constant	Hertz-meter
ε_0	dielectric constant of free space	Farad/meter
ε_{ip}^T	relative dielectric constant at free condition	Farad/meter
ε_{ip}^S	relative dielectric constant at clamped condition	Farad/meter
G	shear modulus	Newton/meter^2
Y	Young's modulus	Newton/meter^2
K	bulk modulus	Newton/meter^2
Z_L	longitudinal acoustic impedance	rayl
Z_S	shear acoustic impedance	rayl
P_v	percentage variation	percent
Z	electrical impedance	ohm
Z_m	minimum electrical impedance	ohm
θ	phase angle	degree
v_L	longitudinal wave velocity	meter/second
v_S	shear wave velocity	meter/second
v_{oil}	velocity of oil	meter/second
d_{inner}	inner diameter of a ring	meter
d_{outer}	outer diameter of a ring	meter
d_{mr}	mean diameter of a ring	meter
w_r	wall thickness of a ring	meter
τ_r	thickness of a ring	meter
$f_{r\text{-}thk}$	thickness resonant frequency of a ring	Hertz
$f_{r\text{-}rad}$	radial resonant frequency of a ring	Hertz
$f_{r\text{-}wall}$	wall thickness resonant frequency of a ring	Hertz
f_t	thickness resonant frequency of a disc	Hertz
f_p	planar resonant frequency of a disc	Hertz
f_s	stopband resonant frequencies of a 1-3 composite disc	Hertz
f_L	lateral resonant frequencies of a 1-3 composite disc	Hertz
R_{d2t}	Ratio of mean diameter d_{mr} of ring to thickness	
R_{w2t}	Ratio of wall thickness w_r of ring to thickness	

CHAPTER 1

INTRODUCTION

1.1 Background

Piezoelectric activity was first discovered in single crystals such as quartz, Rochelle salt, and tourmaline by Jacques and Pierre Curie in 1880 [Jaffe, 1971]. It was not until 1946 that scientists discovered that barium titanate ($BaTiO_3$) and lead zirconate titanate (PZT) ceramics exhibited piezoelectric effect [Jaffe, 1971]. In the direct piezoelectric effect, polarization charges are induced in response to an external mechanical stress, whereas in the converse piezoelectric effect, a dimensional change results from an applied electric field.

Piezoelectric materials such as lead zirconate titanate (PZT) have been used to fabricate ultrasonic transducers since the 1940's for use in underwater acoustics, non-destructive testing, medial diagnostics, welding etc [Tanaka, 1982]. PZT has been widely utilized for many years due to its high electromechanical coupling factor (k_{33} ~60%) and high d_{33} coefficient (from 75 to 600 pC/N) [Igarashi, 1982]. However, with a breakthrough in relaxor-based ferroelectric single crystals such as lead magnesium niobate-lead titanate (PMN-PT) and lead zinc niobate-lead titanate (PZN-PT) developed since 1981 [Shrout, 1990], the single crystals show promising potentials to be used in device applications [Park, 1997]. It was found that the single

crystals exhibit an extraordinary large electromechanical coupling coefficient (k_{33}>90%) and piezoelectric coefficient (d_{33}>2000 pC/N) [Geng, 1998; Yin, 1999]. In addition, their electrical loss is small (<0.005) [Yin, 2000]. These superior properties of the novel materials allow the design of higher sensitivity ultrasonic transducers with broadband characteristics for medical diagnostic imaging applications and for large strain actuators .

However, both PZT and the single crystals have two main drawbacks [Smith, 1986] for medical imaging and hydrophone applications. First, their acoustic impedance ($Z=\rho\cdot\upsilon$), where ρ is the density and υ is velocity of sound, are very large (> 20 Mrayl) compared to that of water or human tissue (~1.5 Mrayl), leading to insufficient energy coupling to these media. Another drawback is that the hydrostatic piezoelectric coefficient d_h is also small due to $d_{33} \sim 2d_{31}$. Small d_h indicates a poor sensitivity of receiving under hydrostatic pressure. To improve these two problems, a number of different types of composites using piezoelectric materials and polymer have been developed (Fig. 1.1) [Gururaja, 1985; Newnham, 1990] and some typical composites (e.g. 1-3, 0-3, 2-2, 3-3) have been fabricated by other workers. [Meyer, 1997; Chan, 1998; Ritter, 1998; Creedon, 1994]. Since polymer such as epoxy to be used in this work has very low relative dielectric constant ($\varepsilon \sim 4$) and low acoustic impedance (Z ~ 4 Mrayl). A ceramic/polymer composite has ε and Z much lower than that of ceramic to facilitate energy transfer [Chan, 1989]. Composites can also be tailored through varying the piezoelectric ceramic volume fractions and their

spatial distributions, and the connectivity [Gururaja, 1987] to obtain the optimized properties to meet the needs of different kinds of ultrasonic applications.

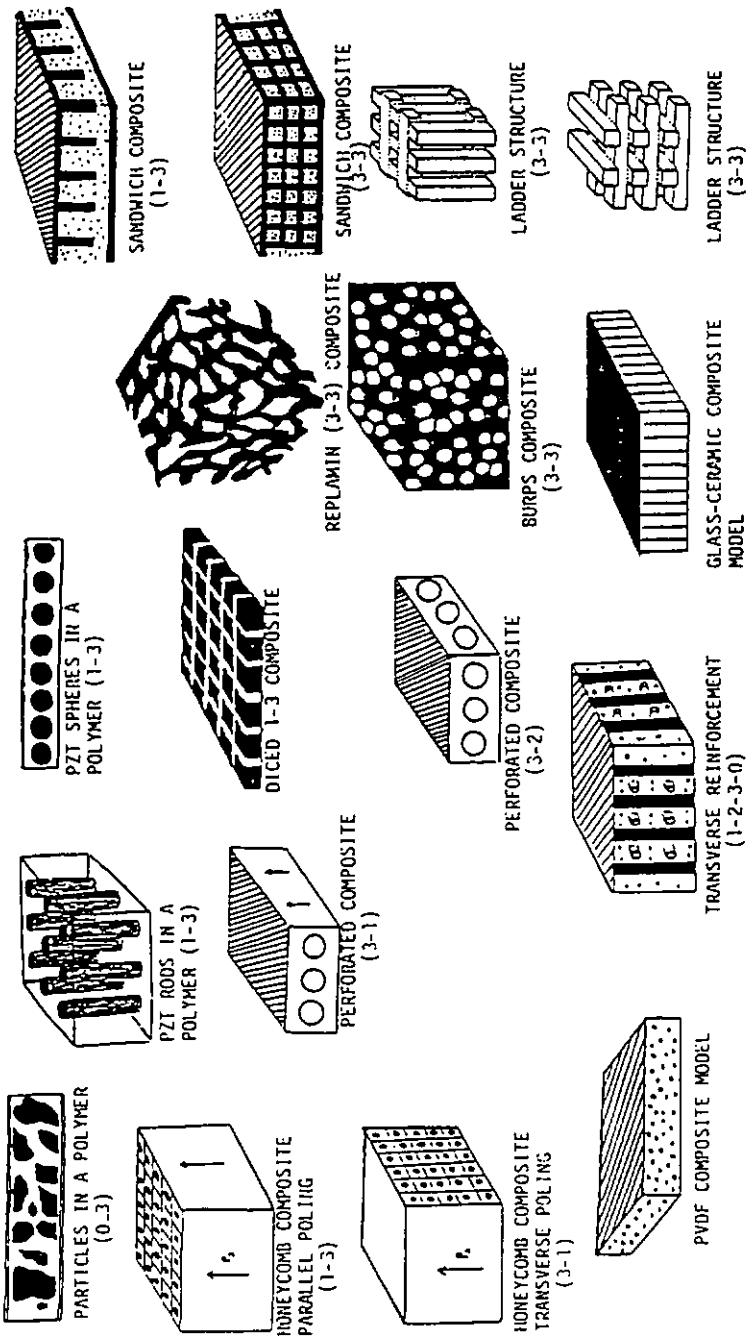

Fig. 1.1 Schematic diagram of various types of composites with different connectivity. [Gururaja, 1987]

1.1.1 A PMN-PT/epoxy composite for medical applications

A 1-3 composite consists of piezoelectric rods embedded in a polymer matrix (Fig. 1.2). The Origin of the name "1-3" is due to the connectivity that is defined by the manner in which the individual phases are interconnected [Newnham, 1990]. 1 stands for the piezoelectric phase which is connected in one dimension while the polymer is 3 dimensionally connected [Newnham, 1990]. Among the 17 composite patterns in Fig. 1.1, a 1-3 composite has attracted considerable interest [Kwok, 1999; Hayward, 1996; Gururaja, 1985] as it can allow pure thickness mode operation with the advantages of having to higher electromechanical coupling (up to k_{33}). A highly efficient material used in ultrasonic transducer applications, should have high electromechanical coupling of the material as it represents the efficiency in conversion between electrical and mechanical energy. The 1-3 composite also provides a broader bandwidth and lower planar mode-coupling coefficient compared to a piezoceramic which are beneficial in some transducer systems. Furthermore, the 1-3 composite can easily be fabricated by a dice and fill technique to be described in Chapter 2.

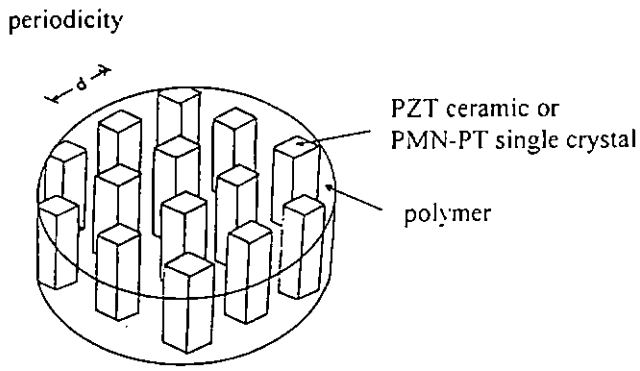

Fig. 1.2 Schematic diagram of a 1-3 composite.

In order to utilize the advantage of the extrahigh k_{33} of PMN-PT single crystal, a 1-3 PMN-PT /epoxy composite is fabricated and characterized in this work. This is an original work which has not been reported yet in the literature. In addition, the single crystal PMN-0.33PT used in this work is a new material and its material properties have to be evaluated in order to optimize properties for future applications. Making use of the unique properties of 1-3 composites, transducers with better performance can be produced for use in medical diagnosis and non-destructive testing applications.

1.1.2 PZT/epoxy composite transducers for wire bonding application

Ultrasonic wire bonding (Fig. 1.3) classified as the first level packaging has been using in microelectronic industries for several decades [Tummala, 1989]. It is a technique used as a means of interconnecting the chips, substrates, and output pins by bonding fine metal wires.

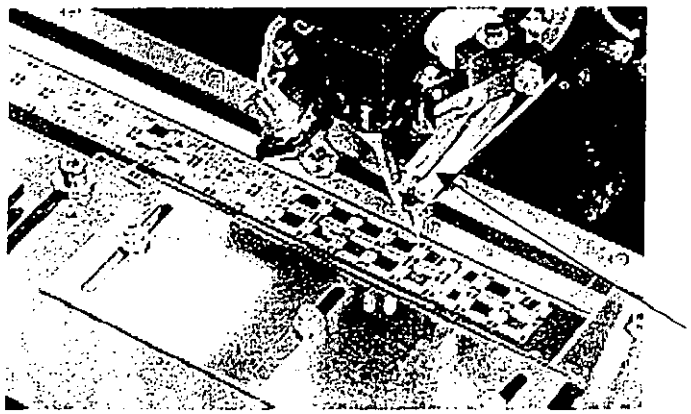

Fig. 1.3 Photograph of a wire bonding technique in microelectronic packaging.

As the size of the IC chips becomes smaller, there is a need to increase the frequency of the bonder transducer (Fig. 1.4) in order to obtain higher yield. As the frequency increases, the bonder transducer design becomes problematic due to the coupling between the thickness and radial vibration modes. As piezoelectric ceramics (e.g. PZT) has high mechanical quality factor Q_M, locking the operating frequency in a designated range becomes increasingly difficult as the frequency goes up. These problems will be alleviated by using composites instead of ceramics since composites have lower Q_M values and wider bandwidth. The mode-coupling problem will also be solved because of the lower planar mode-coupling coefficient. In this work, composites with innovative new designs and different cutting patterns have been developed in order to improve the performance of the ultrasonic transducer. In Fig. 1.4, composites ring fabricated are stacked up to form the sandwich transducer with a bolt.

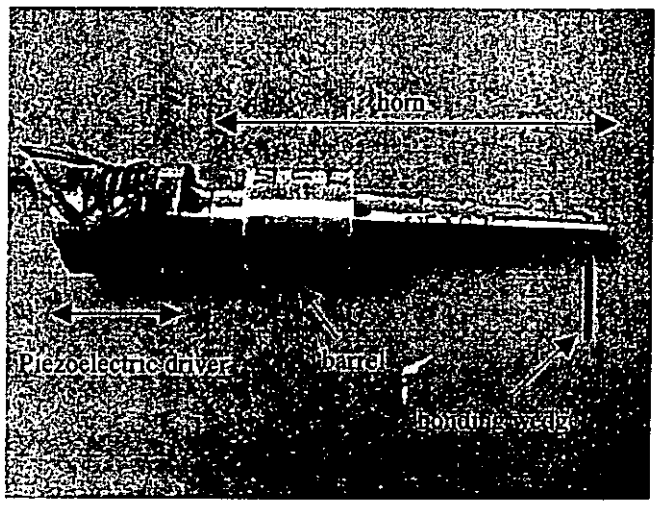

Fig. 1.4 A sandwich type ultrasonic bonding transducer.

1.2 Scope of the work

The main objectives of this work are to fabricate a 1-3 PMN-PT/epoxy composite and PZT/epoxy composite sandwich transducers for ultrasonic transducer applications, and to evaluate their electrical performance.

This thesis describes the fabrication of 1-3 PMN-PT/epoxy and PZT/epoxy composite samples. Thermal, electrical and mechanical properties of PMN-PT single crystal and PZT ceramic will be measured. Characterization of composite samples will also described. The thesis is divided into seven chapters.

The fabrication of PMN-PT single crystals and PZT ceramics is described in Chapter 2. The procedure in sample preparations such as poling and fabrication of composites are also given in Chapter 2.

By the resonance technique described by the IEEE and IRE standards [ANSI/IEEE Std. 176-1987; IRE 46, 1958], thermal stability and material parameters in terms of piezoelectric, elastic and dielectric constants of PMN-PT single crystals and PZT ceramics are characterized in Chapter 3. Various modes of vibrations in the test samples are also described.

In Chapter 4, mechanical properties of epoxy are determined with the ultrasonic immersion method [Read, 1978]. Thermal stability of material parameters are also characterized.

In Chapter 5, piezoelectric coefficients and hydrostatic charge coefficients of PMN-PT single crystals and PZT ceramics are determined by using laser interferometry and by subjecting the samples to hydrostatic pressure, respectively.

In Chapter 6, mode coupling behavior and electrical impedance as a function of frequency for the 1-3 PMN-PT/epoxy composite disc with different thickness are discussed.

Chapter 7 describes the fabrication of the composite transducers for the wire bonding application. Their electrical characterizations are also discussed. Mode of vibrations and material parameters in the PZT ring with different thickness are described.

In Chapter 8, conclusions and suggestions for future work are given.

1.3 Original contributions

The present work has made the following original contributions:

1. The advantage of using piezoelectric ceramic/polymer composites in making sandwich-type drivers to be used in ultrasonic wire bonding application has been established, a US patent application has been filed based on this work.

2. A complete set of electromechanical parameters of PMN-PT single crystals have been measured and reported.

3. The 1-3 PMN-PT/epoxy composite has been fabricated and characterized.

CHAPTER 2

SAMPLE PREPARATION

2.1 Materials used

2.1.1 Lead zirconate titanate (PZT-802) ceramic

Modified lead zirconate titanate (PZT)-802 powder supplied by Piezo Kinetics Inc. in the United States was used in the present study for fabricating the ultrasonic transducers. This material is also called the US Navy Type III material which is a hard PZT material that can withstand high levels of electrical excitation and mechanical stress [PKI data sheet]. It is commonly used in making high voltage or high power generators and transducers. It has a high longitudinal electromechanical coupling constant (k_{33}~0.6), high mechanical quality factor (Q_M ~1000) and low dielectric loss factor (tan δ<0.004).

PZT ceramic has a polycrystalline structure and has a high coupling coefficient near the morphotropic phase boundary (MPB, at 52-53%$PbZrO_3$) between the rhombohedral and tetragonal phases [Tetsuro, 1982]. Ceramic material is made by fusing together a large number of small crystallites [Mason, 1954]. From Fig. 2.1, above the Curie temperature, PZT crystallites are centro-symmetric cubic (isotropic).

Below the Curie temperature, PZT exhibits tetragonal symmetry (anisotropic structure) [Jaffe, 1954]. The tensor property of PZT follows the tensor form of the 6mm point group that have a hexagonal phase structure. It is a solid solution of lead titanate $PbTiO_3$ and lead zirconate $PbZrO_3$ which is modified by adding dopants of other elements in order to meet specific property requirements [Xu, 1991]. PZT 802 ceramic is acceptor (Fe) doped [Zhao, 1996]. PZT has a high Curie temperature T_c up to 300°C which is higher than the normal operating temperature, resulting in a stable operation performance. To elicit the piezoelectric properties, it is necessary to apply a high electric field (typically several kV/mm) to align the dipoles inside the PZT in a process called poling. If the operating temperature is close to the Curie temperature, the material will become partially or completely depoled, thus losing its piezoelectric properties.

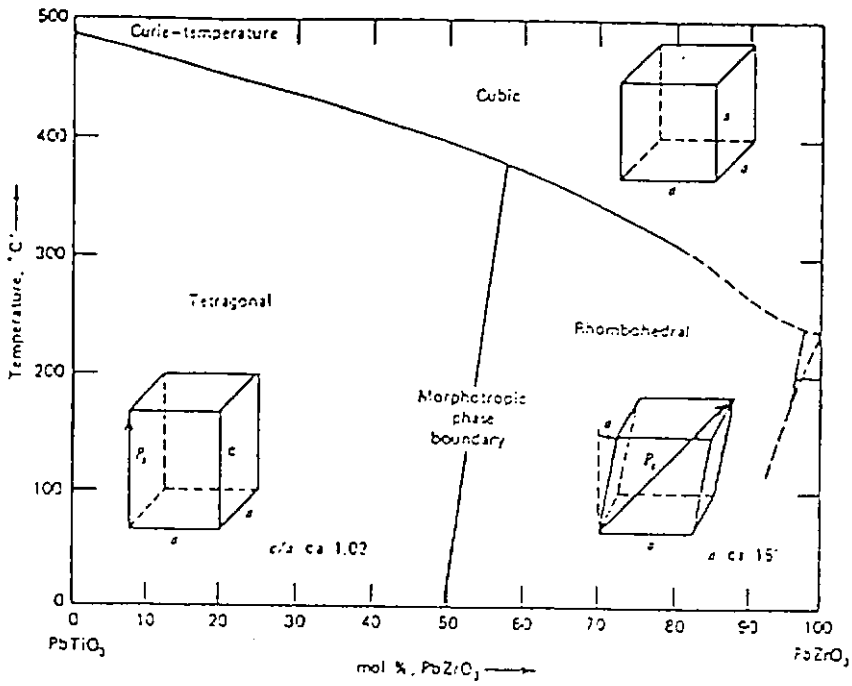

Fig. 2.1 Phase diagram of a PZT system [Rosen, 1992].

2.1.2 Lead magnesium niobate - lead titanate (PMN-33mol%PT) single crystal

Lead magnesium niobate doped with 33 mol% lead titanate (PMN-0.33PT) ferroelectric single crystals grown by Shanghai Institute of Ceramics were also studied. With the composition of 33 mol% PT which is close to the morphotropic phase boundary (MPB) shown in Fig. 2.2, it has extremely high piezoelectric coefficient (d_{33} > 2000 pC/N) and electromechanical coupling coefficient (k_{33}~0.93) at room temperature after being poled in the [001] direction [Gupta, 1998; Park, 1997]. It is a promising material to be used in applications such as ultrasonic imaging transducers and actuators. [Yin , 1999].

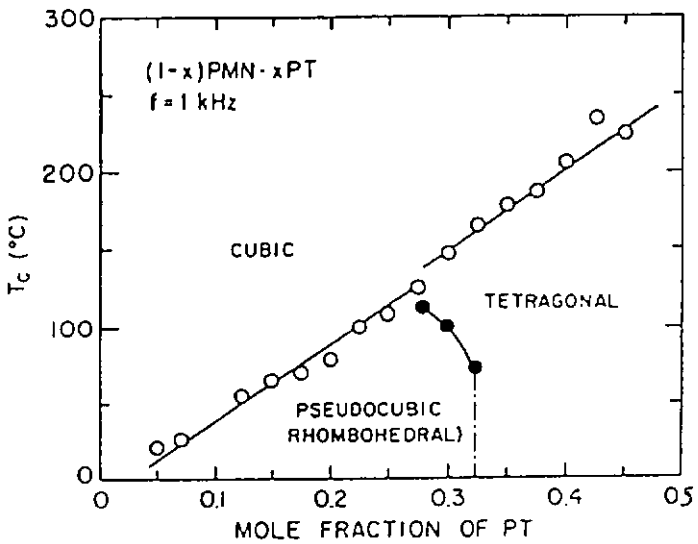

Fig. 2.2 The PMN-PT phase system showing the MPB [Choi, 1989].

With similar crystal structure as another important single crystal PZN-4.5%PT [Liu, 1999], the crystal PMN-0.33PT physically has a cubic perovskite structure with symmetry $m\bar{3}m$ above 150°C but becomes a rhombohedral ferroelectric phase with 3m symmetry below the phase transition temperature. After poling the crystal along the [001] direction, it has a pseudo-tetragonal 4mm macroscopic symmetry [Liu, 1999]. Its material parameters presented in the project are based on this 4 mm symmetry.

2.1.3 Epoxy LW5157 with hardner HY5159

Epoxy LW5157 with hardener HY5159 supplied by Ciba-Giegy was used in the composite fabrication. It can withstand relatively high temperature (up to 120°C – 130°C) and has good wear resistance [Ciba Specialty Chemicals specifications]. The epoxy has a good adhesion to the materials and is quite hard so that it can mechanically support the piezoelectric material elements in the composite structure.

2.2 Fabrication of PZT samples

There are three steps in the fabrication of the PZT samples using the ceramic powder [Xu, 1991]: dry pressing, calcination and binder burnout, and sintering. Before the fabrication, it is essential to make sure that all equipments are clean enough to avoid any contamination by impurities. It is better to wear a plastic glove during the fabrication procedure. Acetone is commonly used to clean the mold before pressing.

2.2.1 Dry pressing

Dry pressing can be used without the need for additional binder because the as-supplied powder has been mixed with PVA (polyvinyl alcohol) which is a common binding agent for easier shaping. A required amount of ceramic powder, with the same weight at each time, was poured into a steel mold shown in Fig. 2.3. Before pressing, make sure that the powder is distributed evenly. The piston was then pressed slowly so that the air trapped inside the mold has enough time to escape. The ring-shaped sample was pressed for 10 minutes in a 15 mm diameter mold under an applied pressure of 8 MPa. In order to prepare different shapes of PZT samples used in subsequent measurements (Fig. 2.4), PZT plates and discs were made. After sintering, samples were cut into required shapes and dimensions with a precision saw.

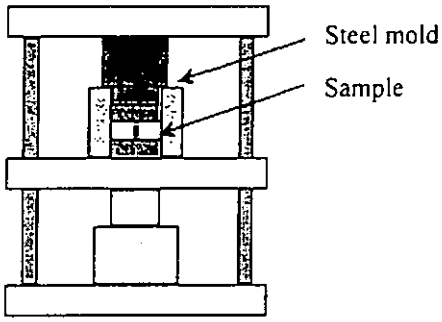

Fig. 2.3 Schematic diagram of the setup for pressing the sample.

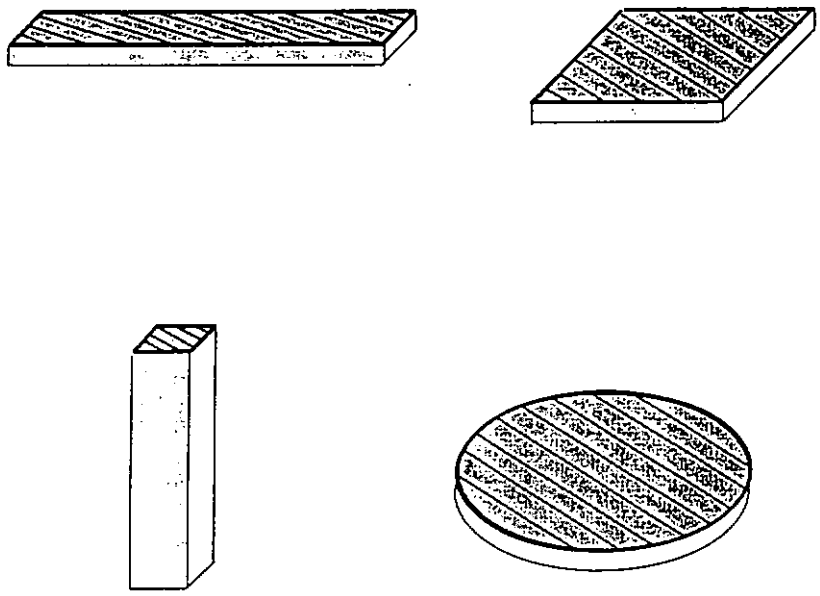

Fig. 2.4 Various PZT samples for the measurements.

2.2.2 Calcination and binder burnout

The pressed samples were put into a recrystallized alumina crucible without being covered and heated in a Lindberg/blue furnace following heating steps as shown in Fig. 2.5. The samples were heated for a long time under the temperature of 300°C so as to remove the PVA. Further heating the samples to about 790°C without the loss of lead can produce the desired compound, $Pb(ZrTi)O_3$ by combination reaction of PZT. After maintaining the samples at the calcinating temperature for one hour, the samples were then cooled down naturally to room temperature after switching off the oven. The samples must be calcinated in an oxidizing atmosphere by allowing air access to the samples through the opening of gas release in the furnace. Otherwise, carbon monoxide (CO) was produced from organic substances such as PVA so that the gas reacted with lead oxide (PbO) to form carbon dioxide and lead, resulting in a decrease in the piezoelectric activities of the samples due to lack of PbO.

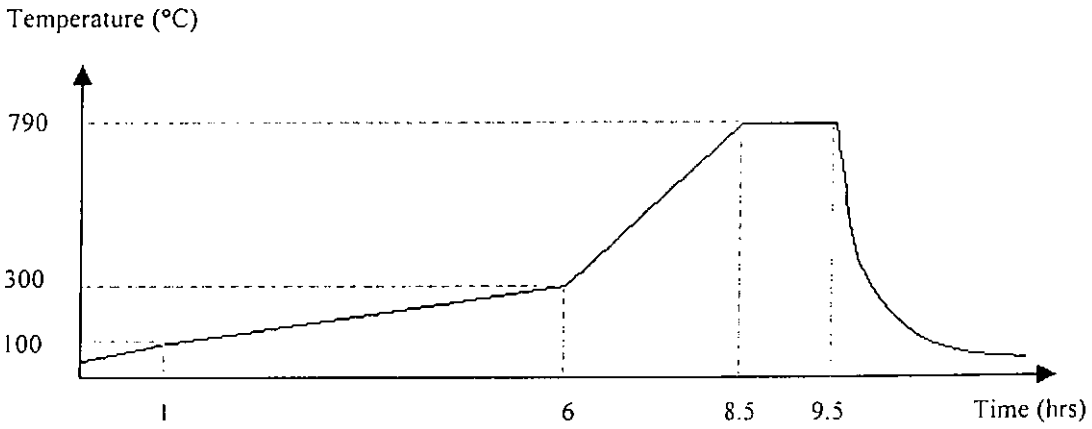

Fig. 2.5 Temperature rise vs time schedule for calcination.

2.2.3 Sintering

The calcined samples, placed in a closed alumina crucible and surrounded with the sintered PZT powder, were then sintered at a temperature of 1285°C in a high temperature furnace Carbolite RHF 16/8 for a period of time shown in Fig. 2.6. Due to the evaporation of PbO above 800°C, the sintered PZT powder covering the samples can maintain a saturated PbO vapor in the crucible so as to prevent the excessive loss of lead content in the samples. After maintaining the samples at the sintering temperature for one hour, the samples were then cooled down naturally to room temperature after switching off the oven. Sintered samples are smaller than the "green" PZT samples. Shrinkage is as follows: outer diameter ~ -13.3%, inner diameter ~ -20.0%, thickness ~ -20%.

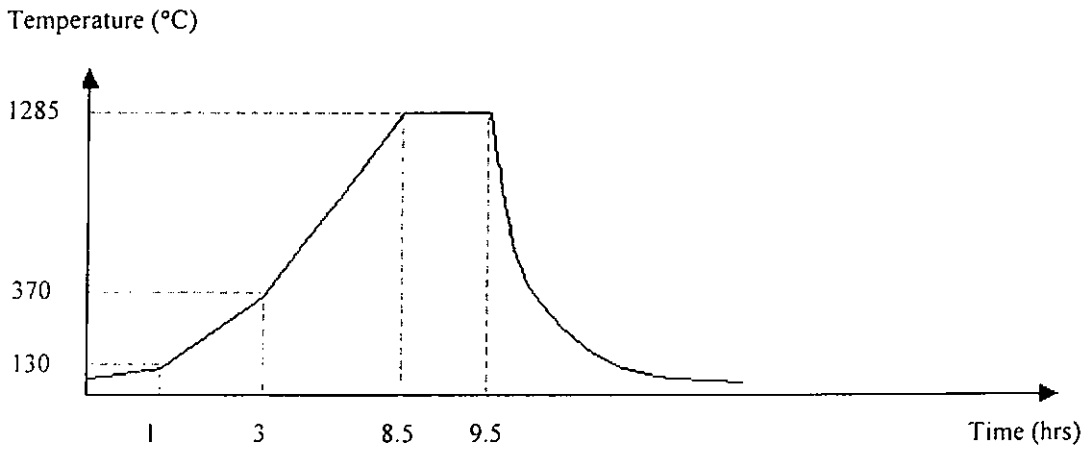

Fig. 2.6 Temperature rise vs time schedule for sintering.

2.3 Poling of PZT samples

In order to pole the sintered samples under a uniform field along the thickness axis, they should be polished by using a Buehler ECOMET 3 variable speed grinder/polisher with different grades of abrasive papers until uniform thickness and smooth flat surfaces were obtained. Silver electrodes were applied on the two flat surfaces with an air-dried silver paint (G3691 Agar Scientific Ltd.). Every sample mounted in a holder was put in a silicon oil bath which has been preheated to a temperature of 120°C (Fig. 2.7). After temperature equilibrium was reached, the sample was poled for 30 minutes by applying a DC poling field of 6.5 kV/mm. Dipoles inside the PZT sample were aligned parallel to the direction of the field and the sample exhibited piezoelectric phenomenon. The sample was then cooled down to room temperature with the heater switched off while the poling field was kept on. It was short-circuited and annealed in an oven at a temperature of 50°C for 24 hours before measurements in order to relieve the stress and charges trapped in the sample during poling.

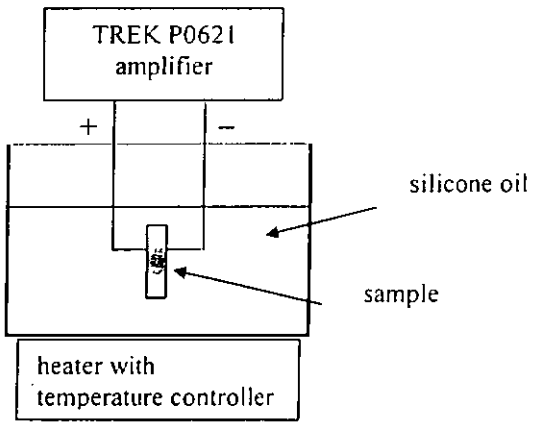

Fig. 2.7 Experimental setup for poling the PZT sample.

2.4 Fabrication of PMN-PT samples

The relaxor ferroelectric PMN-PT single crystals were grown in the Shanghai Institute of Ceramics (SICCAS) by a modified Bridgman method [Yin , 1999] shown in Fig. 2.8. The raw powders of PbO, MgO, Nb_2O_5 and TiO_2 with the purity more than 99.99% were used as the starting materials. The powders were mixed in which the PMN-PT binary system forms a complete solid solution, resulting in a composition of 67%PMN and 33%PT. The PMN-PT single crystals were grown in a platinum crucible with seed crystals along the <100> or <111> direction. During the crystal growth, the highest temperature is usually more than 100°C above the melting point of the crystal (about 1288°C). The temperature in the Bridgman furnace was regulated by a proportional integral differential (PID) controller. The precision of the furnace temperature was controlled within ± 0.5°C. After soaking for about 10 hours, the crucible was pulled down at a rate of 0.1-1.0 mm/hr. Near the end of the crystal growth process, the furnace temperature was decreased at a rate of 25°C/hr to room temperature. Usually PMN-PT single crystals with the size of about ϕ25 x 40 mm could be obtained. The orientations of PMN-PT single crystals were determined by an X-ray diffractometer. 5 Z-cut samples with specific dimensions and orientations as shown in Fig. 2.9 supplied by SICCAS have been used in subsequent characterization.

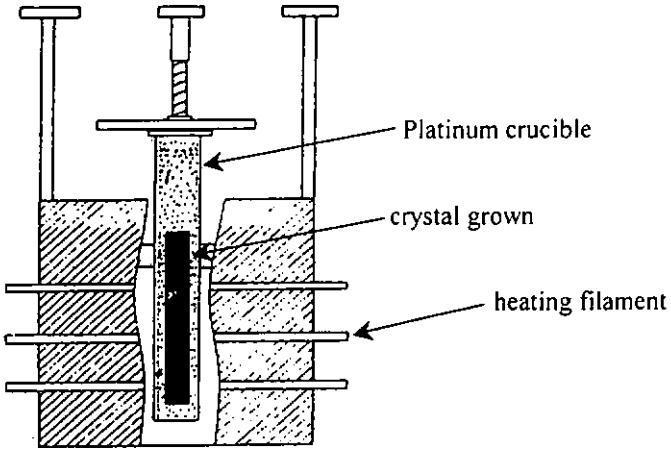

Fig. 2.8 Schematic diagram of the structure of the Bridgman furnace [Yin , 1999].

(ZX cut) long bar

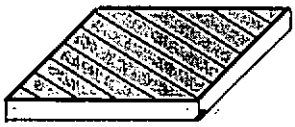

(ZX cut) thin square plate

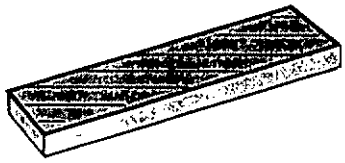

(ZXt cut 45°) long bar

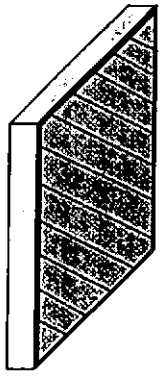

(YZ cut) thin shear plate

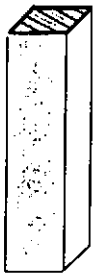

(XZ cut) thin rod

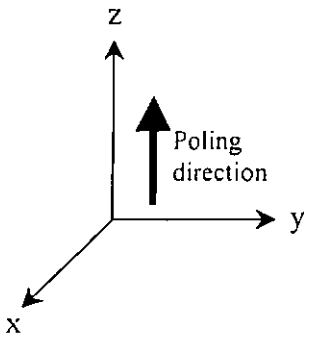

Fig. 2.9 The orientations of PMN-PT single crystals used in the characterization [Geng, 1998]. Refer to Table 3.2b for the dimensions of the crystals.

2.5 Poling of PMN-PT samples

Silver electrodes were applied on the two flat surfaces of the samples with an air-dried silver paint (G3691 Agar Scientific Ltd.) before poling. With an applied frequency of 10 Hz, each sample was put in a silicone oil bath and poled by an AC electric field of 1 kV/mm at room temperature. The poling step was repeated several times to ensure the sample had been completely poled. The sample was then short-circuited and annealed at room temperature for 24 hours before measurements.

2.6 Fabrication of composite samples

2.6.1 Fabrication of PZT/epoxy composite rings

The composite ring consisting of piezoelectric PZT elements embedded in a passive polymer matrix was made using a dice-and-fill technique. Each PZT ring was cut into a "cake" or a "1-3" pattern as shown in Fig. 7.5, respectively using a Buehler ISOMET 2000 precision saw with a blade of 0.1 mm thickness. The sample was cleaned in an ultrasonic bath and dried. The sample was then surrounded by a Teflon collar and epoxy was filled into the grooves. To prepare the epoxy, 100 parts by weight of LW5157 resin with 11 parts by weight of HY5159 hardener was thoroughly mixed and then degassed in vacuum for 15 minutes. It was noticed that the epoxy used has a high viscosity of 3500 CPS. The diced sample attached with

the Teflon collar had to be immersed into the epoxy bath and degassed in vacuum for 30 minutes. The epoxy was then allowed to cure at 40°C in the oven for 12 hours in order to develop optimum properties. Excess epoxy was ground away with wet-and-dry abrasive papers (grade 400, 800 1200).

2.6.2 Fabrication of the 1-3 PMN-PT/epoxy composite

The 1-3 PMN-PT/epoxy composite (Fig. 6.1) was also made with the dice-and-fill technique. The PMN-PT single crystal was firstly cut in one direction using a precision saw with a blade of 0.1mm thickness. The sample was then cleaned in an ultrasonic bath and dried. It was surrounded by a Teflon collar and epoxy was filled into the grooves. After the epoxy had cured, a second cut to the sample perpendicular to the first direction can be made. If reticulated cuts were made in both directions in one go, the PMN-PT rods may break because they are very fragile. Having prepared the epoxy, the diced sample attached with the Teflon collar was then immersed into the epoxy bath and degassed in vacuum for 30 minutes. The epoxy was then allowed to cure at 40°C in the oven for 12 hours in order to develop optimum properties. Excess epoxy was ground away with the abrasive papers.

CHAPTER 3

CHARACTERIZATION OF PMN-PT SINGLE CRYSTALS AND PZT CERAMICS BY THE RESONANCE TECHNIQUE

3.1 Introduction

The tetragonal phase single crystal PMN-0.33PT is a promising material to be used for fabricating actuators and ultrasonic transducers because of its extremely high piezoelectric coefficients (d_{33} > 2000 pC/N) and electromechanical coupling factor (k_{33}~0.93) [Yin, 1999]. Characterization of the material properties (Fig. 3.1) of the PMN-PT single crystal such as the elastic, piezoelectric and dielectric coefficients are very important for applying it in device design but most data are not fully reported yet in the literature.

In this chapter, a resonance technique described in IEEE and IRE standards [ANSI/IEEE Std. 176-1987; IRE 46, 1958] was used to determine the materials properties of PMN-PT single crystals and PZT ceramics. 5 Z-cut PMN-PT samples with specific orientations shown in Fig. 2.9 were used in the measurements [Geng, 1998]. The PZT ceramic samples did not need to be cut in specific orientations because of its ∞ mm symmetry in a plane normal to the poling direction. In the

resonance method, some specific resonance modes are excited by applying an ac field to a piezoelectric material of a specific shape, aspect ratio and specific polarization direction. Resonant and anti-resonant frequencies corresponding to each sample were recorded by the impedance vs frequency spectrum (Fig. 3.2) measured by an HP4194A impedance/gain phase analyzer. Different resonant modes excited in various samples are described in the following sections in order to find the electromechanical coefficients.

ELASTIC STIFFNESS MATRIX
$$\begin{pmatrix} c_{11} & c_{12} & c_{13} & 0 & 0 & 0 \\ c_{12} & c_{11} & c_{13} & 0 & 0 & 0 \\ c_{13} & c_{13} & c_{33} & 0 & 0 & 0 \\ 0 & 0 & 0 & c_{44} & 0 & 0 \\ 0 & 0 & 0 & 0 & c_{44} & 0 \\ 0 & 0 & 0 & 0 & 0 & c_{66} \end{pmatrix}$$

PIEZOELECTRIC MATRIX
$$\begin{pmatrix} 0 & 0 & 0 & 0 & d_{15} & 0 \\ 0 & 0 & 0 & d_{15} & 0 & 0 \\ d_{31} & d_{31} & d_{33} & 0 & 0 & 0 \end{pmatrix}$$

DIELECTRIC MATRIX
$$\begin{pmatrix} \varepsilon_{11} & 0 & 0 \\ 0 & \varepsilon_{11} & 0 \\ 0 & 0 & \varepsilon_{33} \end{pmatrix}$$

For 6 mm, $c_{66} = \frac{c_{11} - c_{12}}{2}$

Fig. 3.1 Elastic, piezoelectric, and dielectric matrices of a tetragonal crystal with 4 mm and for a hexagonal structure of 6 mm point group symmetries [Nye, 1967].

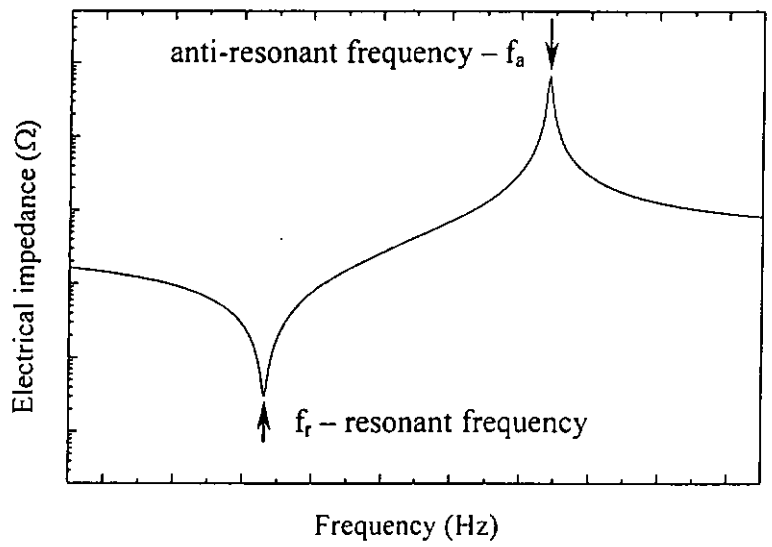

Fig. 3.2 Electrical impedance against frequency spectrum.

3.2 Constitutive equations and matrix notation

Piezoelectric vibrations of test samples with different geometry can be described by a set of constitutive equations in Cartesian tensor notation [ANSI/IEEE Std. 176-1987] which involves mechanical and electrical boundary conditions, given by

$$T_{ij} = c^{E}_{ijkl} S_{kl} - e_{kij} E_k \tag{3.1}$$

$$D_i = e_{ikl} S_{kl} + \varepsilon^{S}_{ik} E_k \tag{3.2}$$

where the components of stress (T) and electric displacement (D) are taken as dependent variables

E_k = electric field tensor
c_{ijkl}^{E} = stiffness tensor at constant electric field
ε_{ik}^{S} = dielectric permittivity, clamped condition
e_{kij} = piezoelectric tensor
S_{ij} = strain tensor

The compressed matrix notation introduced for stress and strain in the IEEE standard employs this symmetry of S_{ij} and T_{ij} with respect to exchange subscripts, i.e. $S_{ij}=S_{ji}$. This matrix notation consists of replacing ij or kl by p or q, where i,j,k,l take the values 1,2,3 and p,q take the values 1,2,3,4,5,6. This allows a new subscript according to the following scheme:

Tensor notation:	11	22	33	23,32	31,13	12,21
Matrix notation:	1	2	3	4	5	6

Then, the piezoelectric constitutive equations become

$$T_p = c^{E}_{pq} S_q - e_{kp} E_k \tag{3.3}$$

$$D_i = e_{iq} S_q + \varepsilon^{S}_{ik} E_k \tag{3.4}$$

The shear strain components S_4, S_5 and S_6 are redefined as

$$S_4 = (S_{23} + S_{32}) = 2S_{23} \tag{3.5}$$

$$S_5 = (S_{31} + S_{13}) = 2S_{13} \tag{3.6}$$

$$S_6 = (S_{12} + S_{21}) = 2S_{12} \tag{3.7}$$

Any mechanical and electrical variables can be chosen as independent variables, the piezoelectric constitutive equations can thus be expressed in other forms:

$$T_p = c_{pq}^D S_q - h_{kp} D_k \tag{3.8}$$

$$E_i = -h_{iq} S_q + \beta_{ik}^S D_k \tag{3.9}$$

Or

$$S_p = s_{pq}^D T_q + g_{kp} D_k \tag{3.10}$$

$$E_i = -g_{iq} T_q + \beta_{ik}^T D_k \tag{3.11}$$

Or

$$S_p = s_{pq}^E T_q + d_{kp} E_k \tag{3.12}$$

$$D_i = d_{iq} T_q + \varepsilon_{ik}^T E_k \tag{3.13}$$

where

c_{pq}^D = elastic stiffness coefficient at constant electric displacement
s_{pq}^E = elastic compliance coefficient at constant electric field
s_{pq}^D = elastic compliance coefficient at constant electric displacement
β_{ik}^T = impermittivity at constant stress, free condition
β_{ik}^S = impermittivity at constant strain, clamped condition
ε_{33}^T = dielectric permittivity at constant stress , free condition
d_{ip} = piezoelectric (charge) coefficient
g_{ip} = piezoelectric (voltage) coefficient
h_{iq} = piezoelectric coefficient

3.3 Vibration modes in piezoelectric materials

3.3.1 Lateral extensional mode of a bar

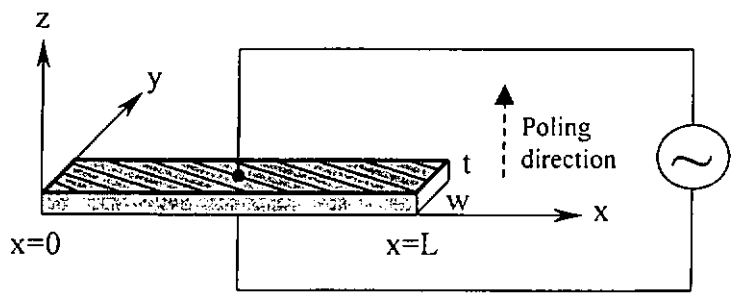

Fig. 3.3a A length-expander bar with the electric field perpendicular to its length.

A long piezoelectric bar with electroded surfaces normal to the z direction which is parallel to the poling direction as shown in Fig. 3.3a is used in determining s_{11}^E and k_{31}.

Assume the cross-sectional dimensions are very small compared with its length,

$$L >> w,t$$

Since the bar is free to vibrate in the x and y directions and its electroded surfaces form equipotential surfaces in the z direction, constant-T & constant-E are thus chosen as independent variables respectively. The following piezoelectric equations are given [Berlincourt,1964]:

$$S = s^E T + dE \tag{3.14}$$

$$D = dT + \varepsilon^T E \tag{3.15}$$

Since the thickness t is negligibly small, $E_1 = E_2 = 0$ throughout the bar. Similarly, stresses $T_2 = T_3 = T_4 = T_5 = T_6 = 0$ on the free surfaces and hence also throughout the bar leaving

$$S_1 = s_{11}^E T_1 + d_{31} E_3 \tag{3.16}$$

$$D_3 = d_{31} T_1 + \varepsilon_{33}^T E_3 \tag{3.17}$$

The admittance of the vibrating bar can then be obtained by (Appendix A.1)

$$\frac{1}{Z} = j\omega \frac{L\omega}{t} \varepsilon_{33}^T \left\{ (1 - k_{31}^2) + k_{31}^2 \frac{\tan(\omega L / 2\upsilon_b^E)}{\omega L / 2\upsilon_b^E} \right\} \tag{3.18}$$

where the free permittivity ε_{33}^T can be obtained directly from an impedance measurement at low frequency (e.g. 1 kHz). υ_b^E is acoustic velocity of the sample.

At resonance for an unloaded bar with no loss, the admittance becomes infinite, giving

$$\tan \frac{\omega L}{2\upsilon_b^E} = \infty \quad \text{and} \quad f_r = \frac{\upsilon_b^E}{2L} \tag{3.19}$$

This is followed by a zero of admittance at anti-resonance f_a given by

$$\frac{\tan[(\pi/2)(f_a/f_r)]}{(\pi/2)(f_a/f_r)} = \frac{k_{31}^2 - 1}{k_{31}^2} \tag{3.20}$$

Conversely, electromechanical coupling factor k_{31} can be calculated from measured values of f_r and f_a. Elastic compliance s_{11}^E can be determined by

$$s_{11}^E = \frac{1}{\rho (2Lf_r)^2} \tag{3.21}$$

3.3.2 Thickness mode of a thin square plate

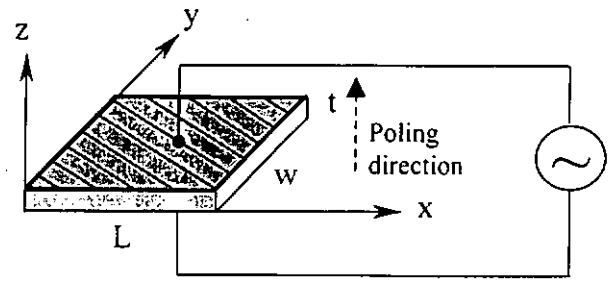

Fig. 3.3b A thin plate with the electric field parallel to its thickness.

A thin piezoelectric plate with electroded surfaces normal to the z direction which is parallel to the poling direction as shown in Fig. 3.3b is used in determining c_{33}^E, c_{33}^D, k_t, $\varepsilon_{33}^T$and ε_{33}^S.

Assume the thickness is small compared with its length and width,

$$L, w >> t$$

The plate can be considered to be laterally clamped (S_1= S_2= S_4= S_5= S_6=0) for plane wave propagation in the thickness direction. Similarly for an insulating dielectric medium with no electric flux leakage D_1=D_2=0 and $\partial D_3/\partial z$=0. These suggest that D and S can be chosen as independent variables giving [Berlincourt,1964]

$$T_3 = c_{33}^D S_3 + h_{33} D_3 \tag{3.22}$$

$$E_3 = -h_{33} S_3 + \beta_{33}^S D_3 \tag{3.23}$$

The electrical impedance which has been evaluated in Appendix A.1 can be obtained as

$$Z = \frac{\int_0^t E_3 dz}{j\omega w D_3} = \frac{1}{j\omega C_c}[1 - k_t^2 \frac{\tan(\omega \cdot t / 2\upsilon_b^D)}{\omega \cdot t / 2\upsilon_b^D}] \tag{3.24}$$

where $C_c = w/(t\beta_{33}^S)$ is the clamped capacitance of the plate. Resonance f_r and anti-resonance f_a are obtainable from the minimum f_r and maximum f_a impedance. Assume the losses are negligible, i.e., $f_r = f_s$, $f_a = f_p$,

Electromechanical coupling factor k_t can be calculated by Eq. (3.26).

$$f_a = \frac{\upsilon_b^D}{2t} \tag{3.25}$$

$$k_t^2 = \frac{\pi}{2}\frac{f_r}{f_a}\tan(\frac{\pi}{2}\frac{f_a - f_r}{f_a}) \tag{3.26}$$

Elastic stiffness c_{33}^D, c_{33}^E can be determined by

$$c_{33}^E = c_{33}^D(1 - k_t^2) \tag{3.27}$$

$$c_{33}^D = \rho(2tf_a)^2 \tag{3.28}$$

The free dielectric constant ε_{33}^T can be calculated from the measured capacitance C_0 at 1kHz with the equation given by

$$C_0 = \frac{\varepsilon_0 \varepsilon_{33}^T A}{t} \tag{3.29}$$

where A is the area of electrode. The clamped dielectric constant ε_{33}^S can be measured at twice the parallel resonant frequency f_p.

3.3.3 Thickness shear mode of a thin plate

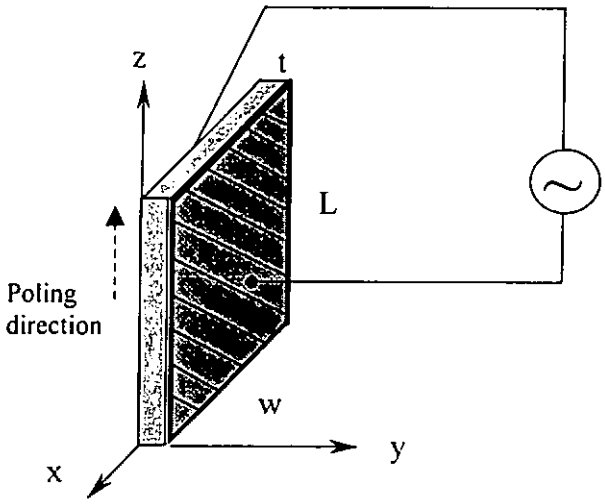

Fig. 3.3c A shear plate with the electric field parallel to its thickness.

A thin shear piezoelectric plate with electroded surfaces normal to the y direction which is perpendicular to the poling direction as shown in Fig. 3.3c is used for determining c_{44}^E, c_{44}^D, s_{44}^E, k_{15}, ε_{11}^T and ε_{11}^S.

When thickness of the plate is small compared with its length and width, $L, w >> t$, the plate can be considered to be laterally clamped ($S_1 = S_2 = S_3 = S_4 = S_6 = 0$) for shear wave propagation in the thickness direction. D and S can be chosen as independent variables giving

$$T_5 = c_{55}^D S_5 + h_{15} D_1 \tag{3.30}$$

$$E_1 = -h_{15} S_5 + \beta_{11}^S D_1 \tag{3.31}$$

The behavior of the thickness shear mode with electric field parallel to the direction of propagation can be described by equations similar to that derived in section 3.3.2.

Therefore,

$$k_{15}^2 = \frac{\pi}{2}\frac{f_r}{f_a}\tan(\frac{\pi}{2}\frac{f_a - f_r}{f_a}) \tag{3.32}$$

$$c_{44}^E = c_{44}^D(1 - k_{15}^2) \tag{3.33}$$

$$c_{44}^D = \rho(2tf_a)^2 \tag{3.34}$$

$$s_{44}^E = \frac{1}{c_{44}^E} \tag{3.35}$$

ε_{11}^T and ε_{11}^S can be determined in the same way as in the thickness mode.

3.3.4 Length extensional mode of a rod

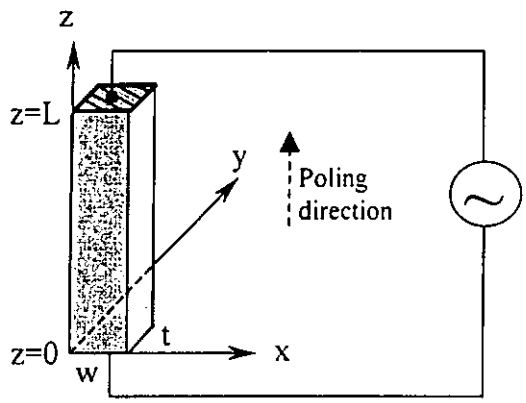

Fig. 3.3d A long rod with the electric field parallel to its length.

A long piezoelectric rod with electroded surfaces normal to the z (poling) direction as shown in Fig. 3.3d is used in determining s_{33}^E, $s_{33}^D$and k_{33}.

Consider the rod is so long that the permittivity of the bar is sufficiently greater than that of its surroundings to prevent fringing electric fields, electric flux lines will also be parallel to its length, such that $D_1 = D_2 = 0$, $\partial D_3/\partial z=0$. With negligible cross-sectional dimensions, all stresses will be zero except T_3. Hence, D and T are chosen as independent variables, giving piezoelectric equations as: [Berlincourt,1964]

$$S_3 = s_{33}^D T_3 + g_{33} D_3 \tag{3.36}$$

$$E_3 = -g_{33} T_3 + \varepsilon_{33}^T D_3 \tag{3.37}$$

The equation of the impedance of the rod vibrating along the z direction is given by (Appendix A.2)

$$Z = \frac{1}{j\omega C_s}\{1 - k_{33}^2 \frac{\tan(\omega L / 2\upsilon_b^D)}{\omega L / 2\upsilon_b^D}\} \tag{3.38}$$

where

$$C_s = \frac{A}{L\beta_{33}^S} = \frac{A\varepsilon_{33}^S}{L} \tag{3.39}$$

$$\beta_{33}^S = \beta_{33}^T(1 + \frac{g_{33}^2}{\beta_{33}^T s_{33}^D}) \tag{3.40}$$

$$k_{33}^2 = \frac{g_{33}^2}{\beta_{33}^T s_{33}^D + g_{33}^2} \tag{3.41}$$

$$\upsilon_b^D = (\frac{1}{\rho s_{33}^D})^{\frac{1}{2}} \tag{3.42}$$

$$k_{33}^2 = \frac{d_{33}^2}{s_{33}^E \varepsilon_{33}^T} = \frac{\varepsilon_{33}^T g_{33}^2}{s_{33}^E} \tag{3.43}$$

A is the cross-sectional area w·t ,C_s is the clamped capacitance, s_{33}^D and k_{33} can be calculated using

$$s_{33}^D = \frac{1}{\rho(2Lf_a)^2} \tag{3.44}$$

$$k_{33}^2 = \frac{\pi}{2}\frac{f_r}{f_a}\tan(\frac{\pi}{2}\frac{f_a - f_s}{f_a}) \tag{3.45}$$

$$s_{33}^E = \frac{s_{33}^D}{(1 - k_{33}^2)} \tag{3.46}$$

3.3.5 Radial mode of a thin disc

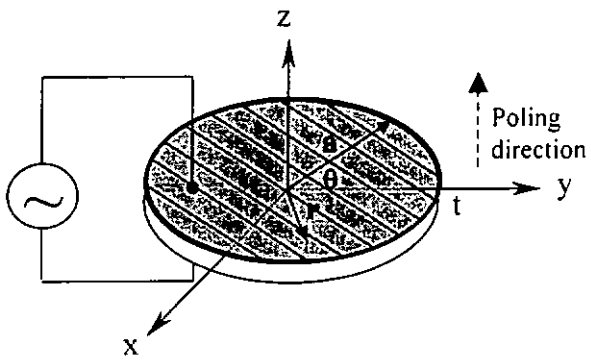

Fig. 3.3e A thin disc with the electric field parallel to its thickness.

A thin piezoelectric disc with electroded surfaces perpendicular to the poling direction as shown in Fig. 3.3e is used for determining k_p, σ^p and s_{12}^E.

It is noted that the radial mode of the disc has been used only for measurements on poled ferroelectric ceramics such as PZT. Whereas the disc for determining k_p, and σ^p are not used in the single crystal. To determine s_{12}^E in the single crystal, a length extensional [110] bar as described in the next section is used.

Assume the disc radius *a* is large compared to its thickness *t*, (a/t > 20). Consider strong mode vibration existing in the plane normal to the poling direction and the thickness t is negligibly small, such that $T_{33}=T_{r3}=T_{\theta 3}=0$ and $\xi_0=\xi_3=0$, $T_{r0}=0$, throughout the disc. Electric field is applied along the z direction such that $D_r=D_\theta=0$. constant-T & constant-E are thus chosen as independent variables respectively.[Ikeda, 1990].

The constitute equations of the system are given by:

$$S_{rr} = s_{11}^{E} T_{rr} + s_{12}^{E} T_{\theta\theta} + d_{31} E_3 \tag{3.47}$$

$$S_{\theta\theta} = s_{12}^{E\,E} T_{rr} + s_{11}^{E} T_{\theta\theta} + d_{31} E_3 \tag{3.48}$$

$$D_3 = d_{31}(T_{rr} + T_{\theta\theta}) + \varepsilon_{33}^{T} E_3 \tag{3.49}$$

The electrical impedance of the disc is described briefly in Appendix A.3 and is given by

$$Z = \frac{V}{I} = \frac{t}{j\omega \cdot \pi \cdot a^2 \cdot \varepsilon_{33}^{T}} \{ \frac{\Im(\frac{\omega \cdot a}{\upsilon^{p}}) + \sigma^{p} - 1}{(1 - k_p^2)\Im(\frac{\omega \cdot a}{\upsilon^{p}}) + \sigma^{p} - 1 + 2k_p^2} \} \tag{3.50}$$

where

$$\sigma^{p} = -\frac{s_{12}^{E}}{s_{11}^{E}} \tag{3.51}$$

$$k_p^2 = \frac{2d_{31}^2}{(s_{11}^{E} + s_{12}^{E})\varepsilon_{33}^{T}} \tag{3.52}$$

σ^p is the planar Poisson's ratio, k_p is the planar coupling coefficient, and $\Im$ is the modified quotient of Bessel functions defined by

$$\Im(y) = \frac{y J_0(y)}{J_1(y)} \tag{3.53}$$

where J_0 and J_1 are the zero and first order of Bessel functions of the first kind respectively, defined by

$$J_0(y) = \sum_{n=0}^{\infty} \frac{(-1)^n}{n!n!} (\frac{y}{2})^{2n} \tag{3.54}$$

$$J_1(y) = \sum_{n=0}^{\infty} \frac{(-1)^n}{n!(n+1)!} (\frac{y}{2})^{2n+1}$$

From Eq. (3.50), the resonant frequencies are given by the roots of the transcendental equation

$$\Im(\omega : a/\upsilon^{p}) = 1 - \sigma^{p} \tag{3.55}$$

Defined η_1 which is the lowest root of the above equation.

$$\eta_1 = 2\pi f_r a/\upsilon^{p} \tag{3.56}$$

where f_r is the fundamental resonant frequency of the radial mode.

The second lowest root of the above equation will give the first overtone resonant frequency, $f_r^{(2)}$ which is shown in Fig. 3.4. With the knowledge of the ratio of $f_r^{(2)}/f_r$, σ^p and η_1 can be calculated from Table 3.1.

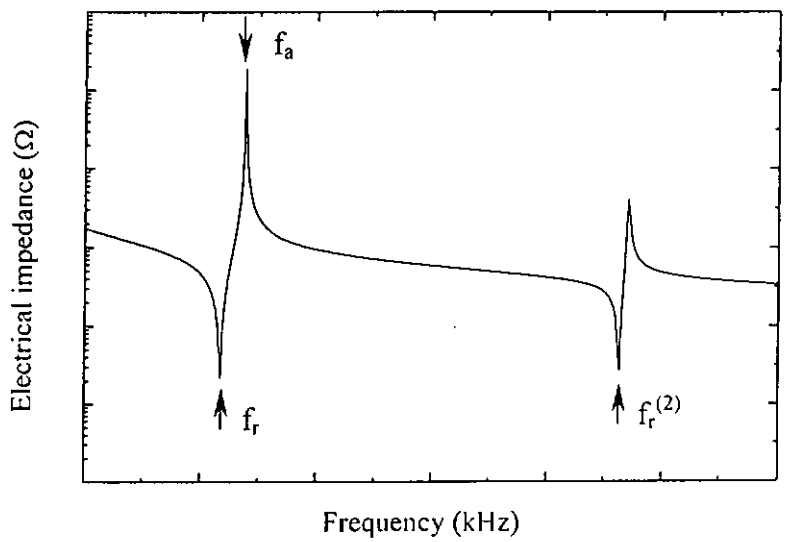

Fig. 3.4 Electrical impedance against frequency spectrum of the radial mode.

At anti-resonant frequency f_a for a disc with no loss, the equation of the impedance Z becomes infinite, giving

$$(1-k_p^2)\Im\{\omega a/(\upsilon^p)^{1/2}\}+\sigma^p-1+2k_p^2=0 \tag{3.57}$$

φ_1 was defined as

$$\varphi_1 = 2\pi f_a a/\upsilon^p = \eta_1(1+\frac{f_a-f_r}{f_r}) \tag{3.58}$$

k_p can be calculated by giving

$$k_p^2 = \frac{\Im(\varphi_1)+\sigma^p-1}{\Im(\varphi_1)-2} \tag{3.59}$$

s_{12}^E was also calculated by

$$\sigma^p = \frac{-s_{12}^E}{s_{11}^E} \tag{3.60}$$

Table 3.1 Frequency constant of a disc resonator $\eta_1=2\pi f_s a/v^p$ and ratio of the first overtone to fundamental resonant frequencies $f_s^{(2)}/f_s$ as a function of the planar Poisson's ratio. [ANSI/IEEE Std. 176-1987]

σ	η_1	$f_s^{(2)}/f_s$
0	1.84118	2.89566
0.05	1.87898	2.84258
0.10	1.91539	2.79360
0.15	1.95051	2.74826
0.20	1.98441	2.70617
0.25	2.01717	2.66699
0.30	2.04885	2.63043
0.35	2.07951	2.59625
0.40	2.10920	2.56423
0.45	2.13797	2.53416
0.50	2.16587	2.50589
0.55	2.19294	2.47926
0.60	2.21922	2.45414
0.65	2.24434	2.43040

3.3.6 Length extensional mode of a [110] bar

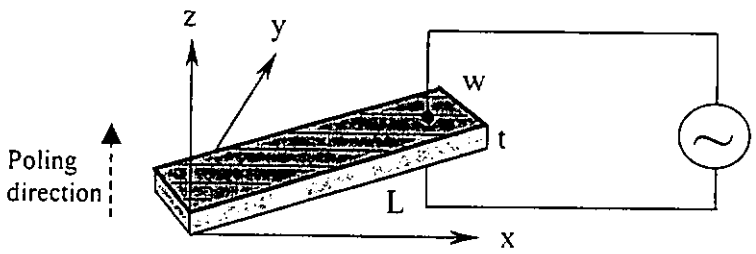

Fig. 3.3f A length extensional [110] bar with the electric field perpendicular to its length.

A long piezoelectric bar with electroded faces normal to the z direction which is parallel to the poling direction as shown in Fig. 3.3f is used for determining $s_{11}^E(45°)$, $k_{31}(45°)$, s_{12}^E and s_{66}^E. The excitation of resonance mode vibration and requirement of dimensions are the same as that of the bar mentioned in section 3.3.1.

The formulae used for calculating $s_{11}^E(45°)$, $k_{31}(45°)$ are:

$$\frac{k_{31}^2(45°)}{1-k_{31}^2(45°)} = \frac{\pi}{2}\frac{f_a}{f_r}\tan\left(\frac{\pi}{2}\frac{f_a-f_r}{f_r}\right) \tag{3.61}$$

$$s_{11}^E(45°) = \frac{1}{\rho(2lf_r)^2} \tag{3.62}$$

With the known values of $s_{11}^E(45°)$, s_{12}^E is calculated by Eq. (3.69). s_{66}^E can be calculated by

$$s_{11}^E(45°) = \frac{1}{2}(s_{11}^E + s_{12}^E) + \frac{1}{4}s_{66}^E \tag{3.63}$$

where $s_{11}^E(45°)$ is the elastic compliance in the diagonal direction of the x-y plane. s_{66}^E is the shear elastic compliance.

3.4 Calculations of other material parameters

The material parameters: s_{11}^E, k_{31}, c_{33}^E, c_{33}^D, k_t, ε_{33}^T, ε_{33}^S, c_{44}^E, c_{44}^D, s_{44}^E, k_{15}, ε_{11}^T, ε_{11}^S, s_{33}^E, s_{33}^D and k_{33} have been determined from the first four test samples (Fig. 3.3a-d) by resonance technique. For PZT ceramic test samples, k_p, σ^P, s_{12}^E have been determined from the thin piezoelectric disc (Fig. 3.3e). s_{66}^E, s_{66}^D can be calculated by

$$s_{66}^E = 2\cdot(s_{11}^E - s_{12}^E) \tag{3.64}$$

$$s_{66}^D = s_{66}^E \tag{3.65}$$

For single crystal of 4 mm point group symmetry, having determined $s_{11}^E(45°)$ from the [110] long bar (Fig. 3.3f), s_{66}^E can be calculated with the known value s_{12}^E determined by Eq. (3.69).

The remaining parameters for both 6 mm and 4 mm point group symmetries can be calculated according to:

$$e_{33} = k_t\sqrt{c_{33}^D\varepsilon_{33}^s} \tag{3.66}$$

$$e_{31} = (\varepsilon_{33}^T - \varepsilon_{33}^s - d_{33}e_{33})/2d_{31} \tag{3.67}$$

$$s_{13}^E = (d_{33} - e_{33}s_{33}^E)/2e_{31} \tag{3.68}$$

$$s_{12}^E = -[s_{11}^E - \frac{2\cdot(s_{13}^E)^2}{s_{33}^E - 1/c_{33}^E}] \tag{3.69}$$

where d_{33}, d_{31} are piezoelectric strain constants. e_{33}, e_{31} are piezoelectric stress constants.

For determining the piezoelectric coefficients d_{33}, d_{31} and hydrostatic charge coefficient d_h,

$$d_{31} = k_{31} \cdot \sqrt{s_{11}^E \cdot \varepsilon_{33}^T} \tag{3.70}$$

$$d_{33} = k_{33} \cdot \sqrt{s_{33}^E \cdot \varepsilon_{33}^T} \tag{3.71}$$

$$d_h = d_{33} + 2 \cdot d_{31} \tag{3.72}$$

Other material parameters shown as follow :

$$s_{11}^D = [1-(k_{31})^2] \cdot s_{11}^E \tag{3.73}$$

$$c_{13}^D = c_{13}^E + \frac{e_{31}e_{33}}{\varepsilon_{33}^S} \quad (3.74) \qquad c_{13}^E = \frac{e_{33} - d_{33}c_{33}^E}{2d_{31}} \tag{3.75}$$

$$c_{12}^D = \frac{-(s_{12}^D \cdot s_{33}^D - s_{13}^{D^2})}{(s_{11}^D - s_{12}^D) \cdot \{s_{33}^D \cdot (s_{11}^D + s_{12}^D) - 2 \cdot s_{13}^{D^2}\}} \tag{3.76}$$

$$c_{12}^E = \frac{-(s_{12}^E \cdot s_{33}^E - s_{13}^{E^2})}{(s_{11}^E - s_{12}^E) \cdot \{s_{33}^E \cdot (s_{11}^E + s_{12}^E) - 2 \cdot s_{13}^{E^2}\}} \tag{3.77}$$

$$c_{11}^E = \frac{s_{11}^E \cdot s_{33}^E - s_{13}^{E^2}}{(s_{11}^E - s_{12}^E) \cdot \{s_{33}^E \cdot (s_{11}^E + s_{12}^E) - 2 \cdot s_{13}^{E^2}\}} \tag{3.78}$$

$$c_{11}^D = \frac{s_{11}^D \cdot s_{33}^D - s_{13}^{D^2}}{(s_{11}^D - s_{12}^D) \cdot \{s_{33}^D \cdot (s_{11}^D + s_{12}^D) - 2 \cdot s_{13}^{D^2}\}} \tag{3.79}$$

$$s_{44}^D = \frac{1}{c_{44}^D} \quad (3.80) \qquad c_{66}^D = \frac{1}{s_{66}^D} \tag{3.81}$$

$$s_{13}^D = s_{13}^E - g_{33} \cdot d_{31} \quad (3.82) \qquad s_{12}^D = s_{12}^E - (k_{31})^2 \cdot s_{11}^E \tag{3.83}$$

$$g_{33} = \frac{d_{33}}{\varepsilon_{33}^T} \quad (3.84) \qquad g_{31} = \frac{d_{31}}{\varepsilon_{33}^T} \tag{3.85}$$

where g_{33}, g_{31} are piezoelectric voltage constants

Density of the samples are determined by applying the Archimedes principle. Mass of the samples in air and water are measured respectively using an electronic balance with the resolution of 0.001mg. Density of the samples can be calculated by

$$V_{air} = \frac{M_{air} - M_{water}}{\rho_{water}} \tag{3.86}$$

$$\rho_{sample} = \frac{M_{air}}{V_{air}} \tag{3.87}$$

Given density of water ρ_{water} at room temperature = 1000 kg/m^3 [standard test method , C373-72]

Frequency constant of N_1, N_{3t}, N_5, N_p in cycle Hz·m can be calculated by

$$N_1 = f_r \cdot L \tag{3.88}$$

$$N_{3t} = f_r \cdot t \tag{3.89}$$

$$N_5 = f_r \cdot t \tag{3.90}$$

$$N_p = f_r \cdot 2a \tag{3.91}$$

where L is the length of the bar, t is the thickness of the plate and a is the radius of the disc.

Young's modulus Y can be calculated by

$$Y = \frac{1}{s_{33}^E} \tag{3.92}$$

The measurement of mechanical quality factor Q_M is given by

$$Q_M = \frac{1}{2\pi f_r Z_m (C_0 + C_1)} \frac{f_a^2}{(f_a^2 - f_r^2)} \tag{3.93}$$

where Z_m is the minimum impedance at resonant frequency f_r.

The electromechanical characteristics of a piezoelectric ceramic element can be represented in the simplest form by the following equivalent circuit. C_0 and C_1 can be calculated from the impedance analyzer measurement with the equivalent circuit simulation.

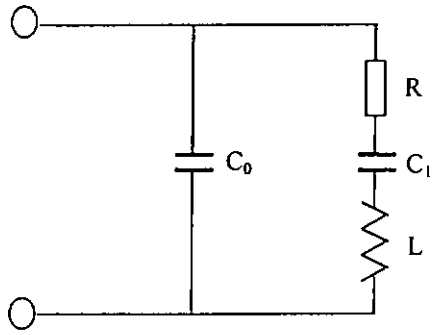

Fig. 3.5 Equivalent circuit for representing the dynamic properties of piezoelectric ceramic element.

where C_0 is the clamped electrical capacitance, L, C_1 and R are inductance, electrical capacitance and resistance respectively, which represent the converted mechanical properties-effective mass, compliance and mechanical loss.

Electrical Q factor Q_E is given by

$$Q_E = \frac{1}{\tan\delta} \tag{3.94}$$

where dissipation factor tan δ can be measured by the impedance analyzer at 1kHz.

3.5 Material parameters of PMN-PT single crystals and PZT ceramics

With the measured resonance data of PMN-PT single crystals and PZT ceramics (Table 3.2a and 3.2b), their elastic, piezoelectric and dielectric constants were determined by the resonance technique. In Table 3.3, the measured material parameters of the PZT samples agree quite well with that of the commercial PZT 8 ceramic given by two companies, Morgan and PKI. This indicates the validity of the measurement technique.

Table 3.2a Data of the PZT test samples.

Test samples	Dimensions in mm			Vibrational Modes	Frequency in kHz	
	length L	width w	thickness t		resonance f_r	anti-resonance f_a
Long bar	9.53	2.07	1.05	Length	181.73	190.30
Square plate	9.80	9.80	1.05	Thickness	1998.10	2165.01
Shear plate	13.10	8.10	0.60	Thickness Shear	1884.99	2174.98
Thin rod	4.68	0.80	0.80	Height	353.27	450.12
Disc	radius=10.95		1.05	Planar	f_r=106.29 $f_r^{(2)}$=278.47	118.87

Table 3.2b Data of the PMN-PT single crystal samples.

Test samples	Dimensions in mm			Vibrational modes	Frequency in kHz	
	length L	width w	thickness t		resonance f_r	anti-resonance f_a
[100] Long bar	15.07	5.64	0.87	Length	74.56	87.06
[100] Square plate	15.45	15.48	0.87	Thickness	2222.84	2672.00
[100] Shear plate	15.09	10.31	0.87	Thickness Shear	1331.25	1798.50
[001] Thin rod	4.15	1.02	0.87	Height	199.88	422.13
[110] Long bar	12.42	3.41	0.87	Length	112.05	132.75

Table 3.3 Elastic, piezoelectric, dielectric constants and electromechanical coupling factors for test samples measured by resonance technique at room temperature.

Material parameters	PMN-0.33PT Single crystal	PKI PZT 802	Commercial PZT 8	
			PKI	Morgan
Electromechanical coupling factor				
k_{33}	0.90	0.66	0.61	0.64
k_{31}	-0.58	-0.33	-0.30	-0.30
k_{15}	0.71	0.54	0.54	0.55
k_t	0.59	0.42	---	0.48
k_p	undetermined	0.49	0.51	0.51
Constant electric field elastic compliance ($10^{-12}m^2/N$)				
s_{11}^E	25.07	10.97	10.40	11.50
s_{12}^E	-5.10	-3.51	---	-3.70
s_{13}^E	-21.27	-4.49	---	-4.80
s_{33}^E	54.27	13.13	13.50	13.50
s_{44}^E	26.04	27.27	---	31.90
s_{66}^E	25.42	28.96	---	30.40
Constant electric displacement elastic compliance ($10^{-12}m^2/N$)				
s_{11}^D	16.64	9.78	---	10.10
s_{12}^D	-13.54	-4.70	---	-4.50
s_{13}^D	-1.38	-1.76	---	-2.50
s_{33}^D	10.31	7.41	---	8.50
s_{44}^D	12.92	19.34	---	22.60
s_{66}^D	25.42	28.96	---	30.4
Constant stress dielectric constant				
$\varepsilon_{33}^T/\varepsilon_0$ at 1kHz	3309	967	1000	1000
$\varepsilon_{11}^T/\varepsilon_0$ at 1kHz	4877	1317	---	1290
Constant strain dielectric constant				
$\varepsilon_{33}^S/\varepsilon_0$ at $2*f_p$	599	571	---	600
$\varepsilon_{11}^S/\varepsilon_0$ at $2*f_p$	2157	895	---	900

Cont.

Table 3.3 Elastic, piezoelectric, dielectric constants and electromechanical coupling factors for test samples measured by resonance technique at room temperature.

Material parameters	PMN-0.33PT	PKI	Commercial PZT 8	
	Single crystal	PZT 802	PKI	Morgan
Constant electric field elastic stiffness (10^{10} N/m^2)				
c_{11}^E	11.82	14.84	---	14.90
c_{12}^E	10.50	7.93	---	8.11
c_{13}^E	10.41	9.44	---	8.11
c_{33}^E	11.13	12.93	---	13.20
c_{44}^E	3.84	3.67	---	3.13
c_{66}^E	3.93	3.45	---	3.40
Constant electric displacement elastic stiffness (10^{10} N/m^2)				
c_{11}^D	12.10	15.23	---	15.20
c_{12}^D	10.78	8.33	---	8.41
c_{13}^D	9.13	8.60	---	7.03
c_{33}^D	17.08	15.71	---	16.90
c_{44}^D	7.74	5.18	---	4.46
c_{66}^D	3.93	3.45	---	---
Piezoelectric strain constant (10^{-12}C/N)				
d_{33}	1158	221	220	225
d_{31}	-497	-96	-100	-97
d_h	164	29	---	31
Piezoelectric voltage constant (10^{-3}m^{2}C^{-1})				
g_{33}	38.48	27.58	24.90	25.40
g_{31}	-17.65	-11.57	-11.30	-10.90
g_{15}	17.45	26.08	36.20	28.90
Mechanical quality factor				
Q_M	85	871	900	1000
Q_E	42	302	250	250

Cont.

Table 3.3 Elastic, piezoelectric, dielectric constants and electromechanical coupling factors for test samples measured by resonance technique at room temperature.

Material parameters	PMN-0.33PT Single crystal	PKI PZT 802	Commercial PZT 8	
			PKI	Morgan
Piezoelectric stress constant (C/m^2)				
e_{33}	17.75	11.83	---	14.0
e_{31}	-3.84	-3.59	---	-4.10
e_{15}	27.29	10.93	---	10.30
Piezoelectric stiffness constant ($10^8 NC^{-1}$)				
h_{33}	33.49	23.43	---	26.40
h_{31}	-5.25	-3.54	---	-7.70
h_{15}	13.5	13.48	---	12.90
Frequency constant (Hz-m)				
N_1	1124	1732	1750	1700
N_{3t}	1934	2098	2100	2070
N_5	1158	1131	1460	---
N_p	undetermined	2328	2360	---
Acoustic velocity (m/s)				
υ_3^D	4649	4547	---	4720
υ_4^E	2204	2198	---	2030
Density ρ (kg/m^3)	7902	7597	7600	7600
Poisson's ratio σ	undetermined	0.32	0.31	0.31
Young modulus Y ($10^{10} N/m^2$)	1.8	7.6	7.2	---

3.6 Thermal stability of the material parameters

3.6.1 Introduction

Detailed material parameters of PMN-0.33PT single crystals and PZT 802 ceramics at room temperature have been characterized. The change of the material parameters with the change of temperature on the piezoelectric properties of the single crystals which are also useful in practical application have not been reported. With the use of the single crystals for ultrasonic applications in the future, the temperature change inside the device is an important factor due to its low Curie temperature of around 120-160°C [Yin, 1999]. Heat generated in the device under long driving operation would deteriorate its performance if the temperature is approaching the Curie temperature. In this section, some important material parameters variation of PMN-0.33PT single crystals and PZT 802 ceramics were studied within the temperature ranging from 20°C to 100°C.

3.6.2 Experimental results of PMN-PT single crystals and PZT ceramics

Samples are placed in a computer controlled oven and connected to a HP4194A impedance analyzer. The shifts of resonance frequencies and parameters with temperature starting from 20°C to 100°C in a step of 5°C are noted and results are

given in Fig. 3.6a-j for PZT ceramics and in Fig. 3.7a-j for PMN-PT single crystals, respectively.

The percentage changes in material parameters ($\varepsilon_{33}/\varepsilon_0$, N_{3t}, N_1, k_{33}, k_{31}, d_{33}, d_{31}, Q_M, c_{33}^E) of PMN-PT single crystals from 20°C to 100°C are considerably larger than that of the PZT ceramics. The change in the relative dielectric constant $\varepsilon_{33}^T/\varepsilon_0$ of PZT is +32% (Fig. 3.6a) whereas that of PMN-PT is +140% (Fig. 3.7a). Change in dissipation loss factor tanδ of PZT is +140% (Fig. 3.6b) but that of PMN-PT is –28% (Fig. 3.7b). This shows that the single crystal can maintain a lower dissipation loss of ~1% from 20°C to 100°C. Frequency constants N_{3t} and N_1 of the PZT are quite stable and have less than +0.8% variation (Figs. 3.6c-d) but that of PMN-PT shows a slight decrease (-2.2% in Fig. 3.7c-d). Electromechanical coupling factors k_{33} and k_{31} of PZT slightly decrease by about 2% (Fig. 3.6e-f) and that of PMN-PT drop a little bit more (< -10%, Fig. 3.7e-f). Larger variation (about +30%) in piezoelectric coefficients d_{33} and d_{31} of PMN-PT are observed in Figs. 3.7g-h whereas that of PZT is about +8% (Fig. 3.6g-h). Mechanical quality factor Q_M of PMN-PT is greatly damped (about -60% in Fig. 3.7i) while that of PZT still have a high value with a change from 967 to 580 (Fig. 3.6i). Stiffness c_{33}^E of PZT increases by about 1% (Fig. 3.6j) but that of PMN-PT decreases by about 4% (Fig. 3.7j).

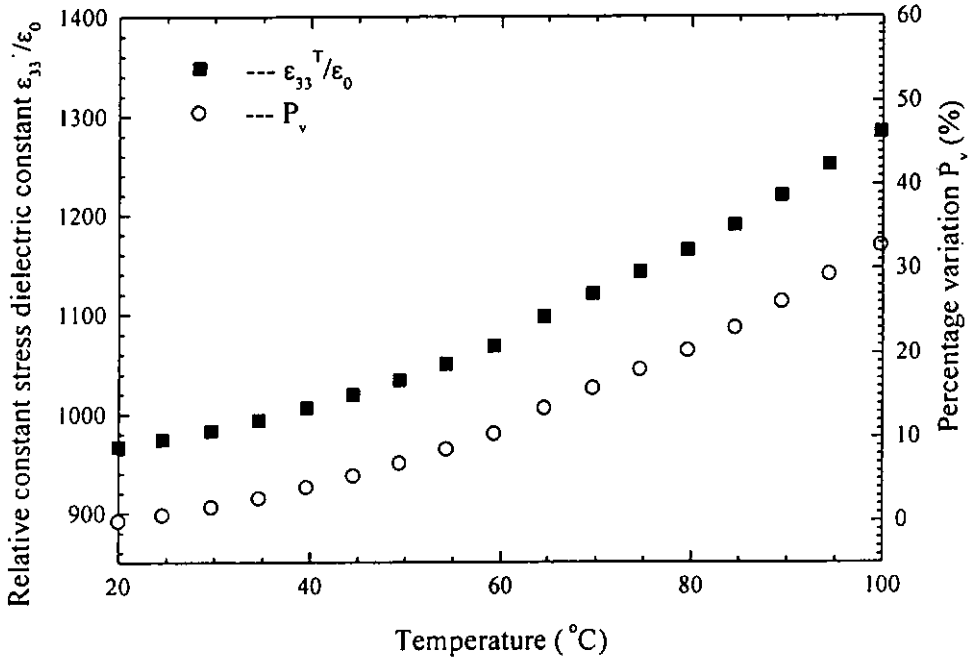

Fig. 3.6a Relative constant stress dielectric constant $\varepsilon_{33}^{T}/\varepsilon_0$ against temperature of PZT 802 ceramic.

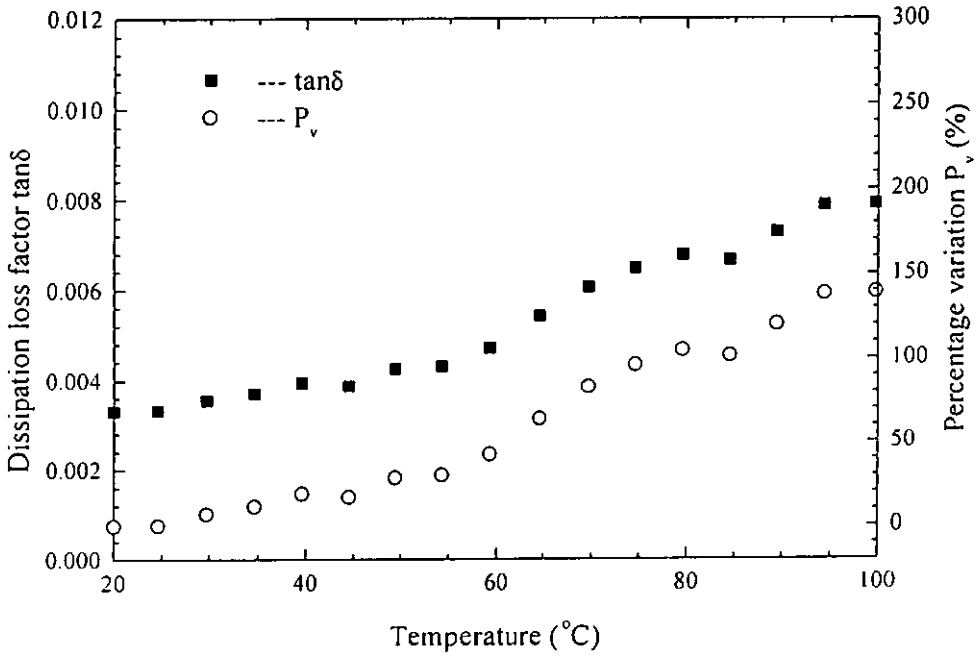

Fig. 3.6b Dissipation loss factor tanδ against temperature of PZT 802 ceramic.

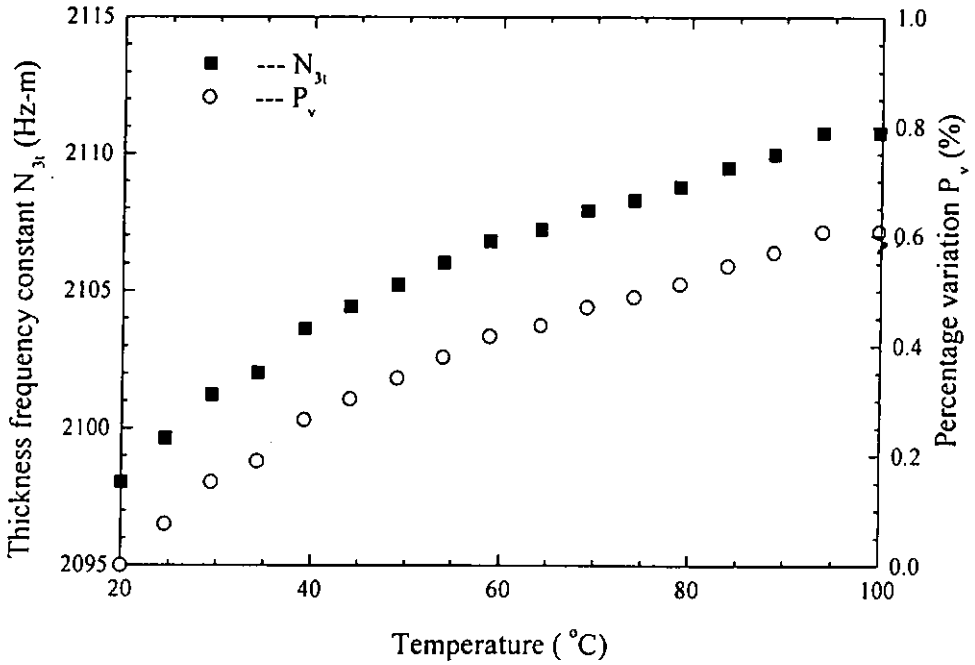

Fig. 3.6c Thickness frequency constant N_{3t} against temperature of PZT 802 ceramic.

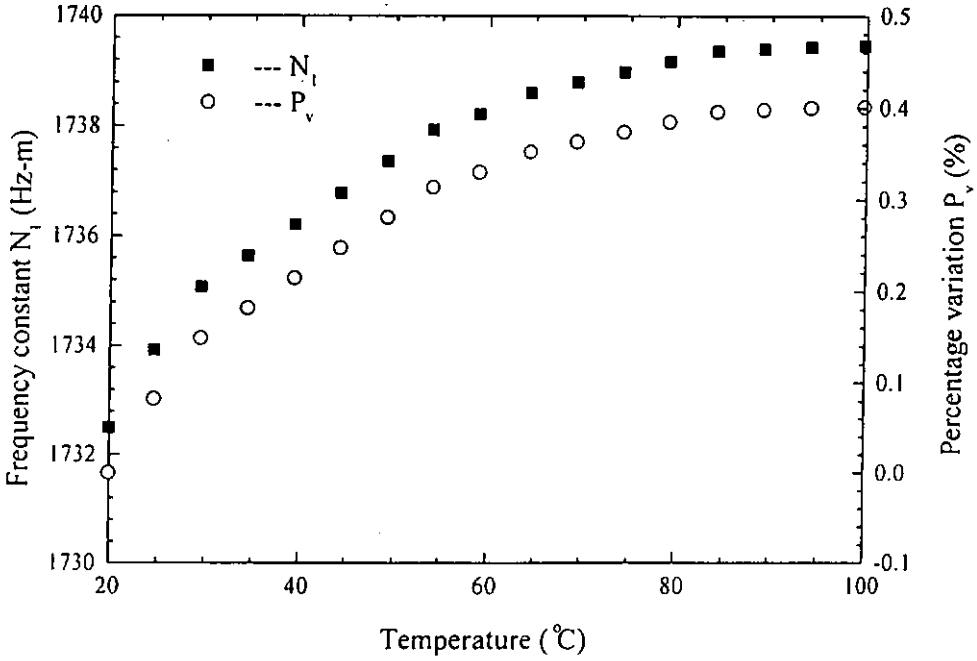

Fig. 3.6d Frequency constant N_1 against temperature of PZT 802 ceramic.

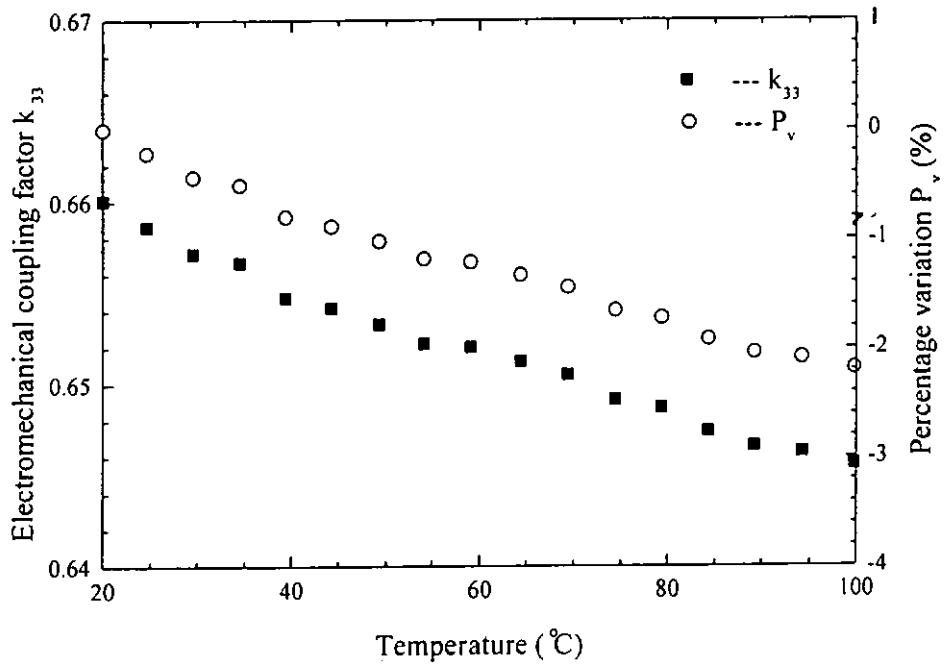

Fig. 3.6e Electromechanical coupling factor k_{33} against temperature of PZT 802 ceramic.

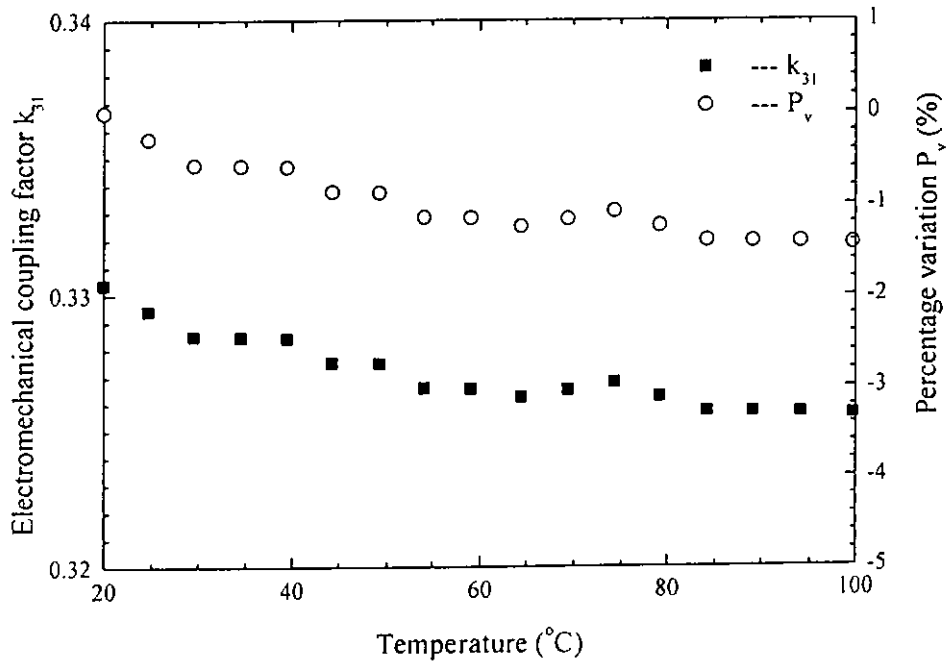

Fig. 3.6f Electromechanical coupling factor k_{31} against temperature of PZT 802 ceramic.

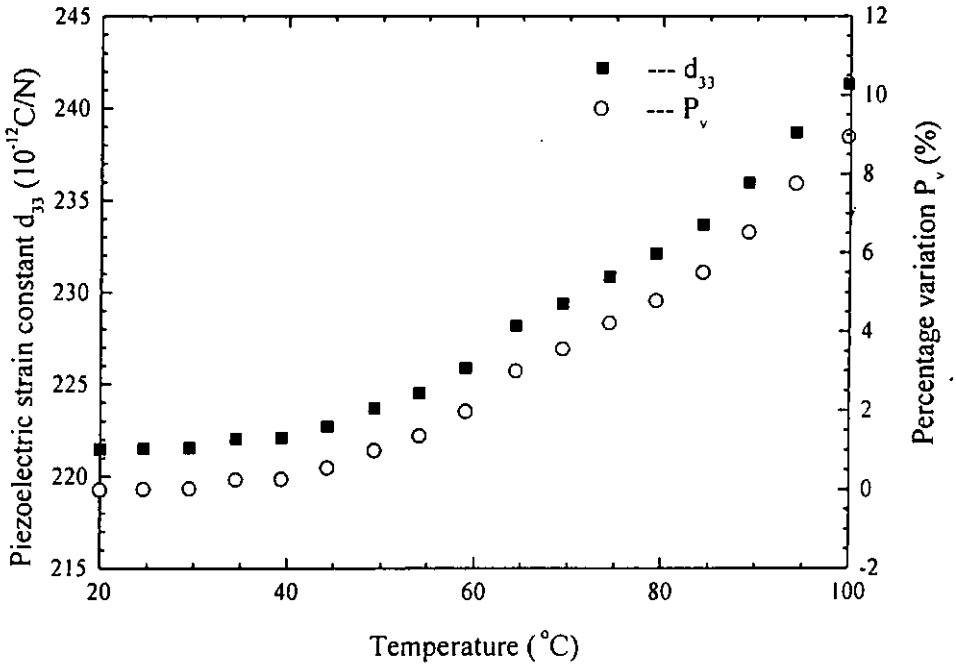

Fig. 3.6g Piezoelectric strain constant d_{33} against temperature of PZT 802 ceramic.

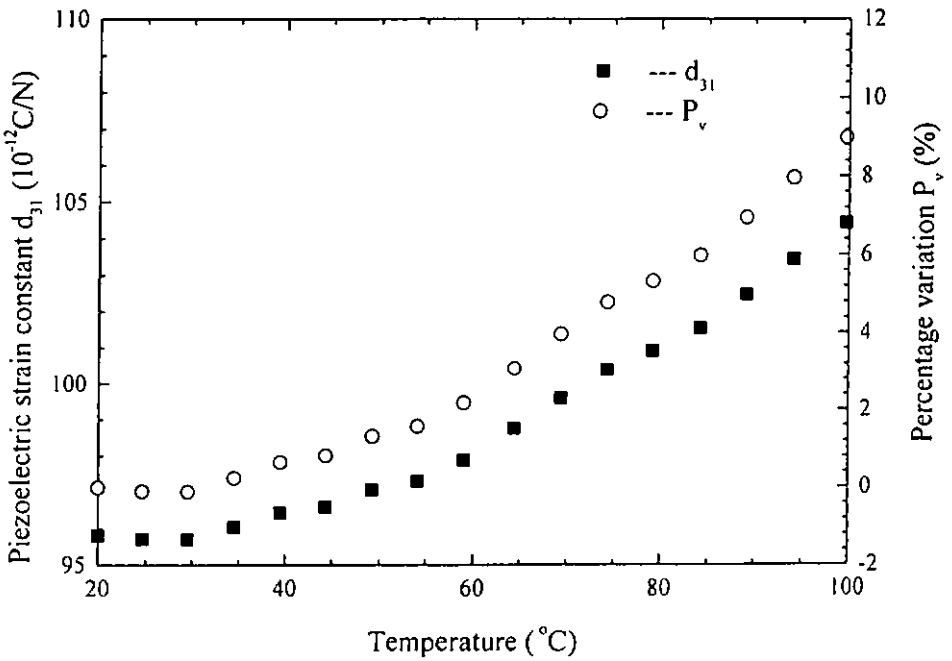

Fig. 3.6h Piezoelectric strain constant d_{31} against temperature of PZT 802 ceramic.

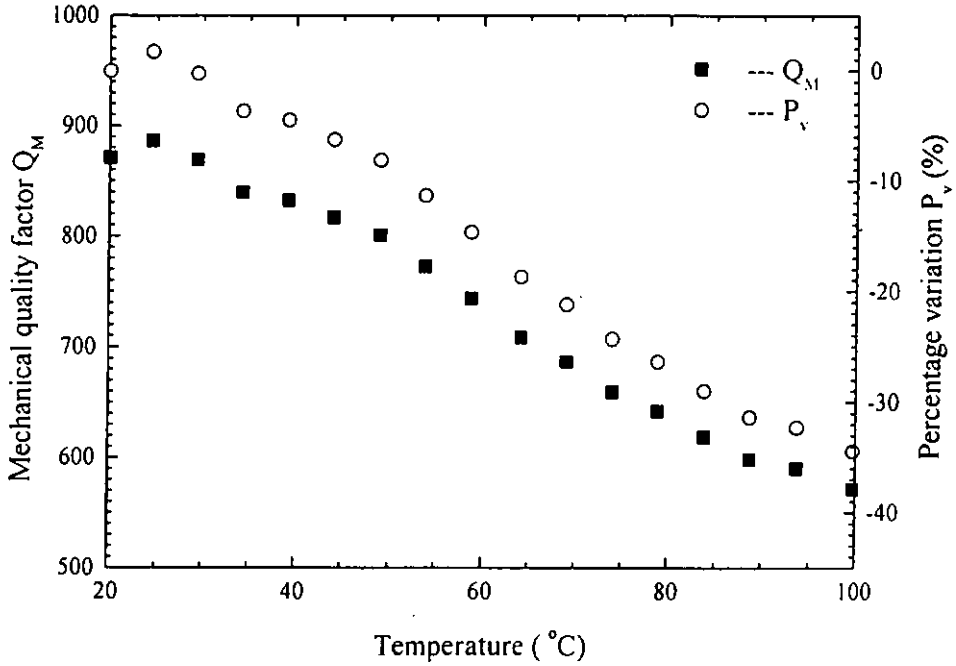

Fig. 3.6i Mechanical quality factor Q_M against temperature of PZT 802 ceramic.

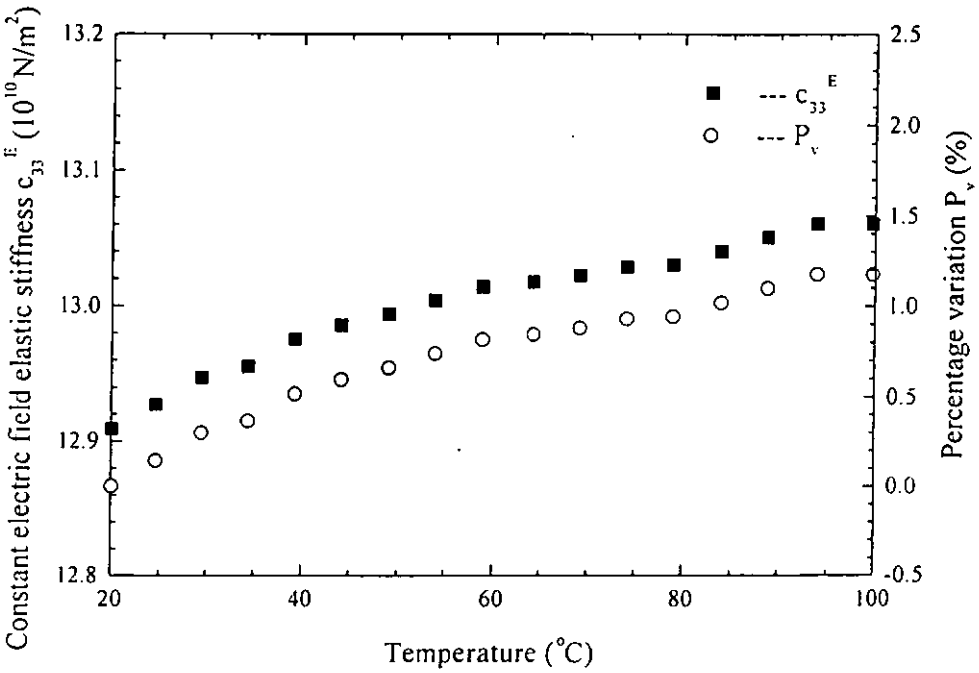

Fig. 3.6j Constant electric field elastic stiffness c_{33}^E against temperature of PZT 802 ceramic.

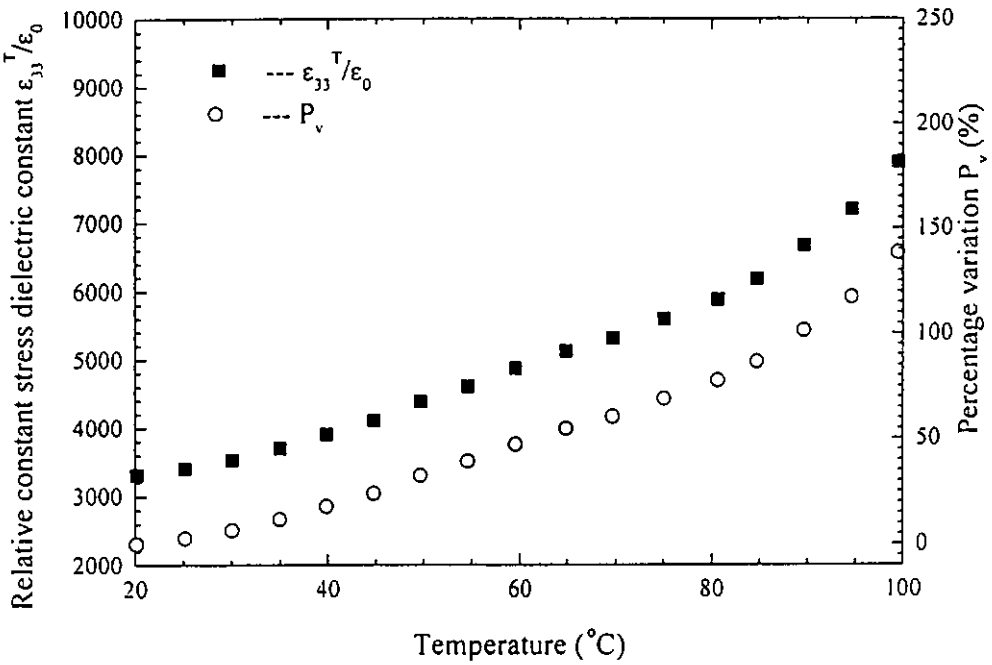

Fig. 3.7a Relative constant stress dielectric constant $\varepsilon_{33}^T/\varepsilon_0$ against temperature of PMN-PT single crystal.

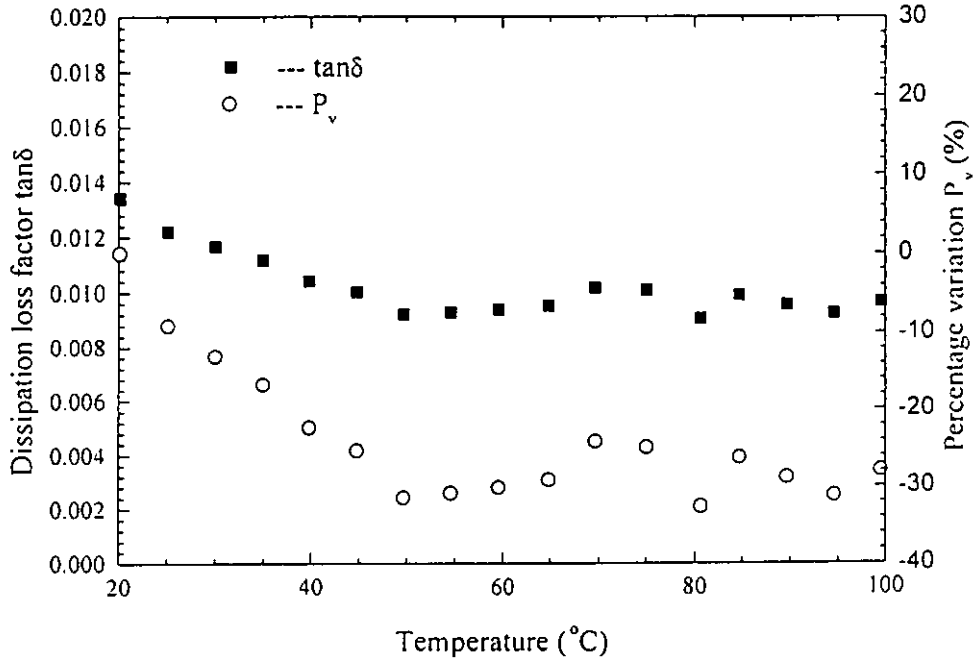

Fig. 3.7b Dissipation loss factor tanδ against temperature of PMN-PT single crystal.

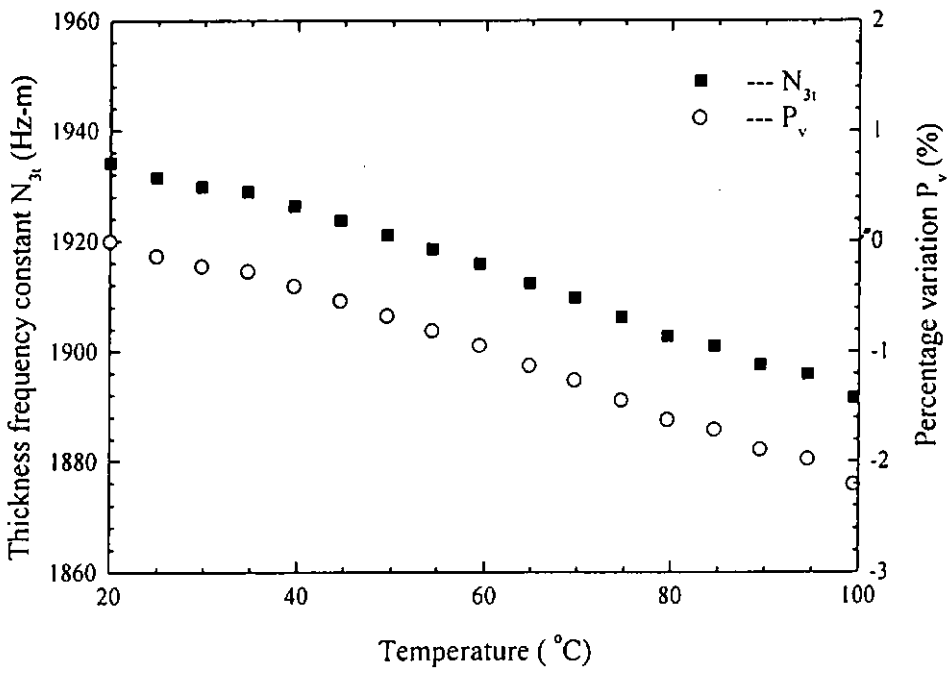

Fig. 3.7c Thickness frequency constant N_{3t} against temperature of PMN-PT single crystal.

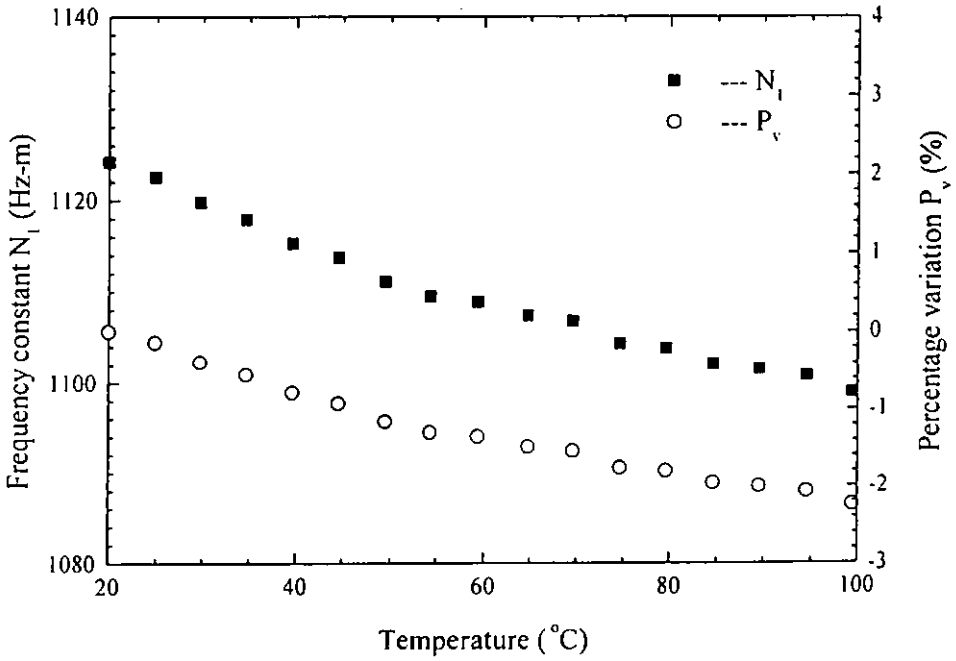

Fig. 3.7d Frequency constant N_l against temperature of PMN-PT single crystal.

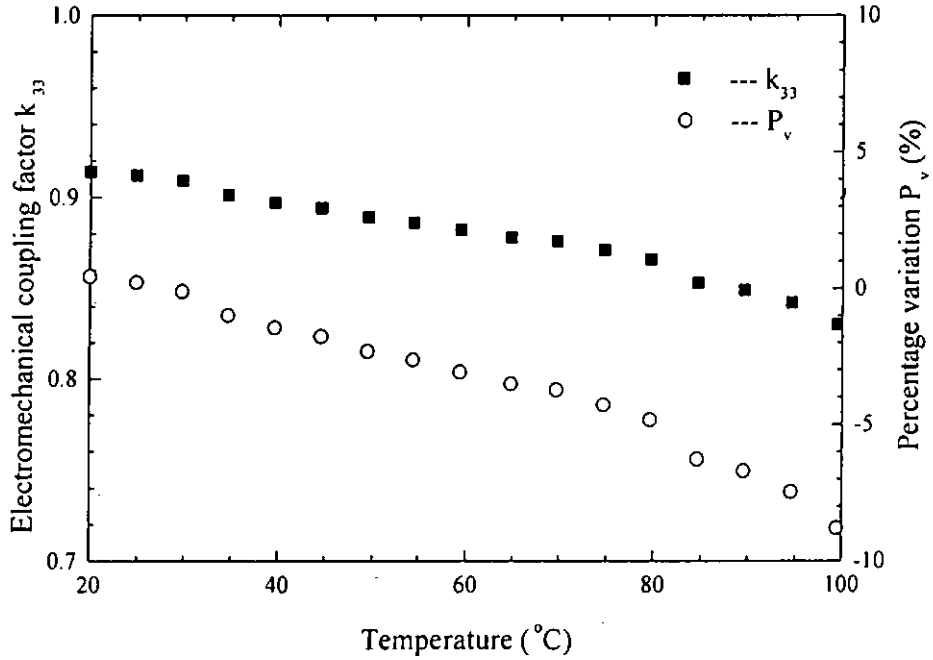

Fig. 3.7e Electromechanical coupling factor k_{33} against temperature of PMN-PT single crystal.

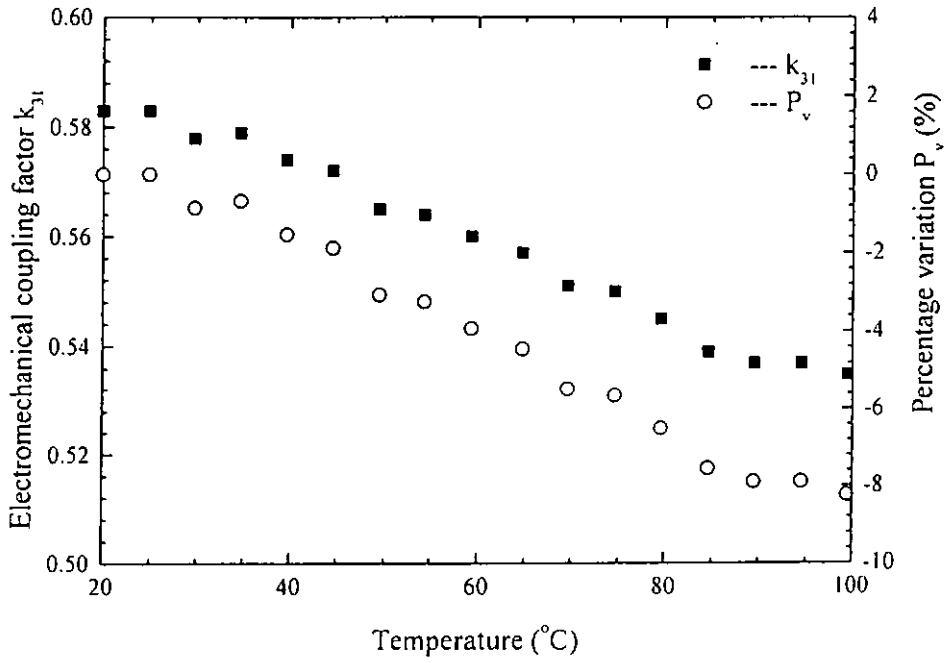

Fig. 3.7f Electromechanical coupling factor k_{31} against temperature of PMN-PT single crystal.

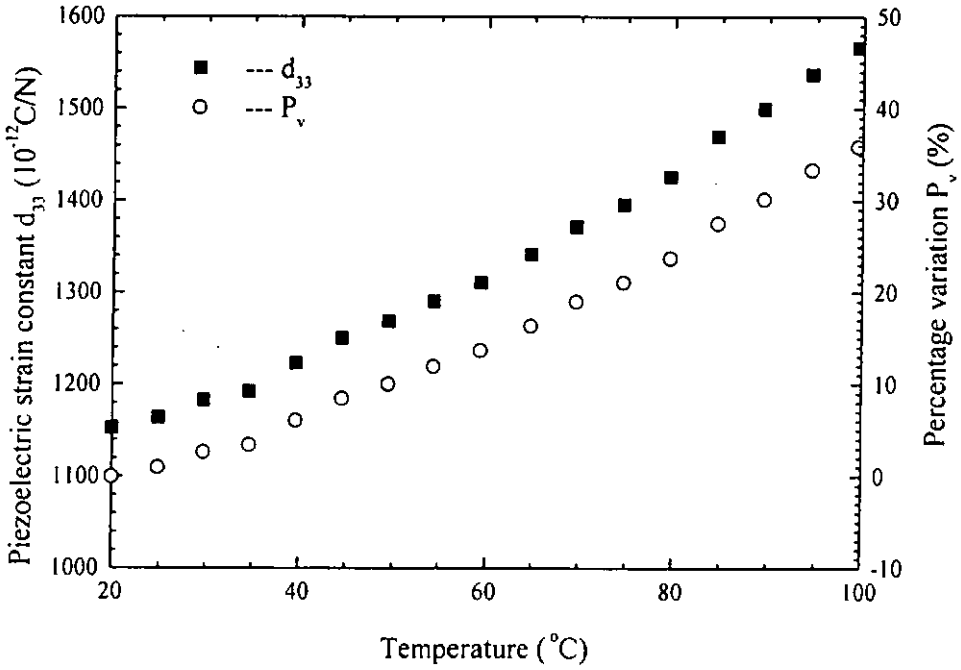

Fig. 3.7g Piezoelectric strain constant d_{33} against temperature of PMN-PT single crystal.

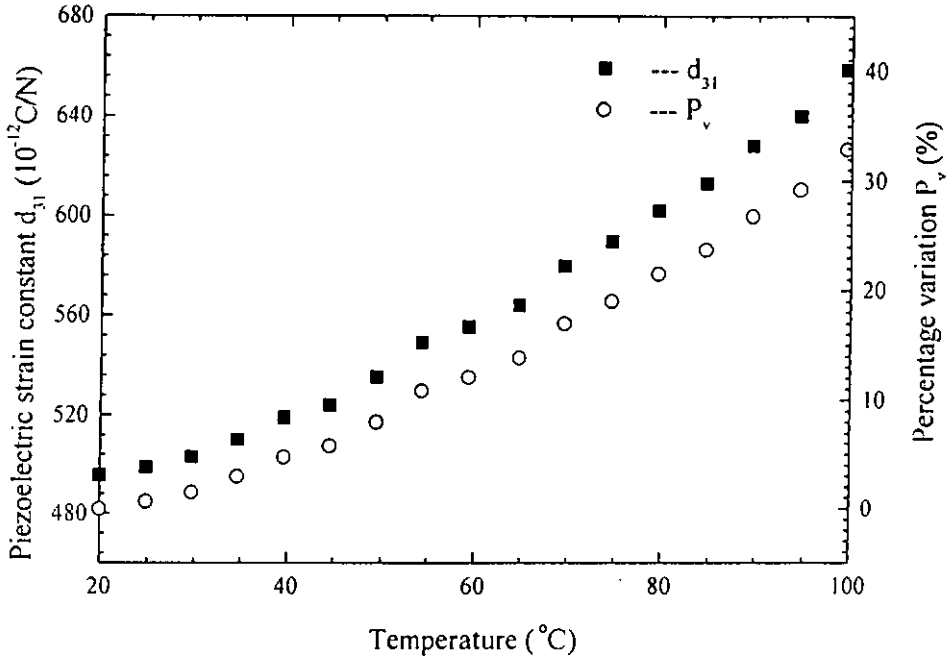

Fig. 3.7h Piezoelectric strain constant d_{31} against temperature of PMN-PT single crystal.

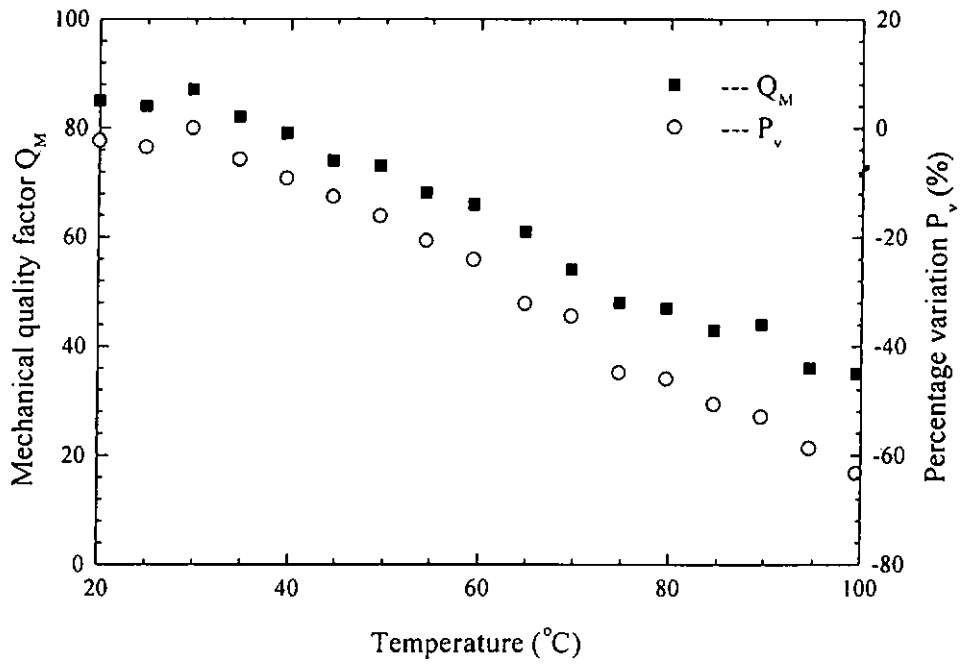

Fig. 3.7i Mechanical quality factor Q_M against temperature of PMN-PT single crystal.

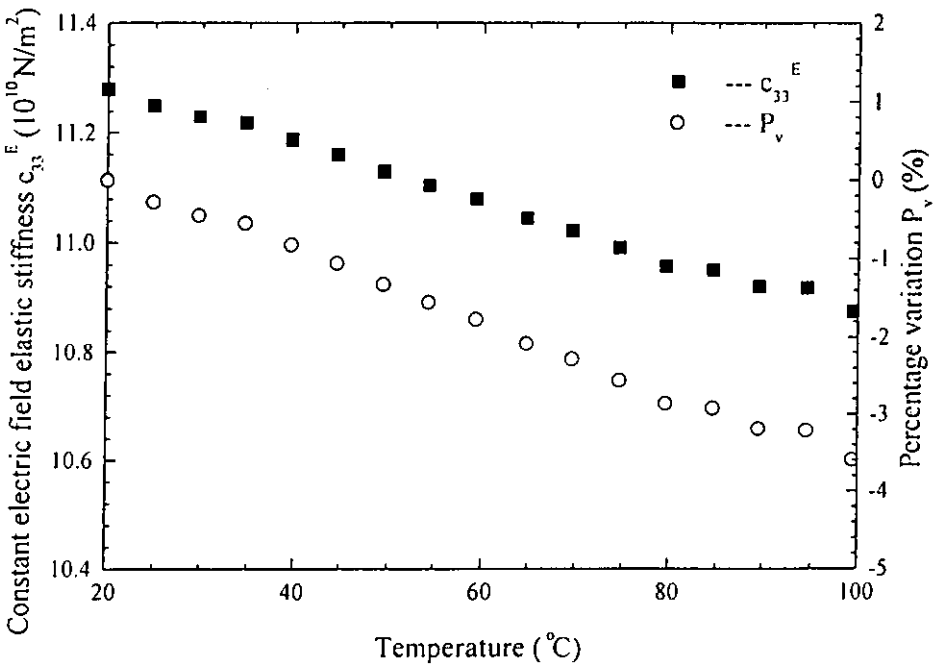

Fig. 3.7j Constant electric field elastic stiffness c_{33}^E against temperature of PMN-PT single crystal.

CHAPTER 4

CHARACTERIZATION OF EPOXY

4.1 Introduction

In the present study, composite materials made of piezoelectric material and epoxy were fabricated. In using these composites to make ultrasonic wire bonding transducers, heat generated by the piezoelectric material during normal operation may cause problem of reliability because of the unknown changes in the properties of the ceramic and epoxy with different temperature. In Chapter 3, the variation of properties in PZT with temperature has been studied. In this chapter, the elastic and electrical properties of the epoxy were measured under different temperatures. Acoustic velocity of the epoxy was measured by using an ultrasonic immersion method [Read, 1978] and elastic constant was calculated by density x $(\text{velocity})^2$. Relative dielectric constant and dissipation loss of the epoxy were also measured. Epoxy type LW 5157 with hardener HY 5159 (mixed in a weight ratio of 10:1 and cured at 40°C for 12 hours) was selected as it can withstand a high temperature up to 120°C and has good wear resistance.

4.2 Experimental setup and sample preparation

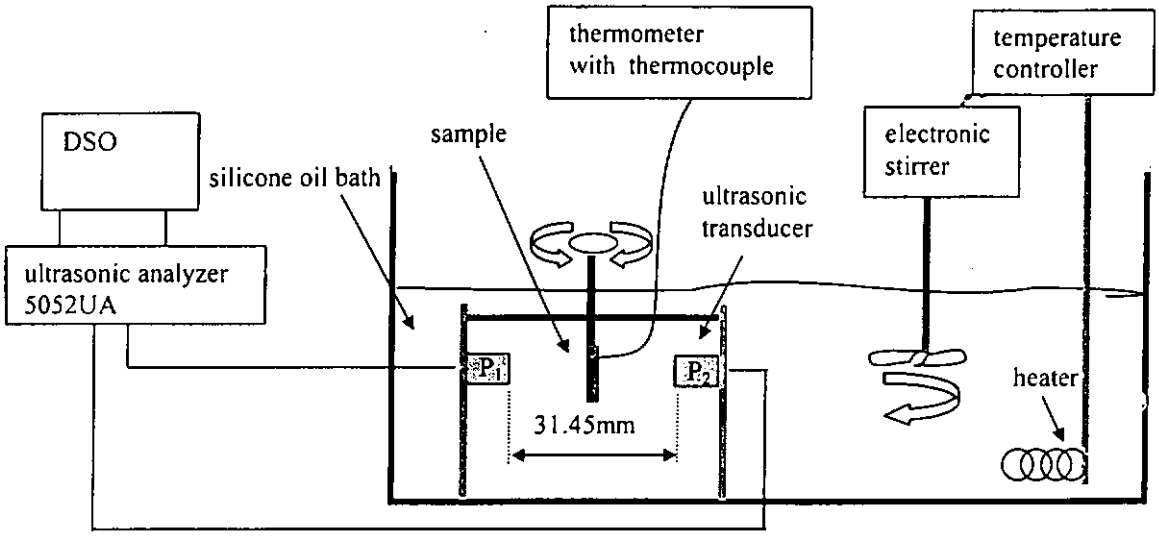

Fig. 4.1 Schematic setup of an ultrasonic immersion method.

The schematic setup is shown in Fig. 4.1. A sample immersed in a silicone oil bath was mounted in a holder which was located in the middle of a pair of 10 MHz ultrasonic transducers of 10 mm diameter. One of the transducers acted as the transmitter P_1 and the other one acted as the receiver P_2. The separation between P_1 and P_2 was 31.45 mm. P_1 was driven by a broadband excitation which was a sharp pulse generated by a Panametrics 5052UA ultrasonic analyzer.

Three epoxy samples with cross sectional area of 15 mm x 20 mm and thickness of 1.2 mm, 1.4 mm and 1.6 mm, respectively, were used in the measurement. These samples had been preheated at 100°C for 10 hours before measurements.

4.3 Measurement of longitudinal wave velocity

The method for measuring the longitudinal velocity was described by [Read, 1978]. When the wave pulses passed through the sample, both longitudinal and shear waves may be generated in the sample depending on the angle of incidence. For the measurement of longitudinal wave velocity, the ultrasonic wave pulse incident normally on the sample and after passing through the sample, was picked up by the receiver. By rotating the sample holder, a maximum wave amplitude can be obtained at normal incidence. The ultrasonic velocity of sound υ_l in the sample was calculated using

$$\Delta T = t\left(\frac{1}{\upsilon_{oil}} - \frac{1}{\upsilon_l}\right) \tag{4.1}$$

where ΔT is a difference in arrival time between wave pulses with and without the sample. t is the sample thickness. υ_{oil} is the velocity of sound in oil that can be calculated from the arrival time in the absence of the sample. By varying the temperature of the oil, the velocity of sound in oil and in the samples were measured as a function of temperature.

The acoustic impedance Z is given by

$$Z = velocity \times density \tag{4.2}$$

Density of the sample was determined using the Archimedes' principle.

4.4 Measurement of shear wave velocity

In order to measure the shear wave velocity [Read, 1978], the sample was rotated to a critical angle such that the total reflection of the longitudinal wave took place and only the shear wave can propagates through the sample as shown in Fig. 4.2. By rotating the sample slowly, the shear wave would appear at a later time than the longitudinal wave and increase in amplitude until it attains the maximum value. At the same time, the longitudinal wave decreases in amplitude until it disappears.

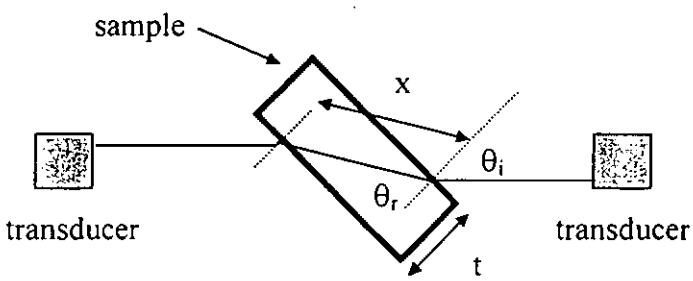

Fig. 4.2 Geometry of shear wave propagation.

To calculate the shear wave velocity υ_s , according to Snell's law,

$$\frac{\sin\theta_i}{\sin\theta_r} = \frac{\upsilon_{oil}}{\upsilon_s} \tag{4.3}$$

where θ_i is the angle of incidence, θ_r is the angle of refraction, x is the path length through the sample.

The path length x through the sample is

$$x = \frac{t}{\cos\theta_r} = t(1-(\frac{\upsilon_s \sin\theta_i}{\upsilon_{oil}})^2)^{-\frac{1}{2}} \tag{4.4}$$

Finding x by solving Eq. (4.4) and the time shift ΔT_s measured from the oscilloscope, the shear wave velocity υ_s can be calculated by

$$\Delta T_s = x(\frac{1}{\upsilon_s} - \frac{1}{\upsilon_{oil}}) \tag{4.5}$$

4.5 Measurement of the attenuation coefficient

In order to avoid the influence of ultrasonic wave diffraction and reflection, several samples of the same cross sectional area but with different thicknesses were used to measure the wave amplitude. The amount of reflections and diffractions can thus be assumed to be the same in the measurements, and if absorption in oil is neglected, the difference in amplitude observed in two samples is due solely to the absorption occurring in a thickness equal to the difference in the thickness of the two samples. Attenuation coefficient α was given by [Hartmann, 1980]

$$\alpha(dBcm^{-1}) = 20\log(\frac{A_1}{A_2})/(t_2 - t_1) \tag{4.6}$$

where A_1 and A_2 are the amplitudes measured in samples of thickness t_1 and t_2

To convert α (dB cm^{-1}) to $\alpha(cm^{-1})$ by using

$$\alpha(dBcm^{-1}) = 10\log(e^{2\alpha(cm^{-1})}) \tag{4.7}$$

Mechanical Q factor can be calculated using

$$Q_L = \frac{2\pi f}{2\upsilon_l \alpha} \tag{4.8}$$

where f is the applied frequency of ultrasonic wave. υ_l is the longitudinal wave velocity of the sample.

4.6 Elastic properties of epoxy

For an isotropic solid, the longitudinal and shear sound velocity determined are related to the elastic constants by the relations [Read, 1978]

$$\upsilon_l = \{(K + 4G/3)/\rho\}\}^{\frac{1}{2}} \tag{4.9}$$

$$\upsilon_s = (G/\rho)^{\frac{1}{2}} \tag{4.10}$$

where K is the bulk modulus, G is the shear modulus and ρ is the density. Young's modulus Y and Poisson's ratio σ can be determined from K and G using

$$Y = 3G/\{1 + G/(3K)\} \tag{4.11}$$

$$\sigma = \frac{1}{2} - \frac{Y}{6K} \tag{4.12}$$

Since the epoxy is isotropic, the three coordinate axes, x,y,z and the three planes yz, xz, xy are equivalent. If tensor notation is used, the stiffness matrix c_{ij} of the epoxy is

$$c_{ij} = \begin{pmatrix} c_{11} & c_{12} & c_{12} & 0 & 0 & 0 \\ c_{12} & c_{11} & c_{12} & 0 & 0 & 0 \\ c_{12} & c_{12} & c_{11} & 0 & 0 & 0 \\ 0 & 0 & 0 & c_{44} & 0 & 0 \\ 0 & 0 & 0 & 0 & c_{44} & 0 \\ 0 & 0 & 0 & 0 & 0 & c_{44} \end{pmatrix} \tag{4.13}$$

After measuring υ_l and υ_s, stiffness c_{11}, c_{12} and c_{44} were calculated by

$$c_{11} = \rho\upsilon_l^2 = K + 4G/3 \tag{4.14}$$

$$c_{12} = \rho\upsilon_l^2 - 2\rho\upsilon_s^2 = K - 2G/3 \tag{4.15}$$

$$c_{44} = G = \rho\upsilon_s^2 \tag{4.16}$$

Compliance s_{11}, s_{12} and s_{44} were calculated from c_{11}, c_{12} and c_{44} by

$$s_{11} = \frac{(c_{11} + c_{12})}{(c_{11} - c_{12})(c_{11} + 2c_{12})} \tag{4.17}$$

$$s_{12} = \frac{-c_{12}}{(c_{11} - c_{12})(c_{11} + 2c_{12})} \tag{4.18}$$

$$s_{44} = \frac{1}{c_{44}} \tag{4.19}$$

The Poisson's ratio is defined as

$$\sigma = \frac{-s_{12}}{s_{11}} = \frac{1 - 2(\frac{\upsilon_s}{\upsilon_l})^2}{2\{1 - (\frac{\upsilon_s}{\upsilon_l})^2\}} \tag{4.20}$$

Table 4.1 Material properties of epoxy measured at room temperature.

Density	ρ	(kg/m^3)	1200
Relative dielectric constant	$\varepsilon/\varepsilon_0$		4.21
Dissipation loss factor	$\tan\delta$		0.005
Longitudinal wave velocity	υ_L	(m/s)	2658
Shear wave velocity	υ_S	(m/s)	1416
Longitudinal acoustic impedance	Z_L	(Mrayl)	3.19
Shear acoustic impedance	Z_S	(Mrayl)	1.70
Longitudinal stiffness	c_{11}	($10^{10}N/m^2$)	0.85
Shear stiffness	c_{44}	($10^{10}N/m^2$)	0.24
Stiffness in x-y plane	c_{12}	($10^{10}N/m^2$)	0.37
Longitudinal compliance	s_{11}	($10^{-12}m^2/N$)	159.61
Shear compliance	s_{44}	($10^{-12}m^2/N$)	415.57
Compliance in x-y plane	s_{12}	($10^{-12}m^2/N$)	-48.19
Shear modulus	G	($10^{10}N/m^2$)	0.24
Bulk modulus	K	($10^{10}N/m^2$)	0.53
Young's modulus	Y	($10^{10}N/m^2$)	0.63
Mechanical quality factor	Q_M		24.5
Poisson's ratio	σ		0.30

4.7 Thermal stability of epoxy

With the ultrasonic immersion method, elastic properties of epoxy were measured as a function of temperature. Each measurement was taken when the sample was heat up. The temperature changes from 20°C to 100°C. The temperature change was controlled to ± 0.1°C. The acoustic velocities of oil and the epoxy sample are given as a function of temperature in Figs. 4.3a-4.3c. Other parameters were calculated and shown in Figs. 4.3d-4.3j. The change of elastic stiffness in the epoxy (-20% at 100°C in Fig. 4.3e-f) is large compared with that of PZT ceramic (+1.2% at 100°C in Fig. 3.6j) and PMN-PT single crystal (-3.8% at 100°C in Fig. 3.7j). The Young's modulus and shear modulus dropped rapidly with the temperature as shown in Fig. 4.3g and Fig. 4.3h whereas the Poisson's ratio σ shows a 5% variation (Fig. 4.3j). The mechanical quality factor Q_M (Fig. 4.3i) is quite constant below 80°C but decreases rapidly at higher temperature.

On the other hand, changes of relative dielectric constant $\varepsilon/\varepsilon_0$ and the dissipation loss factor $\tan\delta$ of the epoxy with temperature were also measured. The sample was connected to a HP4194A impedance gain phase analyzer and was heated inside a computer controlled oven from 20°C to 100°C in step of 5°C in the measurement. The temperature change was controlled to ±0.1°C. From Figs. 4.4a and 4.4b, the relative dielectric constant $\varepsilon/\varepsilon_0$ increases almost linearly with temperature. Except for 1 kHz, the dissipation loss factor measured at different frequencies decreases with increase in temperature. The loss factor shown remains below 0.03 and no relaxation

peak is observed . In terms of the overall performance of the epoxy, it is a suitable material for fabrication of composites for transducer applications.

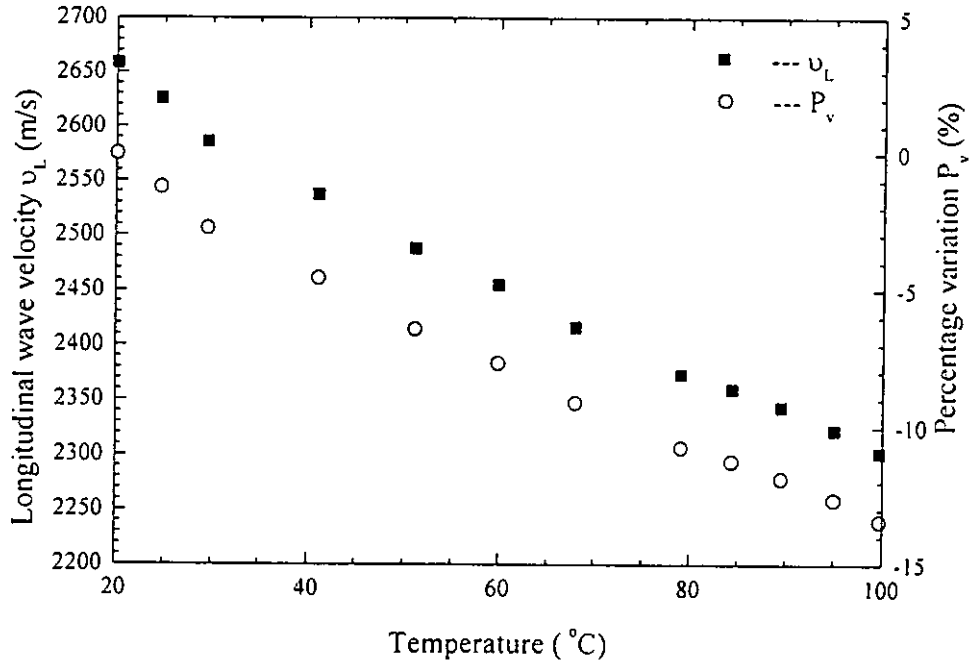

Fig. 4.3a Longitudinal wave velocity υ_L against temperature.

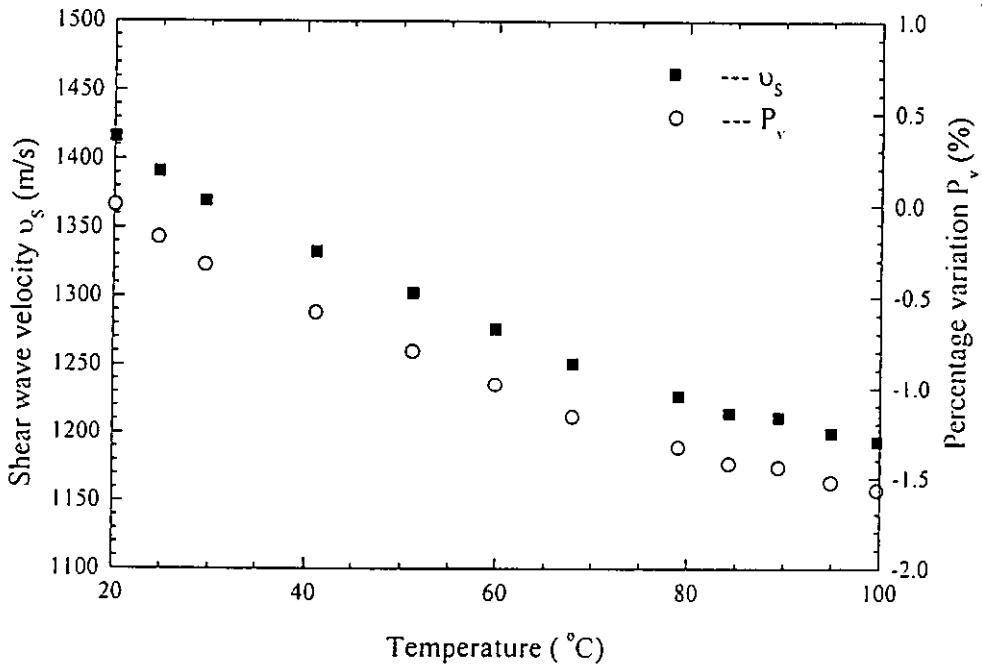

Fig. 4.3b Shear wave velocity υ_S against temperature.

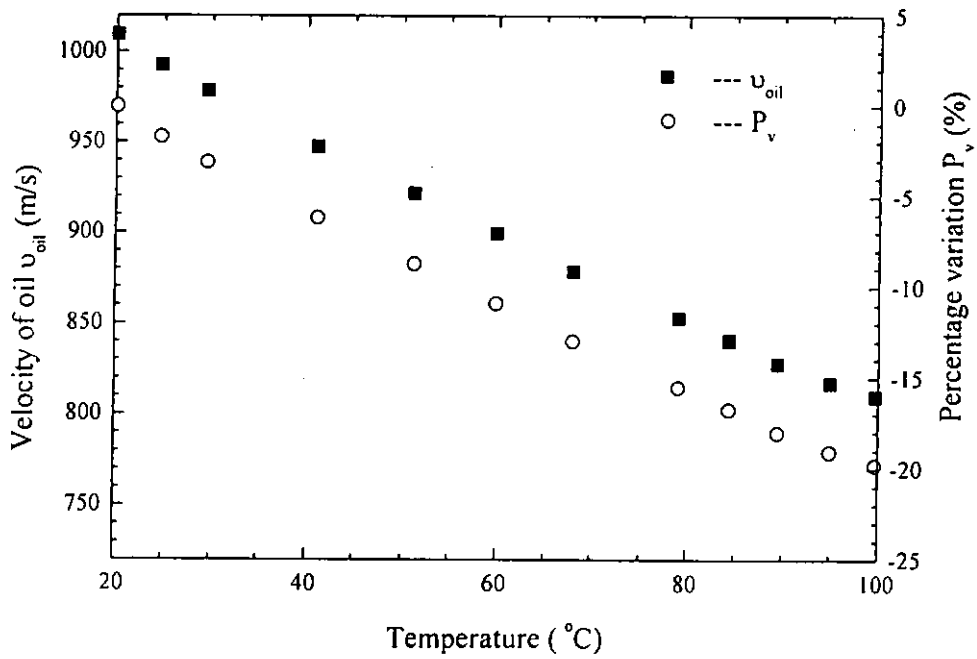

Fig. 4.3c Velocity of oil υ_{oil} against temperature.

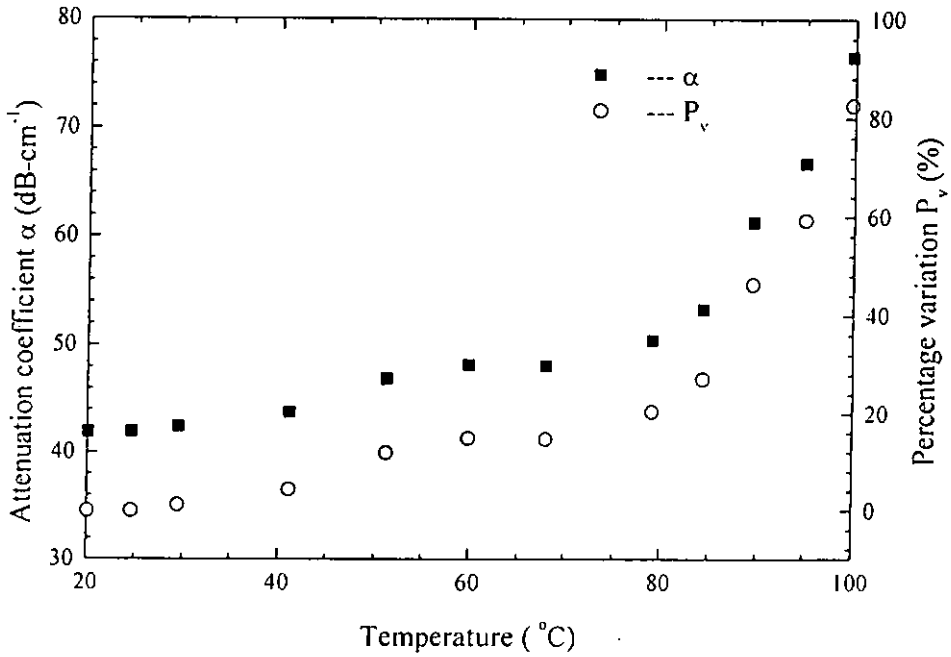

Fig. 4.3d Attenuation coefficient α against temperature.

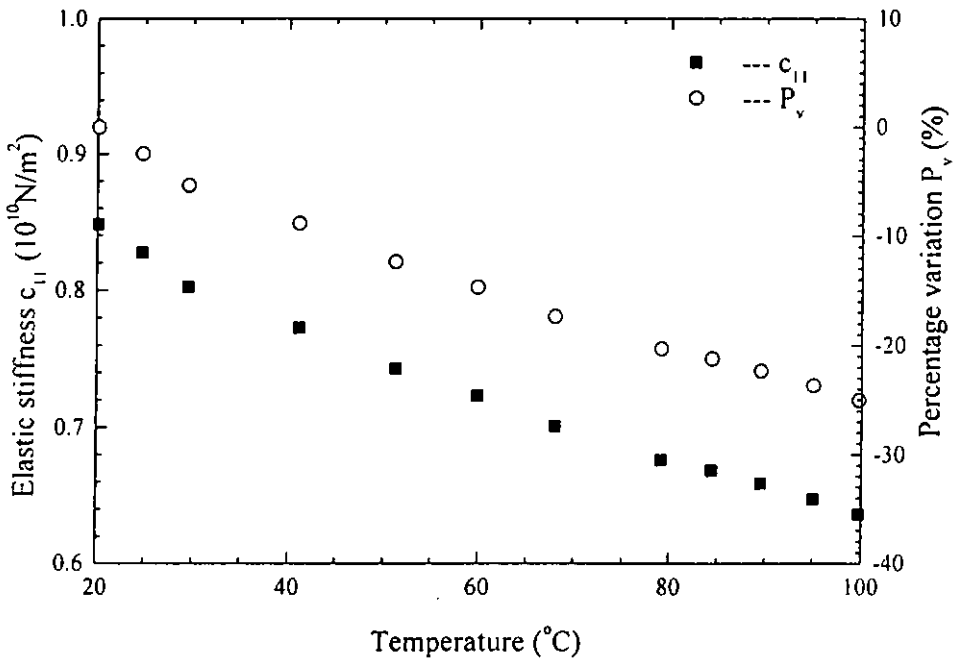

Fig. 4.3e Elastic stiffness c_{11} against temperature.

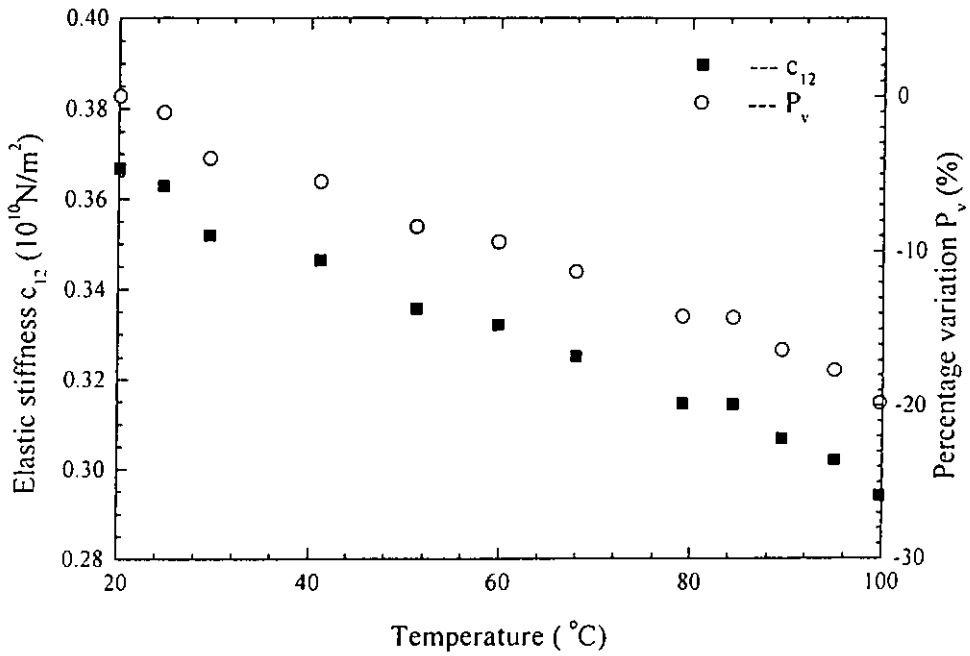

Fig. 4.3f Elastic stiffness c_{12} against temperature.

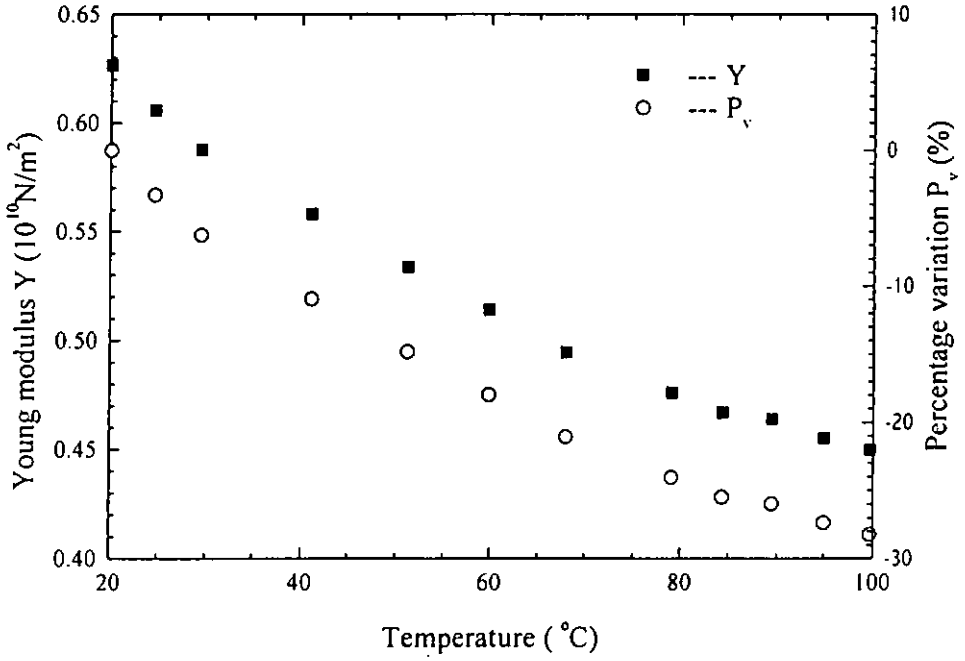

Fig. 4.3g Young's modulus Y against temperature.

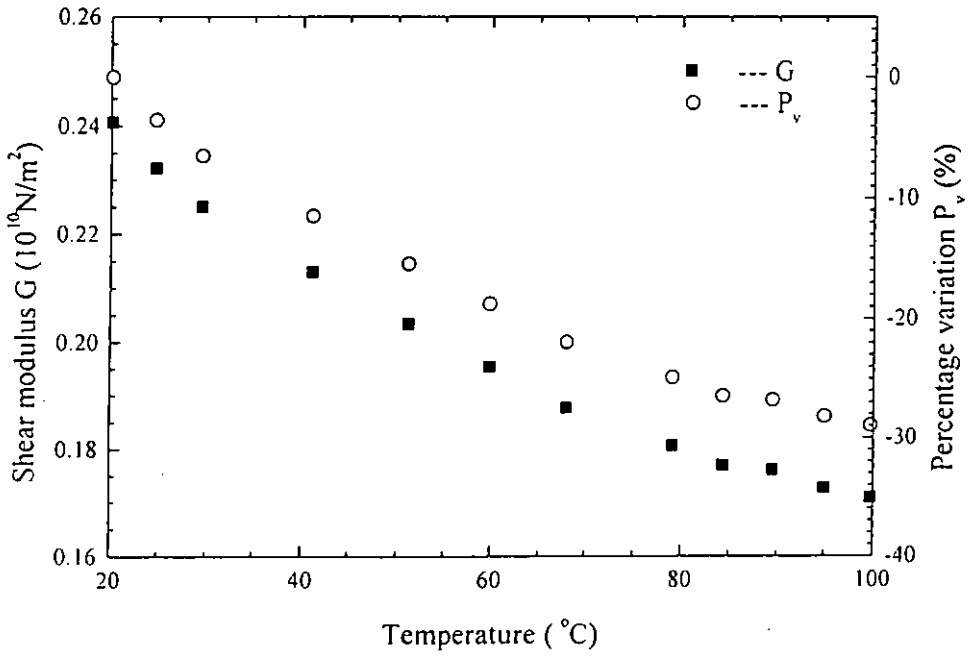

Fig. 4.3h Shear modulus G against temperature.

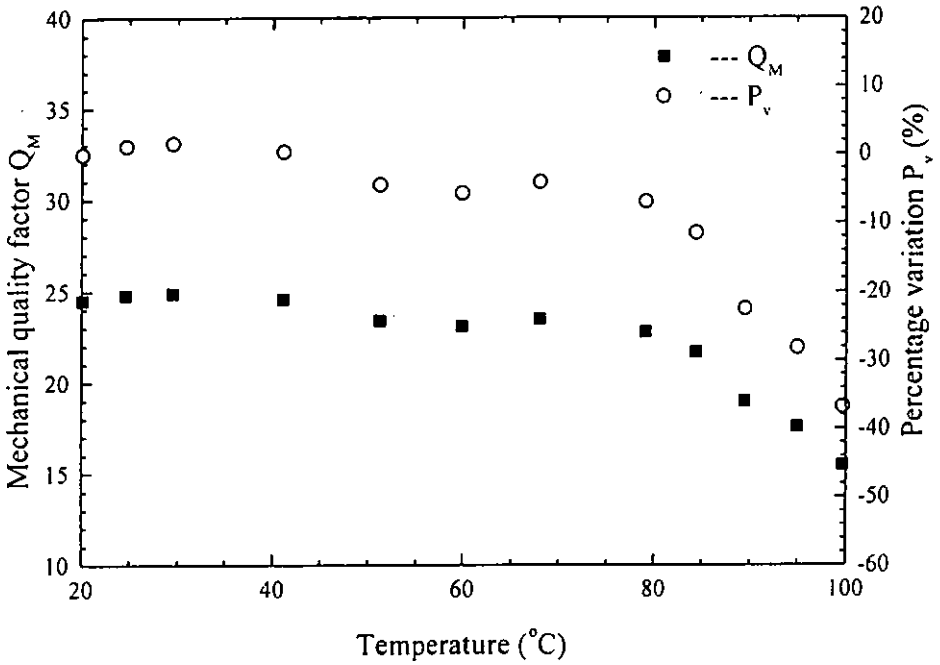

Fig. 4.3i Mechanical quality factor Q_M against temperature.

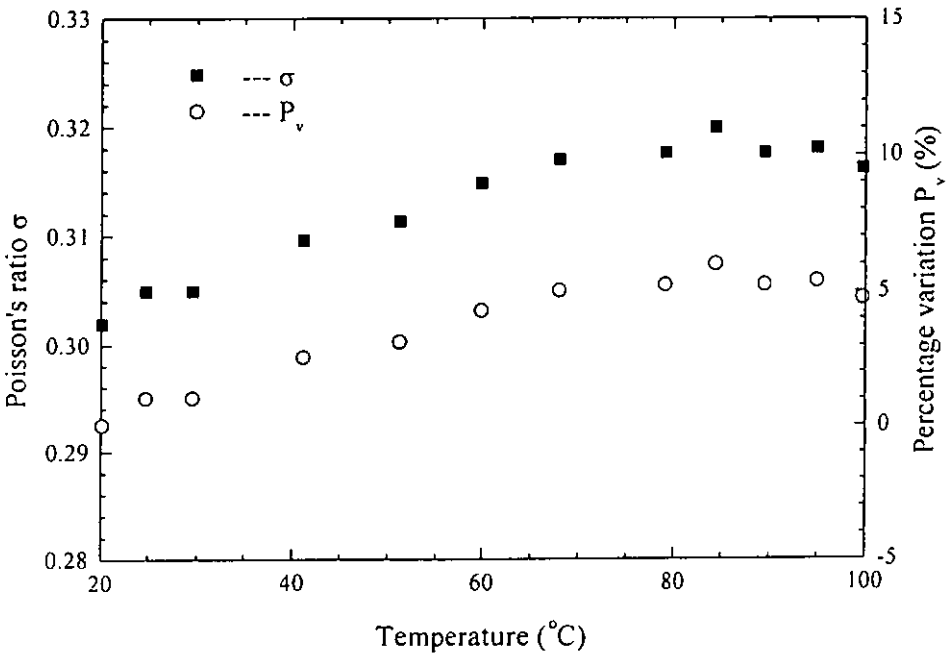

Fig. 4.3j Poisson's ratio σ against temperature.

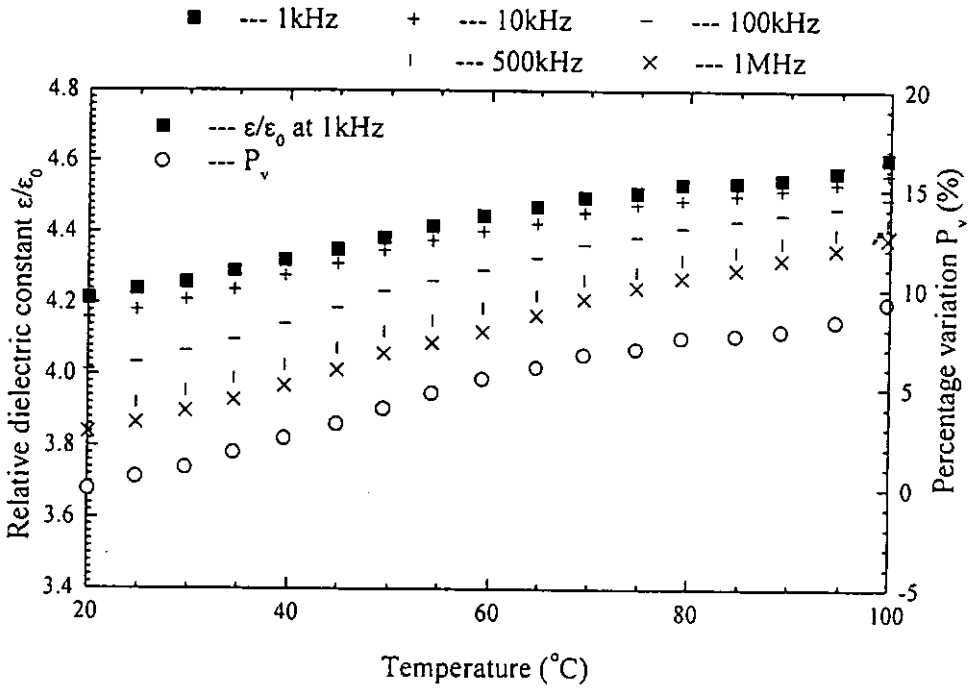

Fig. 4.4a Relative dielectric constant $\varepsilon/\varepsilon_0$ against temperature.

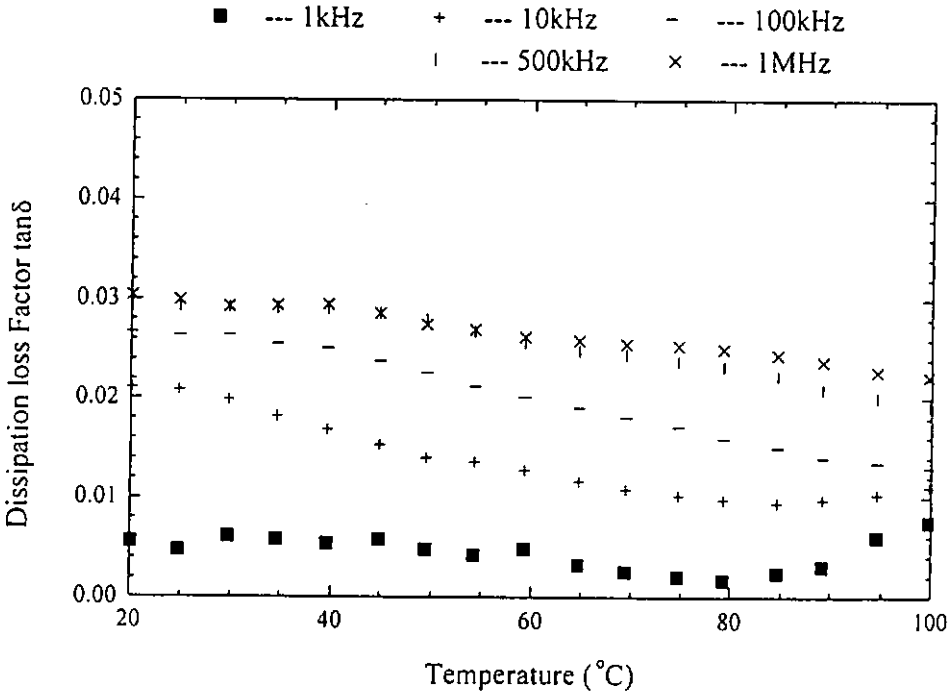

Fig. 4.4b Dissipation loss factor tanδ against temperature.

CHAPTER 5

MEASUREMENT OF PIEZOELECTRIC AND HYDROSTATIC CHARGE COEFFICIENTS

5.1 Introduction

Piezoelectric coefficients d_{33} and d_{31} of PMN-PT single crystals and the PZT 802 ceramics were determined by using an optical heterodyne interferometer to measure the strain induced by an applied electric field. The method used shows great promise because there is no limitation on the dimension of the samples required and it can be used to detect a displacement of 0.1 nm or less [Royer, 1992]. Other method such as the resonance technique described in the previous chapter can also be used to determine the piezoelectric coefficients by measuring the resonance and anti-resonance frequencies of the thin plate and the long bar shown in Fig. 2.9. But the technique is not as direct as the optical measurement in determining the piezoelectric coefficients, as the dielectric and elastic constants had to be determined around the resonant frequencies. Hence, deviation of the piezoelectric coefficients results because of the large change in d_{33} near the resonant frequency of the sample [Royer, 1992]. Here, the hydrostatic charge coefficient d_h of the PMN-PT single crystal and the PZT 802 ceramic was measured by an applied hydrostatic pressure.

5.2 Measurement of piezoelectric coefficients by optical interferometry

A Mach-Zehnder type heterodyne interferometer (SH-120 from B.M. Industries in France) shown in Fig. 5.1 [B.M. heterodyne Probe Manual] was used to measure the displacement in the test samples. A polarized laser beam L with frequency f_L and wavelength λ_L of 632.8 nm is emitted by a 4 mW helium-neon (He-Ne) laser source. The complex amplitude of L is:

$$L = e^{i2\pi \cdot f_L \cdot t} \tag{5.1}$$

After passing through two deflecting mirrors, the laser beam is split into two half-power beams by a cube beam splitter. A reference beam R is directed through a Dove prism into a photodiode. The frequency of probe beam P is shifted by f_B (70 MHz) in a Bragg cell. After reflection from the sample, the phase $\phi(t)$ of probe beam P is modulated by the displacement d(t) of the vibrating surface of the sample. The complex amplitudes of the reference beam R and the probe beam P are:

$$R = e^{i2\pi \cdot f_L \cdot t} \tag{5.2}$$

$$P = p \cdot e^{i2\pi \cdot f_L \cdot t + i2\pi \cdot f_B \cdot t + i\phi(t)} \tag{5.3}$$

$$\phi(t) = \frac{4\pi}{\lambda} d(t) \tag{5.4}$$

After double passing a quarter-wave plate, polarization of the reflected beam S is rotated by 90°. The reflected beam S and reference beam R is mixed and then past through an analyzer at which the polarization of the two orthogonal S & R beams are

oriented by 45°, resulting in the occurrence of interference. The interference of two beams in the photodetector induced photocurrent whose intensity can be expressed as:

$$I(t) = k \cdot \cos(2\pi f_B t + \phi(t)) \tag{5.5}$$

For a pure sinusoidal displacement of the sample with a single frequency ω_0.

$$d(t) = d_0 \sin \omega_0 t \tag{5.6}$$

$$I(t) = k \cdot \cos(\omega_B t + \frac{4\pi}{\lambda} d_0 \sin \omega_0 t) \tag{5.7}$$

which can be expanded into a series of Bessel functions:

$$I(t) = \mathrm{Re}[e^{i\omega_B t} \cdot \{J_0(\frac{4\pi d}{\lambda}) + 2iJ_1(\frac{4\pi d}{\lambda})\sin \omega_0 t + 2J_2(\frac{4\pi d}{\lambda})\sin 2\omega_0 t + ...\}] \tag{5.8}$$

The frequency spectrum of the photocurrent induced in a photodetector contains main components at frequency f_B and sidebands at $f_B \pm f$, where f is frequency of the sample vibration. The absolute vibration displacement can be determined by comparing the components at frequency f_B and $f_B \pm f$ which can be seen in the spectrum analyzer.

If the displacement d is small compared to λ:

$$\frac{J_1(\frac{4\pi d}{\lambda})}{J_0(\frac{4\pi d}{\lambda})} \cong \frac{2\pi d}{\lambda} \tag{5.9}$$

The voltage applied to the sample at 1 kHz was measured by the digital oscilloscope with a 50 Ω termination.

It is noted that the quality of the reflecting surface of the sample is very important. A poor reflecting surface could cause distortion in the interference pattern and introduce severe errors in the determination of small displacements. To overcome the problem, a small mirror was attached to the sample for a reflection surface under low frequency measurement only [Zhao, 1997]. On the other hand, the thin sample was rigidly attached to a thick platform (Fig. 5.2a, Fig. 5.2b) so it is not free to expand or contract in the plane [Zhang, 1988].

In Table 5.1, a square plate and a long bar are used for determining the d_{33} and d_{31}, respectively.

The longitudinal strain S_3 and lateral strain S_1 are calculated by:

$$S_3 = \frac{d_3}{t} \qquad S_1 = \frac{d_1}{L} \tag{5.10}$$

where d_3 and d_1 are the vibration displacements in the thickness and length directions, respectively. t is the thickness and L is the length.

The piezoelectric coefficients d_{33} and d_{31} can be calculated by:

$$d_{31} = -\frac{S_1}{E_3} = \frac{d_1 \cdot t}{V \cdot L} \qquad d_{33} = \frac{S_3}{E_3} = \frac{d_3}{V} \tag{5.11}$$

where E_3 is the applied electric field and V is the voltage.

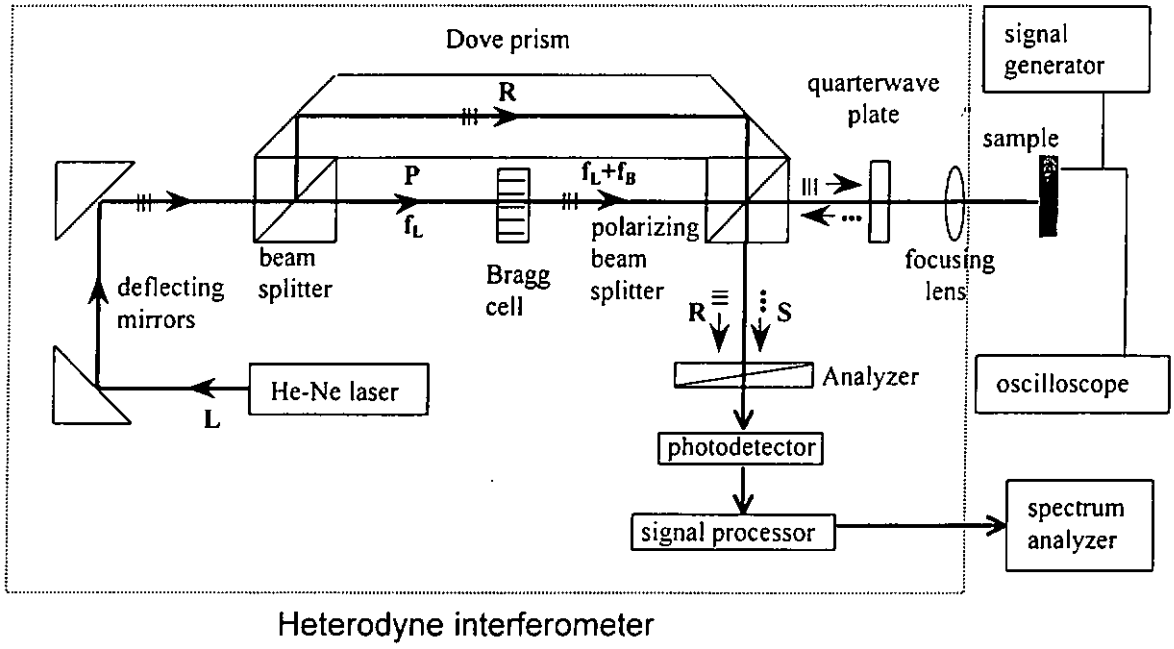

Fig. 5.1 Experimental setup of the optical measurement.

Table 5.1 Dimensions of PMN-PT single crystals and PZT ceramics.

	Dimensions (L x W x t) in mm	
samples	*PMN-PT single crystal*	*PZT ceramic*
square plate	15.45 x 15.48 x 0.87	9.8 x 9.8 x 1.05
long bar	15.07 x 5.64 x 0.87	9.53 x 2.07 x 1.05

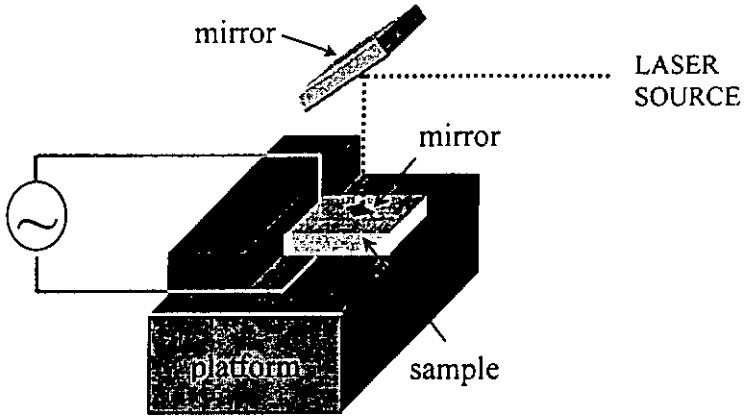

Fig. 5.2a Schematic setup for determining d_{33} of the sample.

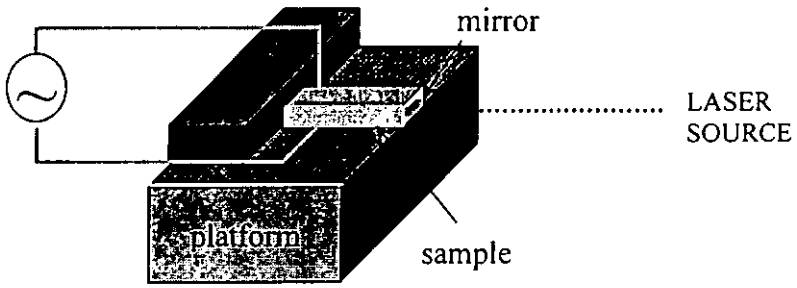

Fig. 5.2b Schematic setup for determining d_{31} of the sample.

5.3 Experimental results of d_{33} and d_{31} measurements

Piezoelectric coefficients d_{33} and d_{31} of PMN-PT single crystals and PZT ceramics were determined by slope of the line in plots of strain against electric field (Figs. 5.3a-b and 5.4a-b). Values calculated by the resonance method are shown in Table 5.2. The calculated values of d_{33} and d_{31} of PMN-PT single crystals and PZT ceramics show reasonable agreements to that measured by interferometry.

Table 5.2 Piezoelectric coefficients of PMN-PT single crystals and PZT ceramics.

	PMN-PT single crystal		PZT ceramic	
Piezoelectric strain constant ($\times 10^{-12}$C/N)	*Laser measurement*	*Resonance method*	*Laser measurement*	*Resonance method*
d_{33}	1127	1158	236	221
d_{31}	-517	-497	-99	-96

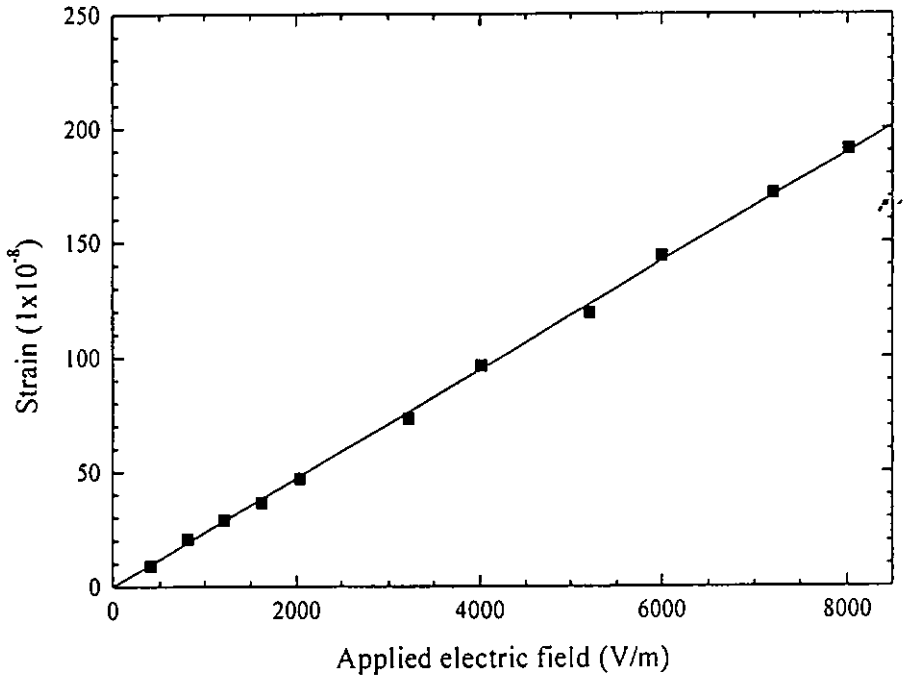

Fig. 5.3a Strain against electric field of a PZT plate measured at 1 kHz (slope of the line = d_{33} coefficient).

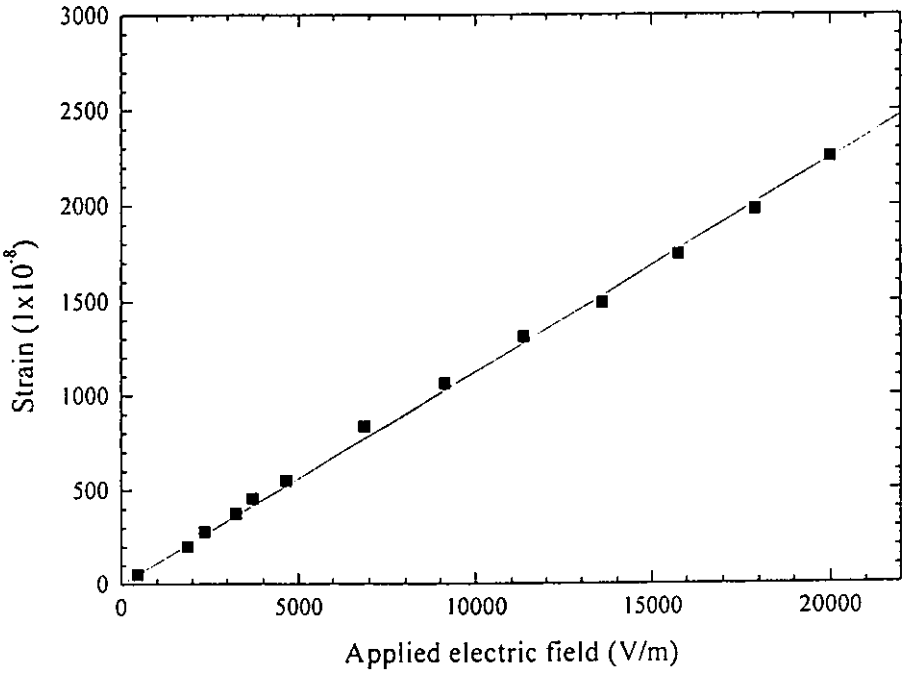

Fig. 5.3b Strain against electric field of a PMN-PT plate measured at 1 kHz (slope of the line = d_{33} coefficient).

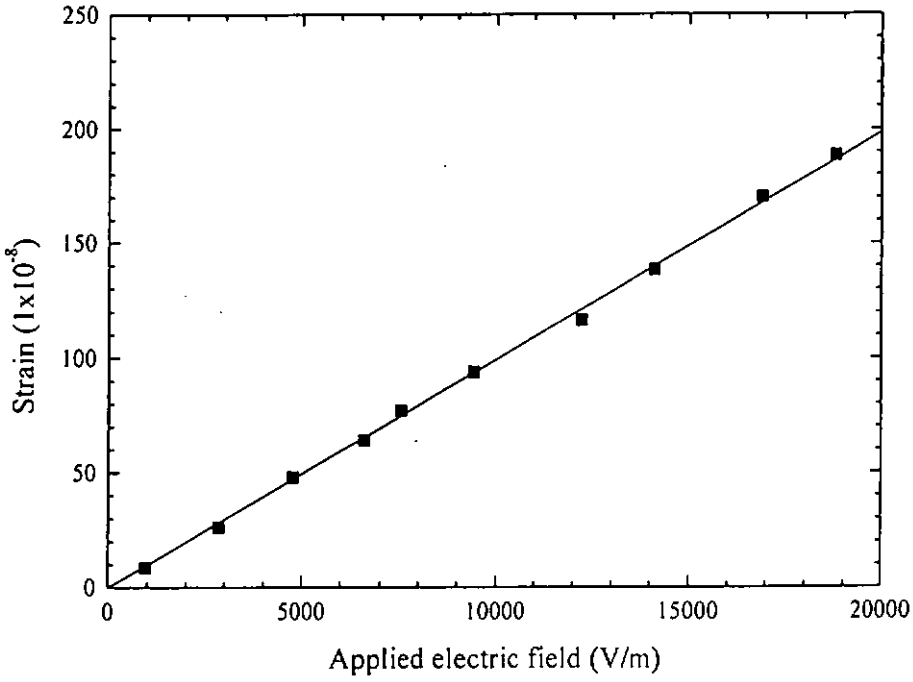

Fig. 5.4a Strain against electric field of a PZT bar measured at 1 kHz (slope of the line = d_{31} coefficient).

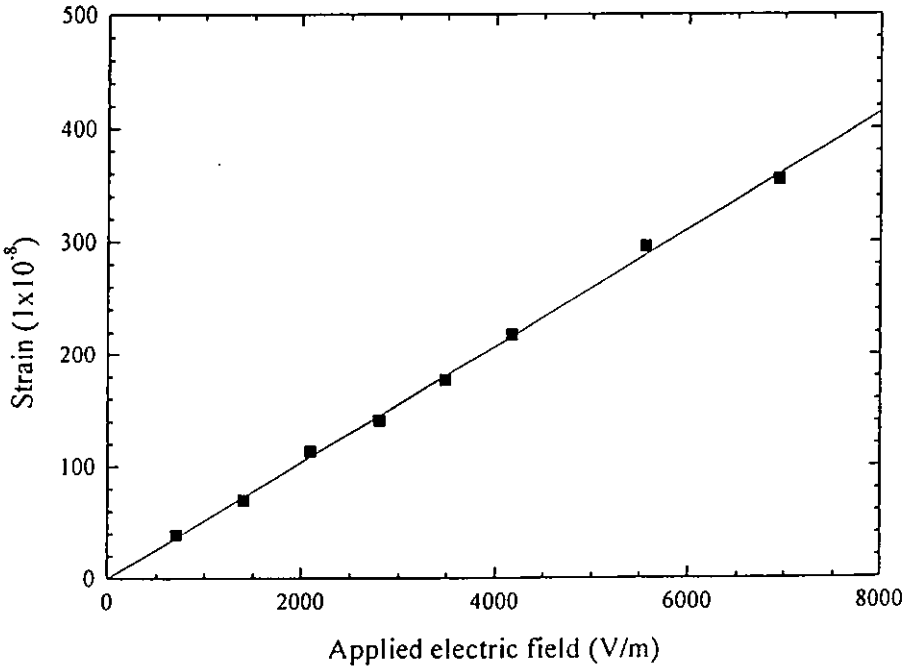

Fig. 5.4b Strain against electric field of a PMN-PT bar measured at 1 kHz (slope of the line = d_{31} coefficient).

5.4 Measurement of hydrostatic charge coefficient

The hydrostatic charge coefficients d_h is defined as the ratio of the electrical displacement (=charge/area) in the sample when it is subjected to a hydrostatic pressure. d_h was measured in a hydrostatic chamber shown in Fig. 5.5, based on a design by [Tancrell et al, 1985]. The chamber was made by polymethylmethacrylate (PMMA). Acoustic pressure was generated by two loadspeakers mounted on opposite sides of the chamber. A copper gauze was used to shield the sample located in the middle of the two loadspeakers in order to eliminate electromagnetic coupling of the signal from the speakers. The loadspeakers were driven by a function generator under an operation frequency of 80 Hz.

The value of d_h was determined by measuring the pressure applied to the sample and the charge generated on the two electroded faces. The pressure inside the chamber was measured by a calibrated microphone (Bruel & Kjaer, type 4144). The plot of acoustic pressure against the driving voltage applied for the calibration of d_h measurement is shown in Fig. 5.6.

The hydrostatic charge coefficients d_h can be calculated by:

$$d_h = \frac{C \cdot V}{P \cdot A} \tag{5.12}$$

where V is output voltage from the sample measured by the lock-in amplifier (Standford Research Systems, SR510). A is the electroded area of the sample. P is

the acoustic pressure which can be obtained from the calibration curve when the applied voltage is known. C is total capacitance at 80 Hz which can be expressed as:

$$C = C_A + C_W + C_S \tag{5.13}$$

where C_A is the capacitance of the lock-in amplifier with the value of 25 pF. C_W is the capacitance of the 1 m cable with the value of 50 pF. C_S is capacitance of the sample measured by the impedance analyzer. (C_s of PMN-PT at 80 Hz = 8.19 nF, C_s of PZT at 80 Hz =784.06 pF).

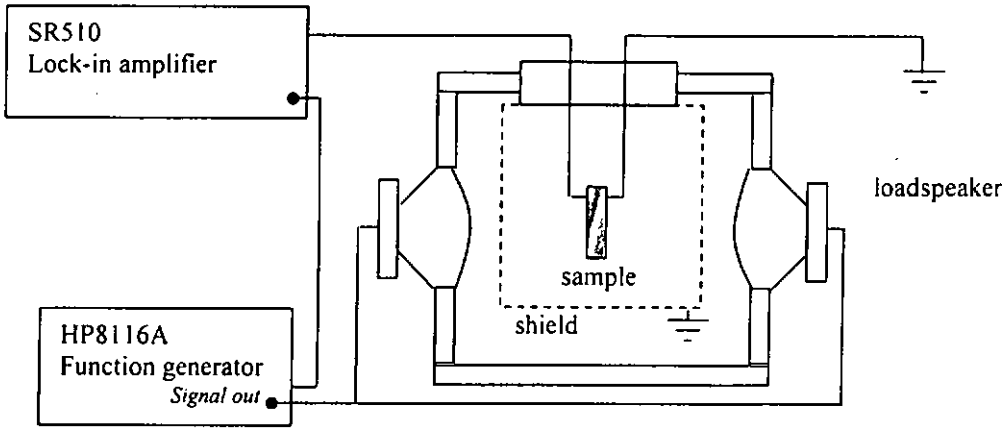

Fig. 5.5 Experimental setup for measuring the hydrostatic charge coefficient d_h.

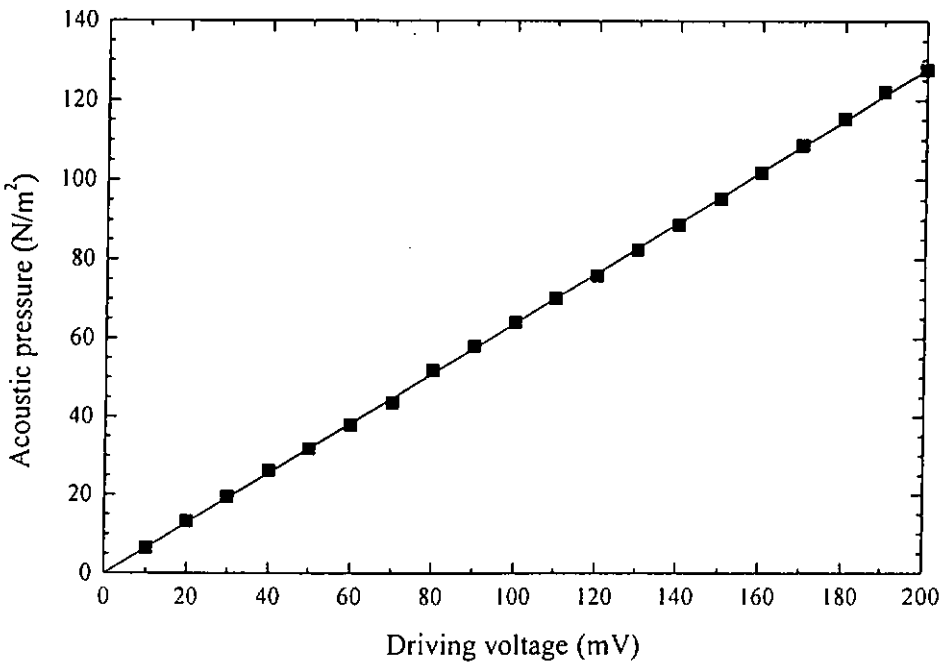

Fig. 5.6 Calibration curve of the hydrostatic chamber.

5.5 Experimental results of d_h measurements

With the applied acoustic pressure, hydrostatic charge coefficient d_h of the PMN-PT single crystal and the PZT ceramic can be measured. It can also be calculated by [Cui, 1998].

$$d_h = d_{33} + 2d_{31} \tag{5.14}$$

In Table 5.3, it can be seen that the calculated values agree well with the measured values. In Fig. 5.7, d_h of samples are quite constant at different acoustic pressures.

Table 5.3 Hydrostatic charge coefficients of the PMN-PT single crystal and the PZT ceramic.

	PMN-PT single crystal		PZT ceramic	
hydrostatic charge coefficient (10^{-12}C/N)	*measured*	*calculated*	*measured*	*calculated*
d_h	80	93	40	38

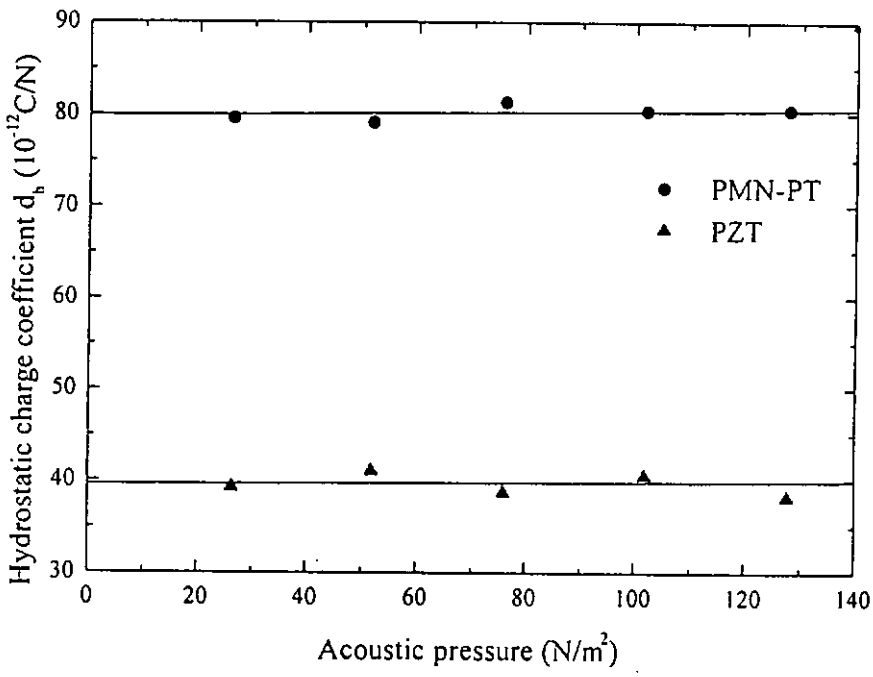

Fig. 5.7 Hydrostatic charge coefficient d_h against acoustic pressure.

CHAPTER 6

CHARACTERIZATION OF A 1-3 PMN-PT/EPOXY COMPOSITE

6.1 Introduction

A variety of piezoelectric composite materials can be made by combining a piezoelectric material with a polymer phase. Among them, the piezoelectric 1-3 composite (Fig. 1.2) that consists of piezoelectric ceramic rods embedded in a polymer phase, has attracted a great deal of attention and has been widely used in the field of underwater sonar application, actuators and medical ultrasonic imaging [Newnham, 1978; Smith, 1991]. The 1-3 composite has higher electromechanical coupling and lower acoustic impedance than conventional piezoceramic such as PZT, thus enhancing their performance because energy can couple better to water or to human tissue.

Using PMN-PT single crystal instead of conventional PZT ceramic to form a 1-3 composite with an epoxy is an original research. The PMN-PT single crystal has extra high electromechanical coupling coefficient k_{33} and by fabricating PMN-PT single crystal into 1-3 composite can make good use of its high k_{33} value.

In this chapter, by using a thinning test, electromechanical properties and resonance vibration modes of the 1-3 PMN-PT/epoxy composite with 0.49 volume fraction of PMN-PT single crystal (Fig. 6.1) were studied as a function of aspect ratio (thickness to periodicity). The material properties of the composite can thus be understood which will help to meet different requirements of specific applications. The study of the material properties of the composite with different PMN-PT volume fractions has not been possible in this project because quantity of good PMN-PT single crystals of such a large size (10 mm diameter, 3 mm thickness) provided to us was limited. The study of 1-3 PMN-PT/epoxy composites would be extended in future work.

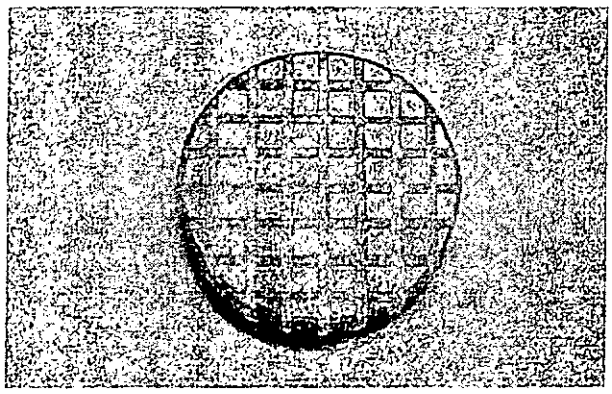

Fig. 6.1 Photograph of a 1-3 PMN-PT/epoxy composite.

6.2 Resonance modes in a 1-3 PMN-PT/epoxy composite

In a disc of 1-3 PMN-PT /epoxy composite, there are three principal types of resonance [Gururaja, 1985; Chan ,1994]: the planar mode, thickness mode, and various lateral modes arising from the regular periodicity of the PMN-PT rod in the composite. These resonance modes were studied from the electrical impedance measurement as a function of frequency. Knowledge of the resonant vibration behavior of the composite is very important in the evaluation of its use in ultrasonic transducer application.

6.2.1 Planar-mode resonance

The planar mode (also called radial) vibration in a thin disc, as illustrated in Fig. 6.2, involves mechanical vibration of the whole specimen in the x_1-x_2 plane when driven by an electric field in the x_3 direction (poling direction). Since the diameter is the largest dimension so that the radial mode is located at the lowest resonant frequency.

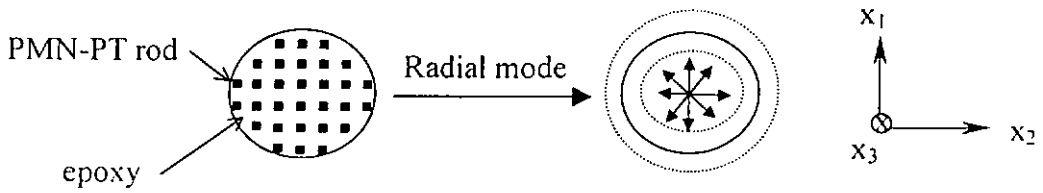

Fig. 6.2 Radial mode in a 1-3 PMN-PT/epoxy composite.

6.2.2 Thickness-mode resonance

For pulse-echo type transducer applications, study of the thickness-mode resonance of the composite shown in Fig. 6.3 is extremely important as the thickness-mode resonance is utilized for transmitting and receiving longitudinal ultrasonic waves. In this mode PMN-PT rods vibrate in the fundamental length longitudinal 33 mode along the x_3 direction (Fig. 6.4). As the PMN-PT rods embedded in polymer matrix is considered to be an integral part of the composite, this resonance of the composite corresponding to the 33 mode of the PMN-PT rods would be the thickness-mode resonance of the disc.

The thickness mode resonance frequency f_t can be determined by

$$\upsilon = f_t \lambda = 2 f_t t \tag{6.1}$$

where υ is the acoustic velocity of PMN-PT single crystal, t is the thickness of the composite.

Thickness t would be equal to half of the wavelength at the fundamental thickness resonance [Auld, 1986]. The thickness mode coupling coefficient k_t, mechanical quality factor Q_M, and the frequency constant N_t were evaluated by the following equations [IRE , 1961]

$$k_t^2 = \frac{\pi}{2} \cdot \frac{f_r}{f_a} \tan(\frac{\pi}{2} \cdot \frac{\Delta f}{f_a}) \tag{6.2}$$

$$Q_M = 4\pi \ \Delta f \ Z_m (C_0 + C_1) \tag{6.3}$$

$$N_t = f_r \cdot t \tag{6.4}$$

where t is the thickness, Z_m is the electrical impedance at the thickness resonant frequency f_r, f_r is the resonant frequency, f_a is anti-resonant frequency, $\Delta f = f_a - f_r$. Referring to the equivalent circuit in Fig. 3.5, C_1 and C_0 are the series and parallel capacitance, respectively.

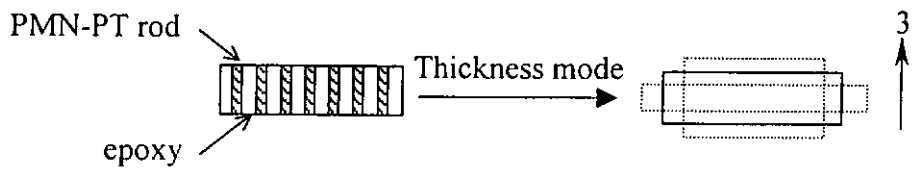

Fig. 6.3 Thickness mode in a 1-3 PMN-PT/epoxy composite.

6.2.3 Lateral-mode resonances

Lateral mode resonances are independent of the thickness of the composite but are related to the lateral dimensions of the PMN-PT rods in the composite. There are two lateral modes vibrations in the x_1 and x_2 directions of the rods. If there are no mode coupling, the two lateral modes would have the same frequency f_L because of symmetry. However, due to the existence of mode coupling between the two lateral modes and the thickness mode, f_L is thus split into two lateral modes f_{L1} and f_{L2}.

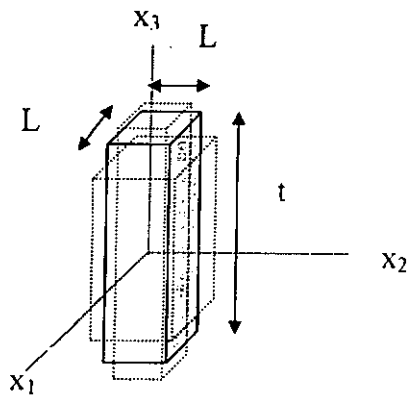

Fig. 6.4 Schematic diagram of a pillar-shaped PMN-PT element inside a 1-3 PMN-PT/epoxy composite.

6.2.4 Stopband resonances

In the 1-3 composite, when the PMN-PT rods vibrate at their thickness mode resonances, they generate shear wave in the polymer propagating in the x_1-x_2 plane (Fig. 6.5). The shear wave interacts with neighbouring rods, depending on the wavelength across the polymer matrix and the lateral periodicity d.

The existence of stopbands is related to Bragg-scattering from the neighbouring elements in the periodic lattice (Fig. 6.5). Suppose a shear wave with polarization along x_3 direction and propagating in the x_1 direction, at a frequency where the periodicity d is one-half the shear wavelength, constructive reflection (Bragg scattering) occurs. But this anti-symmetric mode can't be excited electrically as the sample is uniformly electroded and at this resonance, the alternate planes of rods oscillate at 180° out of phase.

When the periodicity $d = \lambda$, standing wave patterns result as illustrated in Fig. 6.5. In the first stopband, a x_1-propagating wave with x_3 polarization is again Bragg-scattered with a phase shift of 2π from one plane of rods to an adjacent plane. The x_1-propagating wave is also Bragg-scattered by the 45° planes of rods (Fig. 6.5) when periodicity d is equal to $\sqrt{2}\lambda$. Here the rods vibrate in phase and correspond to the second stopband of the square lattice and the resonance can be excited electrically.

Standing wave resonances occur at frequency f_s and f_{s1} which were given by

$$f_s = \upsilon_s / d \tag{6.5}$$

$$\lambda_s = \sqrt{2} \cdot \lambda_{s1} \tag{6.6}$$

$$f_{s'} = \sqrt{2} \cdot f_s \tag{6.7}$$

where υ_s is the shear wave velocity of the polymer, f_s and f_{s1} are stopband resonant frequencies.

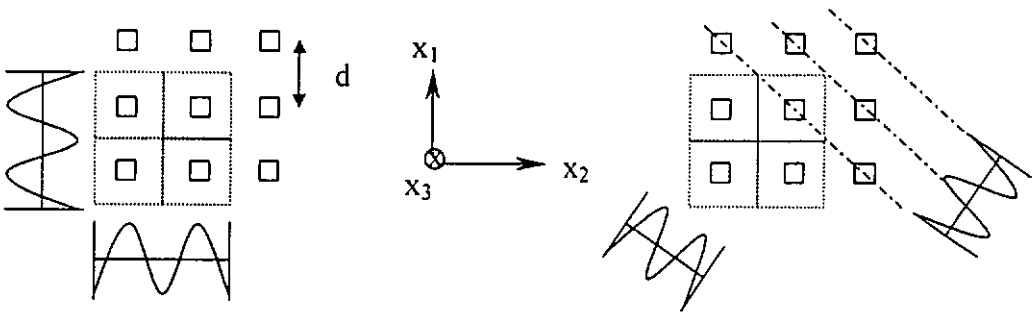

Fig. 6.5 Standing wave patterns inside a unit cell of the 2-D lattice.

6.3 Comparison of the electrical properties of a PMN-PT disc and a 1-3 PMN-PT/epoxy composite disc

In this section, resonance modes of a PMN-PT single crystal disc and a 1-3 PMN-PT/epoxy composite disc (Fig. 6.8) with the diameter of 10.00 mm and the thickness of 2.93 mm have been studied. They were poled in the (001) direction and the electrical impedance and phase of these samples as a function of frequency were compared. The electrical impedance spectra were measured and recorded by an HP 4194A impedance/gain phase analyzer.

From the impedance spectra (Fig. 6.6) of the PMN-PT disc, there exists two groups of strong resonances, namely thickness mode f_t and radial mode f_p with its harmonics. The radial mode resonance (76 kHz) appears at the lowest frequency due to the largest lateral dimension of the disc. Many harmonic resonances exist from 80 kHz to 400 kHz. This complicated radial mode harmonics pattern makes it impossible to find k_p, N_p and σ using the IEEE standard. However, the strong fundamental thickness resonance of 658.8 kHz is very pure indicating that there is no mode coupling near the resonance. Small fluctuation following the thickness resonance implies that there is some micro-defect in the single crystal which may be caused by the inhomogeneity of the crystal.

In the impedance spectrum of the 1-3 PMN-PT/epoxy composite (Fig. 6.7), with 0.49 volume fraction PMN-PT, the planar resonance mode at 100 kHz is weaker than that

of the single crystal. The weak second and third harmonics can be seen at a frequency of 243.8 kHz and 363.2 kHz which is approximately twice and triple that of the fundamental mode. This is because the lateral vibrations in the x_1 and x_2 plane is greatly damped in the polymer matrix, thus resulting in much weaker radial resonances. In order to understand how resonance characteristics of the 1-3 composite as a function of aspect ratio of the rod elements, a thinning test has been carried out as described in the next section.

In the electrical impedance spectrum of the 1-3 PMN-PT composite (Fig. 6.7), the strong thickness resonance greatly shifted to lower frequency compared to that of the PMN-PT disc and slightly coupled with the planar resonance. By comparing their measured material properties (Table 6.1), it is noted that the mechanical quality factor Q_M of the 1-3 composite has been greatly reduced (from $Q_M = 82$ to $Q_M = 12$) indicating that vibration of the PMN-PT rods has been damped by the surrounding polymer. The 1-3 composite with low Q_M factor appeared well suited for broad bandwidth transducer applications. Furthermore, the electromechanical coupling factor k_t has been enhanced (increased from 0.59 to 0.76). The piezoelectric coefficient d_{33} of the 1-3 composite measured by a d_{33} meter (ZJ-3B from the Institute of Acoustics Academia Sinica) is slightly reduced. On the other hand, small stopband resonance mode can be found in the impedance spectrum (Fig. 6.7). Location of the stopband depend on the periodicity d of the composite (Fig. 6.8). The stopband resonance can be approximately estimated using the shear wave velocity υ_s of the polymer at least for the sample with a large polymer volume fraction. With υ_s of 1416 m/s determined in Chapter 4, one stopband resonant frequency was

calculated to be at 1.05 MHz which is closed to the measured value shown in Table 6.2.

Lateral mode of the rod f_L can be seen in the impedance spectra shown in Appendix B. In the thinning test, the lateral mode can be identified easily as it depends on the size of the rod elements and is nearby independent of the 1-3 composite thickness if mode coupling does not exist. In the plot marked thickness of 2.93 mm in Appendix B, there is no mode coupling between the lateral mode resonance and the fundamental thickness resonance as the rod has a small aspect ratio (width to thickness L/t). This would be discussed in detail in the next section.

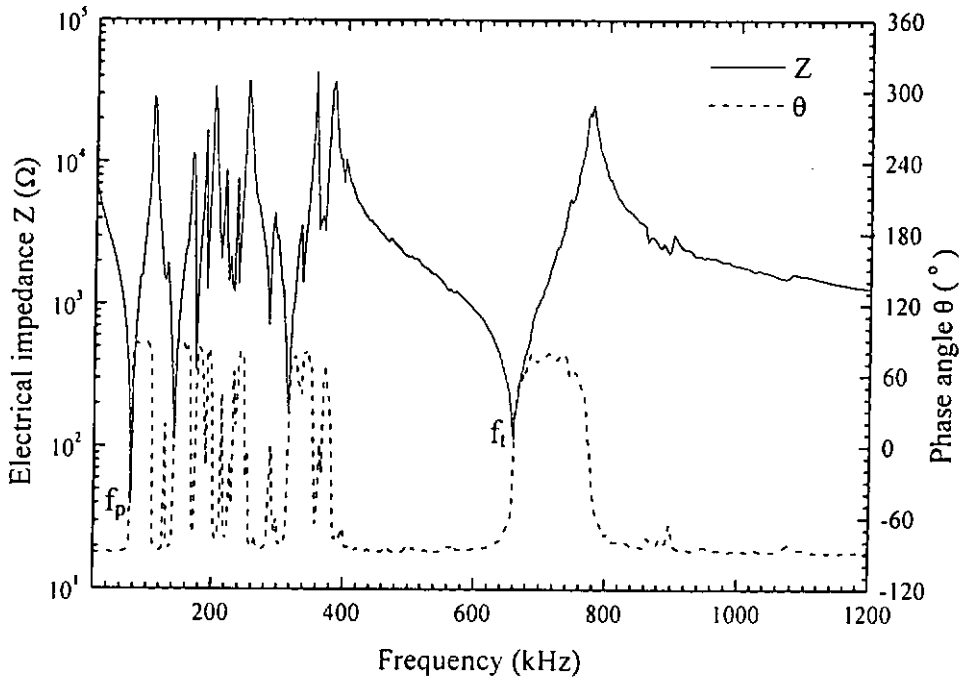

Fig. 6.6 Electrical impedance Z and phase θ against frequency for a PMN-PT disc. (Thickness = 2.93 mm)

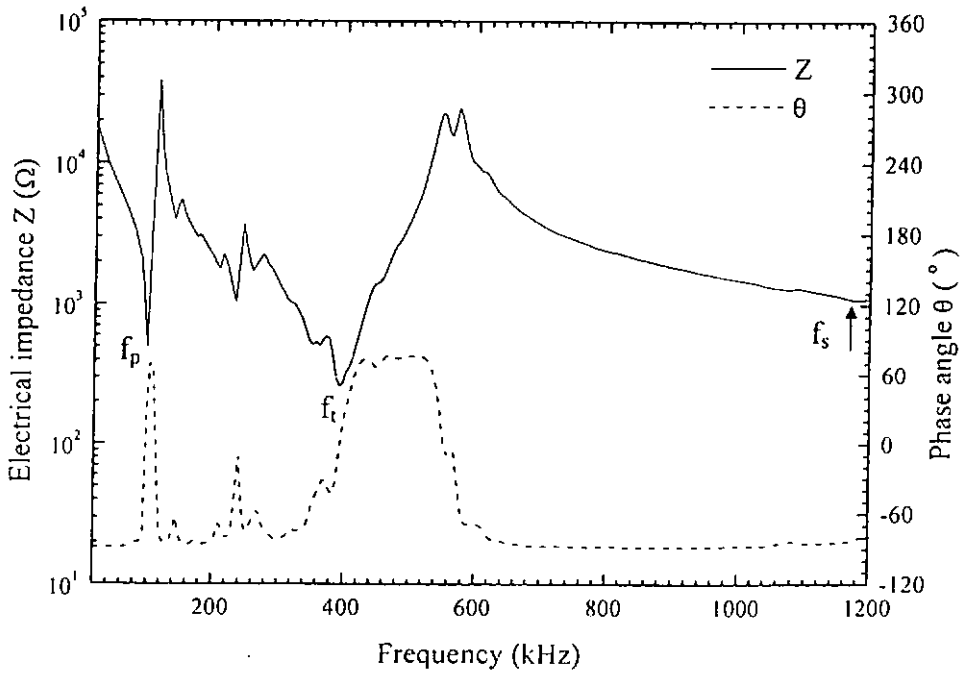

Fig. 6.7 Electrical impedance Z and phase θ against frequency for a 1-3 PMN-PT/epoxy composite disc. (Thickness = 2.93 mm)

Table 6.1 Material properties of PMN-PT and 1-3 PMN-PT/epoxy composite discs.

Material properties	*PMN-PT disc*	*1-3 PMN-PT/epoxy composite disc*
$\varepsilon_{33}/\varepsilon_0$ at 1kHz	3321	2267
tanδ at 1kHz	0.003	0.023
ρ (kg/m^3)	7924	4508
k_t	0.59	0.76
Q_M	82	12
N_{3t} (Hz-m)	1930	1152
d_{33} (10^{-12}pC/N)	1232	1079

Table 6.2 Measured resonant frequencies of PMN-PT and 1-3 PMN-PT/epoxy composite discs with thicknesses of 2.93 mm.

Resonant frequencies (kHz)	*PMN-PT disc*	*1-3 PMN-PT/epoxy composite disc*
Planar mode, f_p	75.94	99.55
Thickness mode, f_t	658.80	393.08
Stopband mode, f_s	---	1199.23
Lateral mode, f_L	---	1392.56

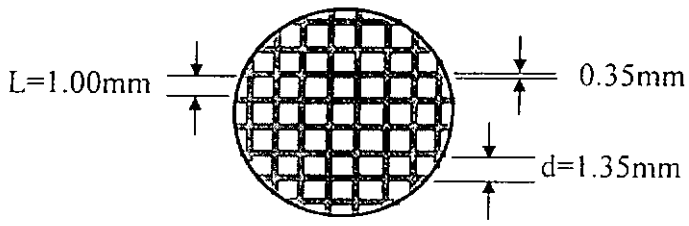

Fig. 6.8 Schematic diagram of a 1-3 PMN-PT/epoxy composite (ϕ = 0.49) with dimensions.

6.4 Thinning test results in the 1-3 composite

From the results of the thinning test (Appendix B), changes in frequencies of the electrical resonance peaks were monitored while the thickness of the 1-3 composite was reduced. The material properties N_{3t}, Q_M, k_t, υ^D of the 1-3 composite were also studied as functions of the change in its thickness. With the knowledge of the material properties, desirable thickness of the 1-3 composite can be chosen to meet the specific device requirements.

During the thinning test, four different resonance modes are identified and characterized as follows:

Thickness mode resonance f_t

The thickness mode resonance f_t is the strongest resonance when the sample is thick because it is directly coupled to the applied electric field. From the plot of f_t vs L/t in Fig. 6.9, the thickness mode resonant frequency is found to increase linearly with decreasing thickness. When the width L of the rod elements become comparable to the thickness t, the thickness and lateral modes couple together.

Planar mode resonance f_p

In Fig. 6.10, the planar mode resonance located at the lowest frequency increased slightly with decreasing thickness. Several weak resonances following the planar

mode are the planar mode harmonics, which have frequencies approximately equal to an integral multiple of f_p.

Lateral mode resonance f_L

The lateral resonance f_L (Appendix B) is rather weak compared to the thickness mode resonance because the rod elements embedded in the polymer matrix are clamped. From Fig. 6.11, the lateral resonant frequency increases linearly with the decrease in thickness and f_L can hardly be observed when the aspect ratio is greater than 0.7, because of the mode coupling between the thickness and the lateral mode.

Stopband resonance f_s

Stopband resonance is too weak to be observed even if there is no mode coupling. This implied that the stopband cause little influence to the thickness mode. From Fig. 6.12, stopband resonance is independent of the change in thickness when the aspect ratio is <0.6. Data points are not shown when the aspect ratio >0.6 because the stopband is too small to be identified.

On the other hand, the electromechanical coupling factor k_t increases rapidly with the decrease in thickness until the aspect ratio approaches to 0.7 (Fig. 6.13). The mechanical quality factor Q_M (Fig. 6.14) of the 1-3 composite is reduced when the aspect ratio is >0.5. This implies that strong mode coupling occurs when the thickness is approaching the lateral width. Frequency constant N_{3t} and longitudinal wave velocity shown in Figs. 6.15 and 6.16 decrease with decreasing thickness.

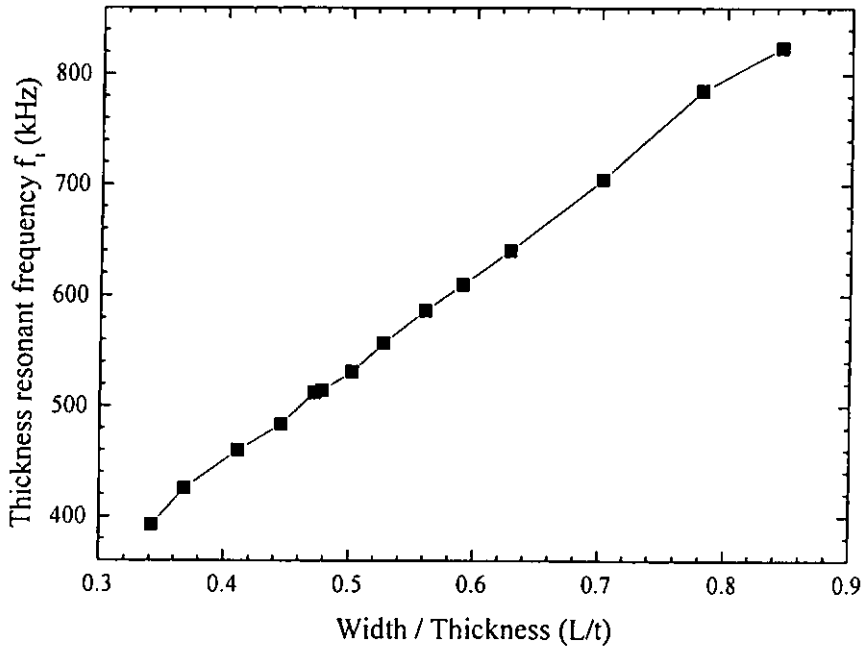

Fig. 6.9 Thickness resonant frequency f_t of a 1-3 PMN-PT/epoxy composite against width/thickness.

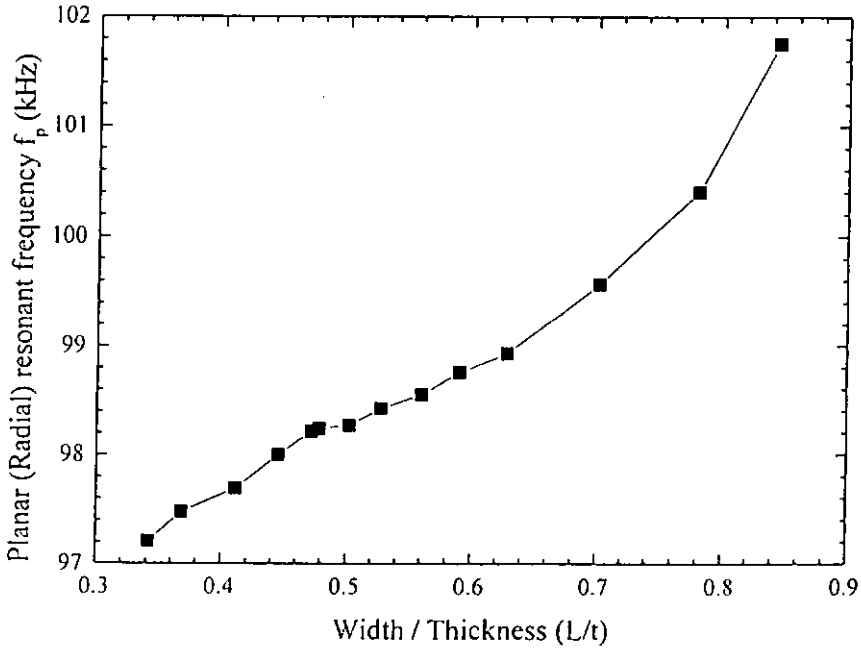

Fig. 6.10 Planar resonant frequency f_p of a 1-3 PMN-PT/epoxy composite against width/thickness.

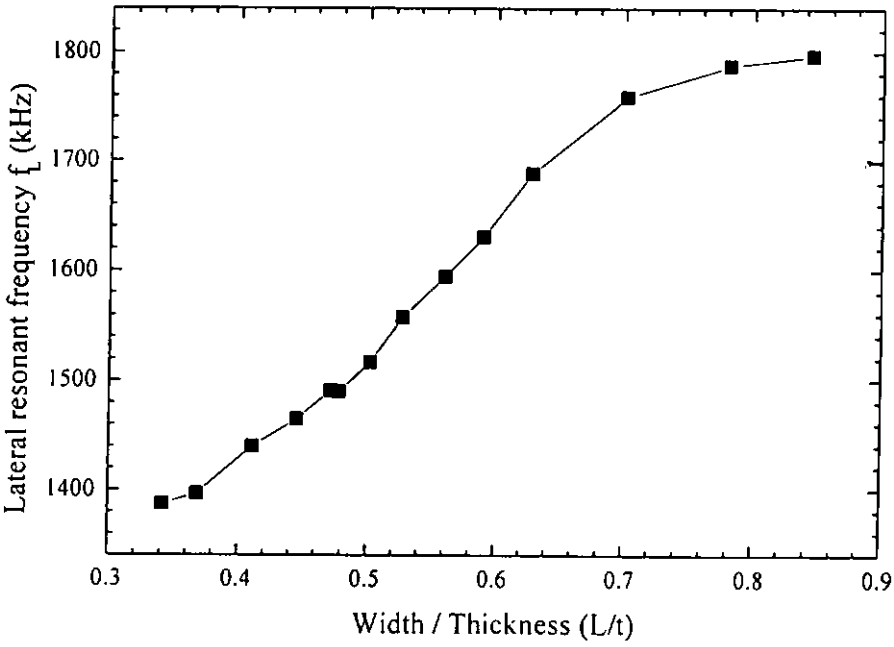

Fig. 6.11 Lateral resonant frequency f_L of a 1-3 PMN-PT/epoxy composite against width/thickness.

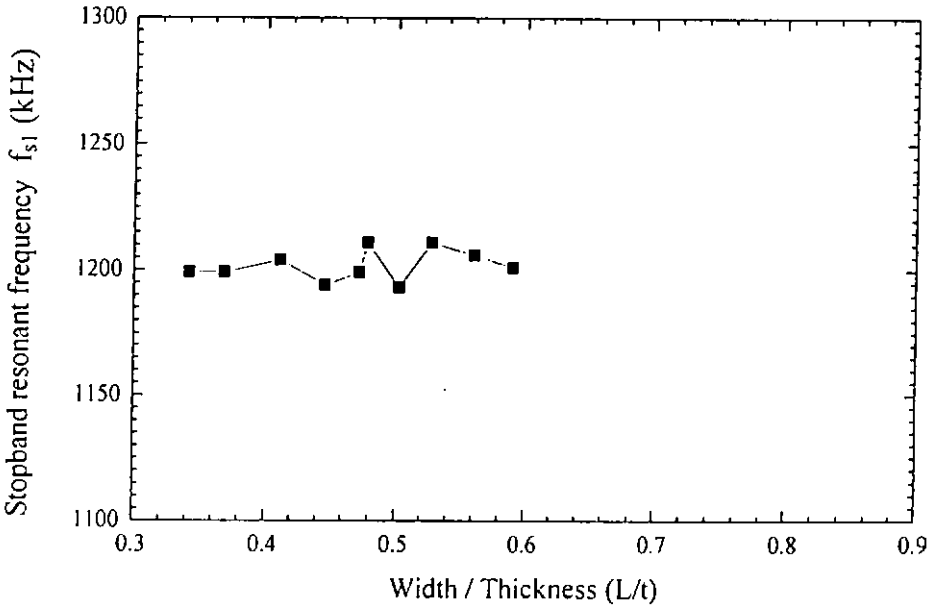

Fig. 6.12 Stopband resonant frequency f_s of a 1-3 PMN-PT/epoxy composite against width/thickness.

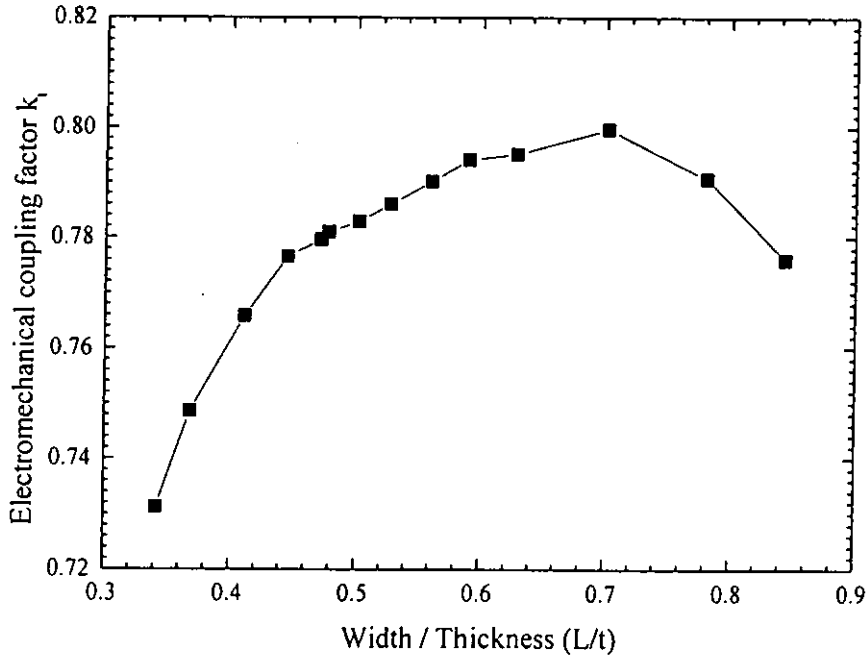

Fig. 6.13 Electromechanical coupling factor k_t of a 1-3 PMN-PT/epoxy composite against width/thickness.

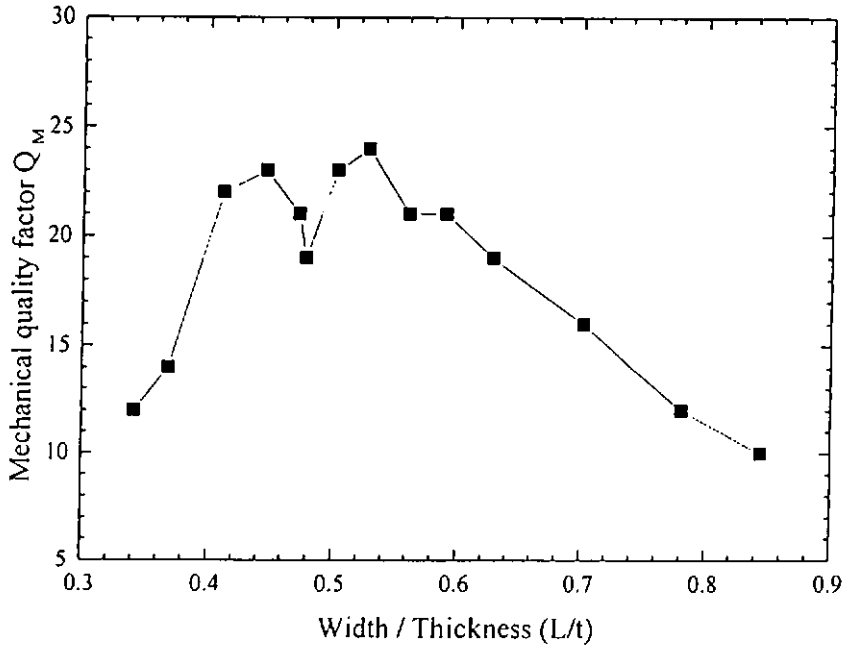

Fig. 6.14 Mechanical quality factor Q_M of a 1-3 PMN-PT/epoxy composite against width/thickness.

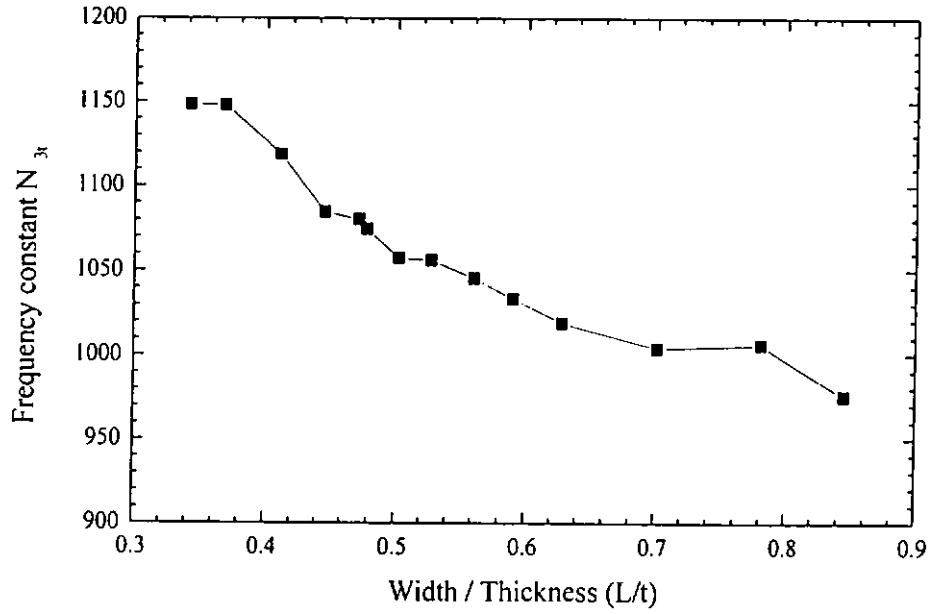

Fig. 6.15 Frequency constant N_{3t} of a 1-3 PMN-PT/epoxy composite against width/thickness.

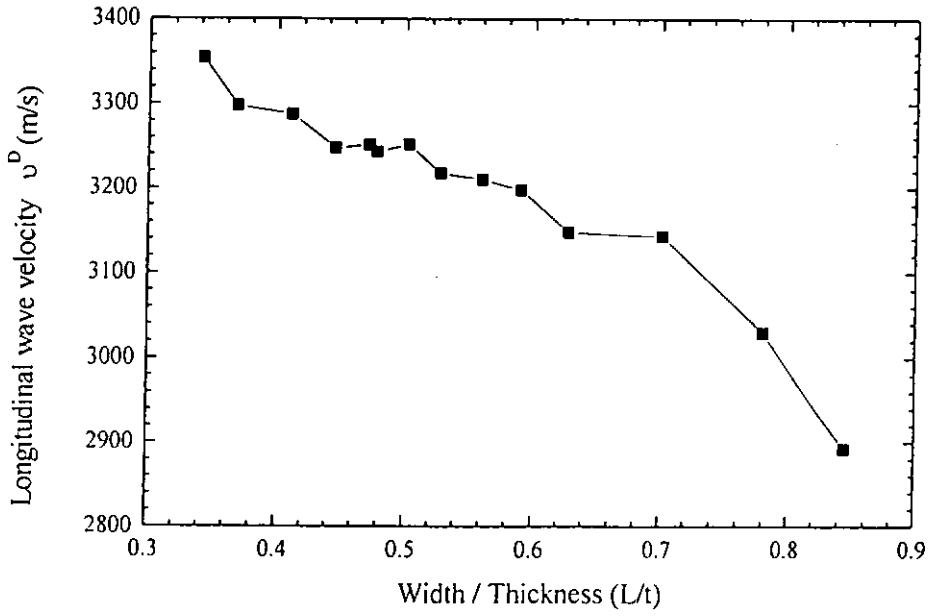

Fig. 6.16 Longitudinal wave velocity υ^D of a 1-3 PMN-PT/epoxy composite against width/thickness.

CHAPTER 7

CHARACTERIZATION OF PZT/EPOXY COMPOSITE SANDWICH TRANSDUCERS

7.1 Introduction

Ring-shaped PZT/epoxy composites were produced for fabricating Langevin sandwich-type transducers to be used as the driver (Fig. 7.1) of an ultrasonic wire bonding transducer. The study of using composite rings instead of conventional PZT ceramics for fabricating the driver in the wire bonding application is a promising research that no related literature has been reported. On the other hand, The reliability of the operation performance of the piezoelectric material used is a major concern for all high power ultrasonic applications. Since conventional piezoelectric PZT material has high mechanical Q_M factor, locking the operating frequency in a designated range becomes increasingly difficult as the frequency goes up. Mode coupling is another problem. Strong radial and wall thickness resonance modes and their harmonics in the piezoelectric ring would easily couple with the operation mode, thereby causing difficulty in the performance control. However, using the composites instead of piezoelectric PZT ceramic can alleviate the problem since the composites have lower mechanical Q_M factor with wider bandwidth and lower planar mode-coupling coefficients which can minimize the occurrence of mode couplings.

In this chapter, the PZT 802 rings fabricated as described in Chapter 2 are used. Mode coupling in the PZT rings which is closely related to its geometry and dimensions is studied and the electromechanical properties of the rings are measured as a function of thickness. By a thinning test of the piezoelectric PZT ring, shifts in resonance vibrations were noted. Thickness of the rings was also optimized regarding the electromechanical properties of the piezoelectric ring.

The electrical characteristics of PZT/epoxy composite rings with different cutting patterns have been measured and compared with that of the PZT ring. The relative amplitude of various resonance vibrations, mechanical Q_M factor and electromechanical coupling factor of these composite rings have been evaluated. From the result, a desirable pattern can be chosen for the wire bonding transducer fabrication. For each set of cutting pattern, four composite rings were used in fabricating a composite driver and their electrical characteristics were measured and compared with the PZT driver.

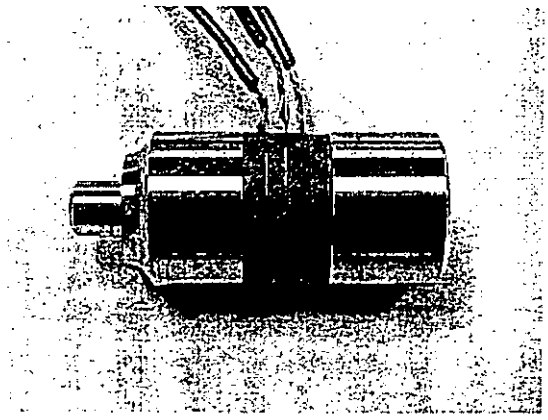

Fig. 7.1 Photograph of a Langevin sandwich-type driver.

7.2 Resonance modes in a PZT ring

There are three possible fundamental modes of vibrations in a piezoelectric ring when an electric field parallel to the poling direction (Fig. 7.2) was applied to the electroded face [Hueter, 1955]. (1) The thickness mode vibration occurs when the applied frequency is close to the thickness resonant frequency $f_{r\text{-}thk}$ which induces a change in thickness $\tau_r \pm \Delta\tau_r$. (2) The radial mode vibration occurs when the applied frequency is close to the radial resonant frequency $f_{r\text{-}rad}$ which induces a change in the mean diameter $d_{mr} \pm \Delta d_{mr}$. The radial mode always appears as the lowest frequency as the diameter is the largest dimension. (3) The wall thickness mode $f_{r\text{-}wall}$ occurs when the frequency is close to the resonant frequency along the wall thickness direction, causing a change in the wall thickness $w_r \pm \Delta w_r$. The resonant frequencies of each mode [IEC standard, 1976] are given by

Thickness mode
$$f_{r-thk} = \frac{1}{2\tau_r\sqrt{\rho \cdot s_{33}^D}} \tag{7.1}$$

Radial mode
$$f_{r-rad} = \frac{1}{\pi d_{mr}\sqrt{\rho \cdot s_{11}^E}} \tag{7.2}$$

Wall thickness mode
$$f_{r-wall} = \frac{1}{2w_r\sqrt{\rho \cdot s_{11}^E}} \tag{7.3}$$

where $d_{mr}=(d_{outer}+d_{inner})/2$ is the mean diameter, $w_r=(d_{outer}-d_{inner})/2$ is the mean wall thickness and τ_r is the thickness of the ring.

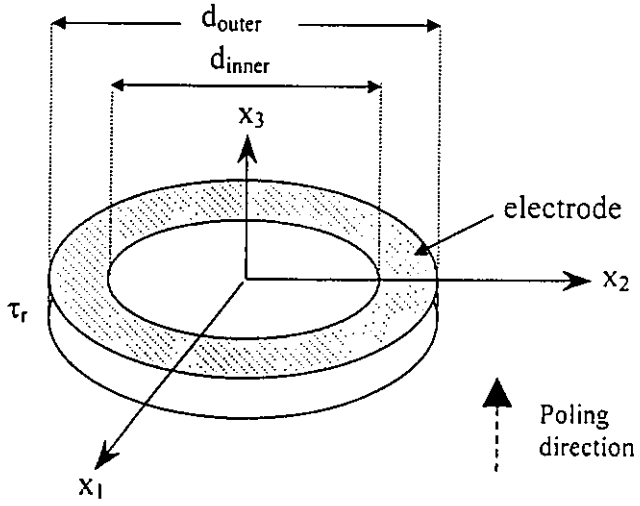

Fig. 7.2 Schematic diagram of a PZT ring.

The dimensions of the PZT ring used in studying the characteristics of the vibration modes are : thickness τ_r = 1.78 mm, outer diameter d_{outer} = 13.00 mm and inner diameter d_{inner} = 5.20 mm. Three strong resonance vibrations can be identified from the electrical impedance and phase as a function of frequency as shown in Fig. 7.3. Measured resonant frequencies of each mode can be compared with the calculated values and are shown in Table 7.1. The optimal ring thickness used in the driver fabrication has been selected from the thinning test to be discussed in the next section. The material parameters of the PZT ring having a thickness of 1.78 mm show good agreements compared with the data supplied by Morgan. Error between the measured and calculated thickness mode is relatively small. Errors in the radial and wall thickness mode is larger due to the variation in the inner and outer diameter.

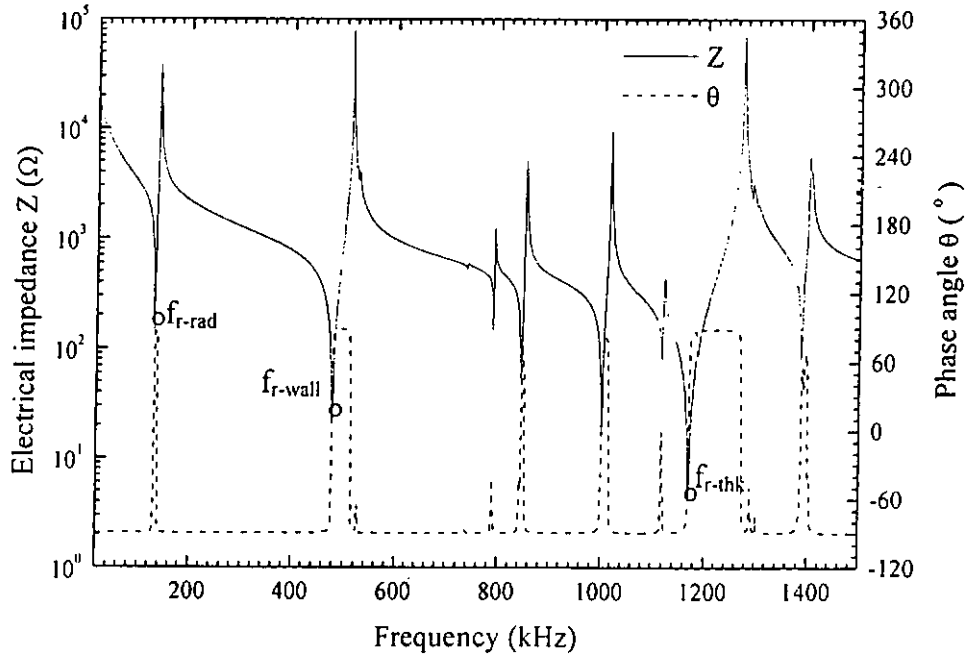

Fig. 7.3 Electrical impedance Z and phase θ against frequency of a PZT (PKI 802) ring of thickness = 1.78 mm.

Table 7.1 Measured and calculated resonant frequencies of a PZT ring.

Resonant frequency	*Measured value (kHz)*	*Calculated value (kHz)*	*Error (%)*
Radial mode, $f_{r\text{-rad}}$	130.40	121.17	-7.12
Wall thickness mode, $f_{r\text{-wall}}$	478.25	444.10	-7.14
Thickness mode, $f_{r\text{-thk}}$	1170.85	1183.90	1.11

7.3 Thinning test results of a PZT ring

By thinning a PZT ring, it is possible to find how various material parameters such as k_t, Q_M, N_{3t} and resonant frequencies of different vibration modes change with thickness. This knowledge is extremely important for optimizing the dimension required for specific ultrasonic applications.

In terms of resonance mode vibrations, strong radial, wall thickness and thickness modes of the ring are observed. From plots of electrical impedance and phase against frequency shown in Appendix C, radial resonance mode appearing at the lowest frequency is very pure without mode coupling. $f_{r\text{-}rad}$ is slightly lower in thicker ring (> 4 mm thick) as shown in Fig. 7.4a which may be due to the presence of the strong thickness mode near to the radial mode. When the outer diameter d_{mr} is larger than 2.7 times the thickness τ_r, the radial frequency is quite constant indicating that it is independent of the thickness.

Considering the wall thickness resonance given in the impedance plots shown in Appendix C. When the wall thickness w_r is larger than 2 times the thickness τ_r, the wall thickness mode is very pure without mode coupling. It is also observed from Fig. 7.4b that the wall thickness resonant frequency decreases almost linearly with the increase in thickness. When the ring thickness is nearly equal to the wall thickness, mode coupling occurs and several strong resonance are found. (Appendix C).

Thickness resonance is the strongest vibration mode in a ring poled along the thickness direction. A strong and pure thickness mode is extremely important if the thickness mode is to be used in ultrasonic applications. Fig. 7.4c shows how the thickness mode resonance varies with the thickness of the ring. Among the impedance plots shown in Appendix C, the strongest and pure thickness resonance was found at a thickness of 1.78 mm. The ring with this thickness exhibits the highest electromechanical factor k_t of 0.43 (Fig. 7.4d) and has the minimum electrical impedance of 2.7Ω at the thickness mode resonance (Fig. 7.4e). Furthermore, high mechanical quality factor Q_M of 1213 has been obtained at the thickness of 1.78 mm (Fig. 7.4f). Thickness frequency constant N_{3t} of 2084 at a thickness of 1.78 mm is shown in Fig. 7.4g which is similar to that measured in Chapter 3. Another strong and pure resonance mode at a thickness of 2.5 mm was also found but its material parameters are a little bit lower than that of the thickness of 1.78 mm. This can be another choice for the ring thickness. When the thickness is over 3 mm, the material parameters measured are getting worse presumably due to the thickness resonance mode is approaching the wall thickness resonance causing strong mode coupling.

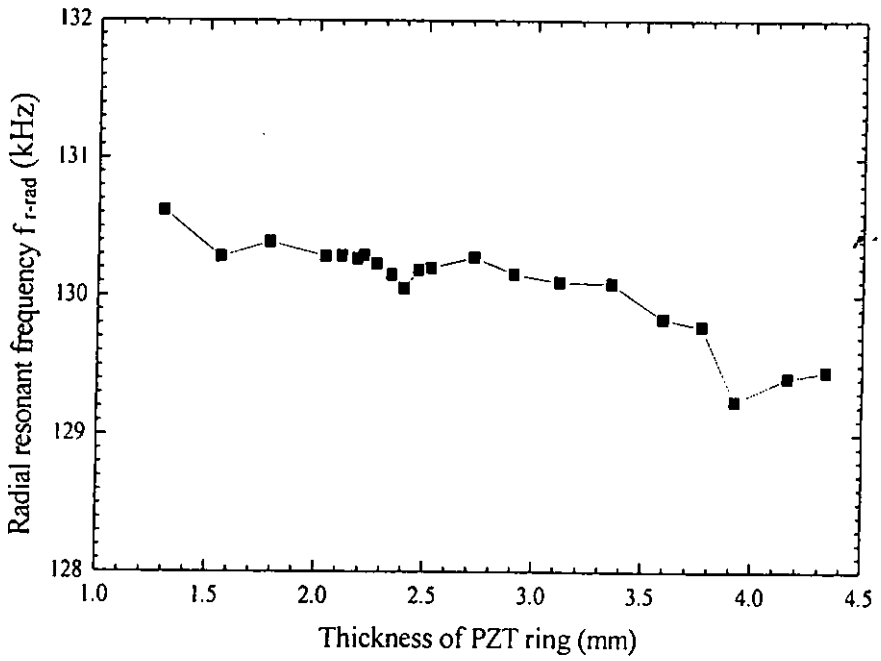

Fig. 7.4a Radial resonant frequency $f_{r\text{-}rad}$ against thickness of a PZT ring.

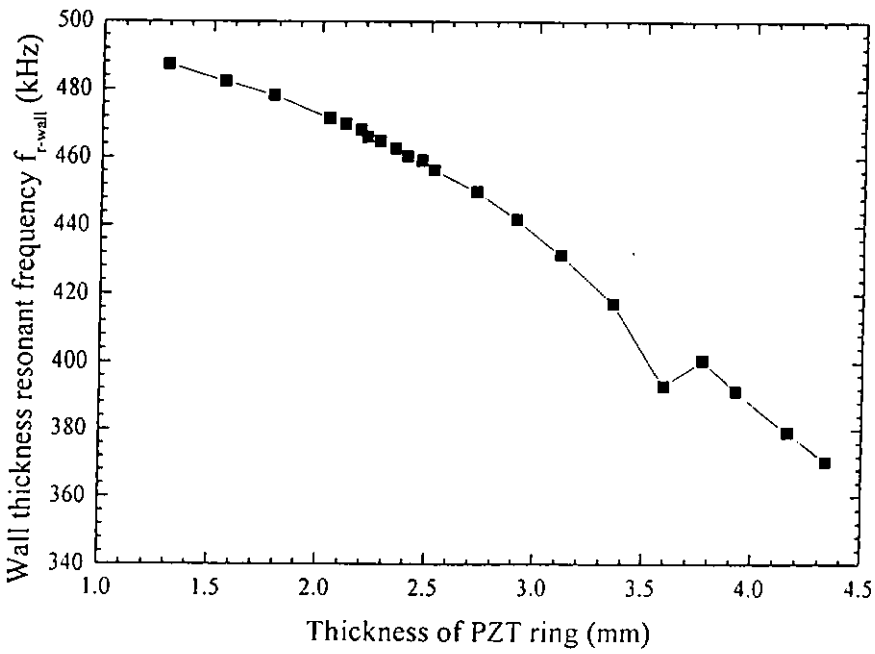

Fig. 7.4b Wall thickness resonant frequency $f_{r\text{-}wall}$ against thickness of a PZT ring.

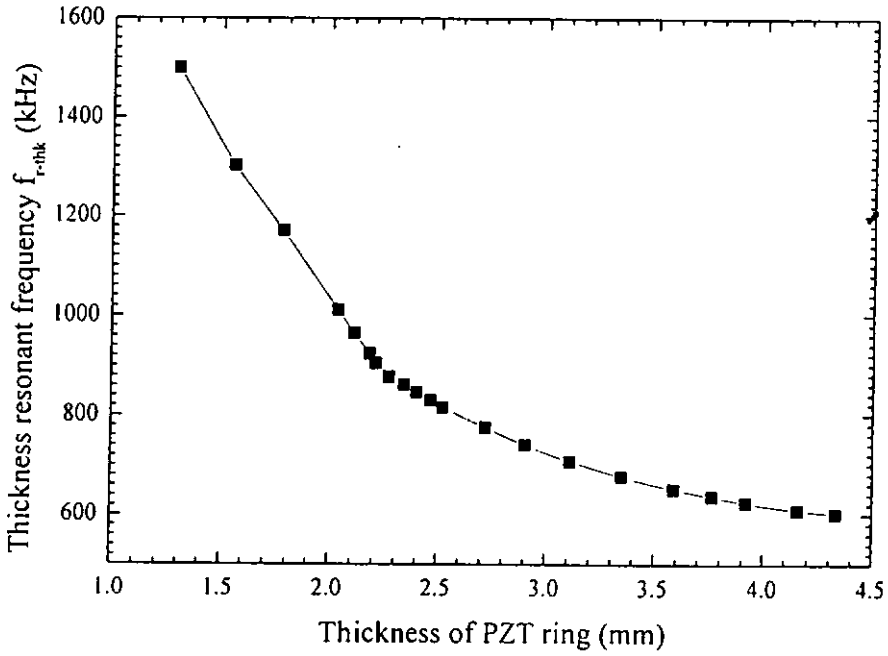

Fig. 7.4c Thickness resonant frequency $f_{r\text{-}thk}$ against thickness of a PZT ring.

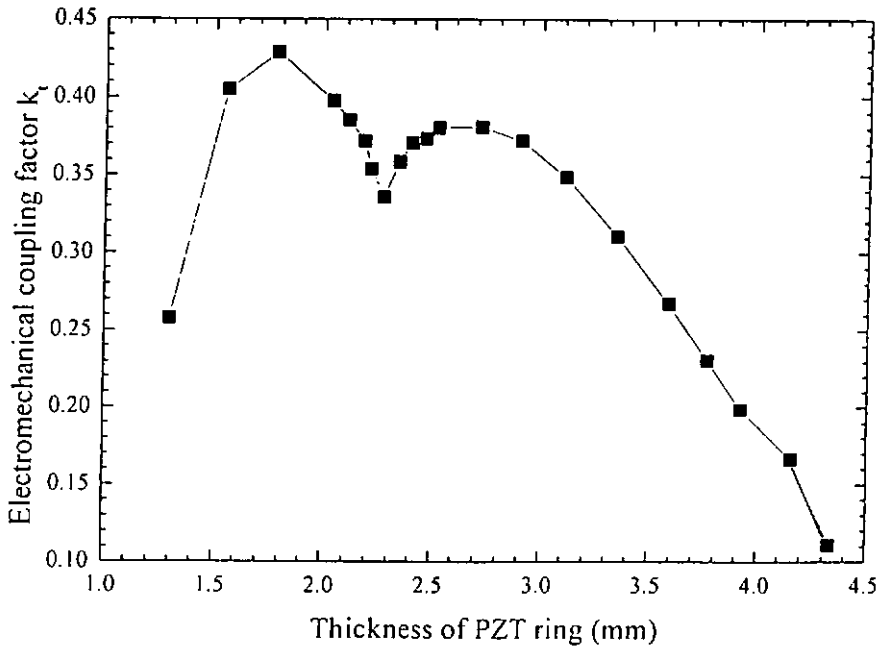

Fig. 7.4d Electromechanical coupling factor k_t against thickness of a PZT ring.

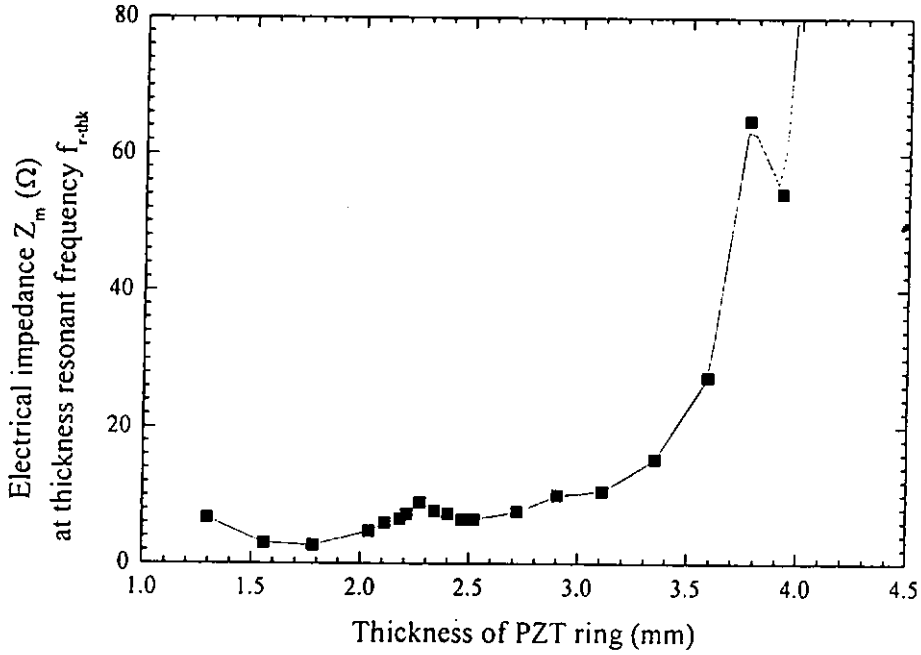

Fig. 7.4e Electrical impedance Z_m at thickness resonant frequency $f_{r\text{-}thk}$ against thickness of a PZT ring.

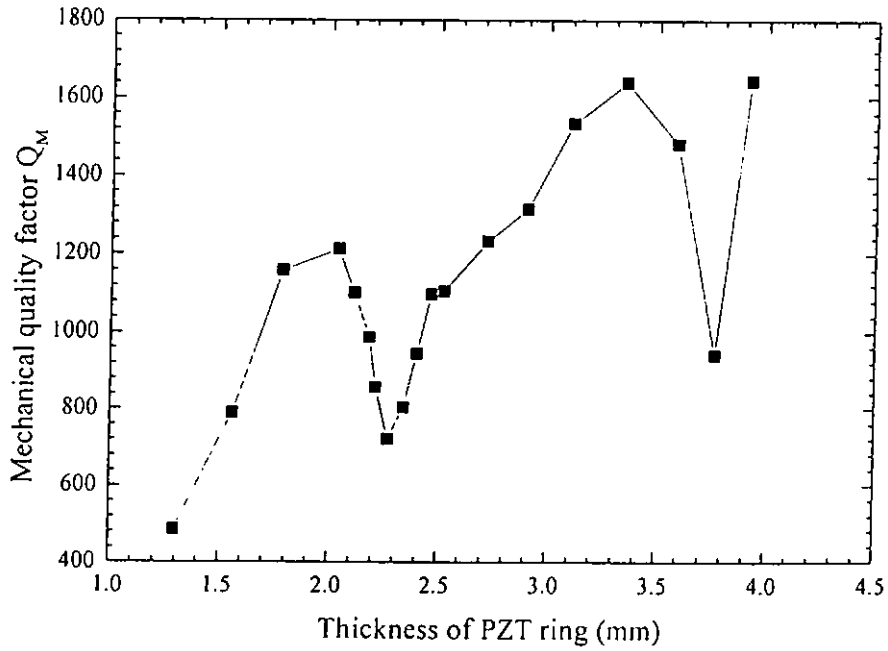

Fig. 7.4f Mechanical quality factor Q_M against thickness of a PZT ring.

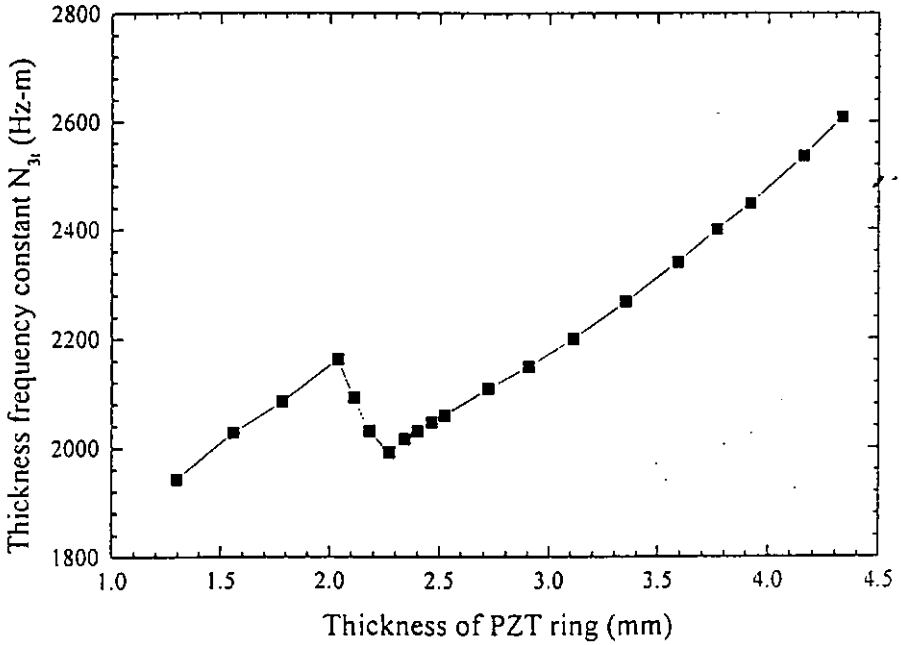

Fig. 7.4g Thickness frequency constant N_{3t} against thickness of a PZT ring.

7.4 Electrical characterization of composite rings

Piezoelectric rings with the optimised thickness of 1.78 mm were used to make composite rings with two types of cutting patterns by the dice-and-fill technique as described in Chapter 2. As shown in Fig. 7.5, one type is called the 'cake' and the other one is called the '1-3' composite rings. There are four reasons for selecting these two cutting patterns for fabricating composite drivers:

1. Ceramic volume fraction should be made as high as possible. As the polymer used makes no contribution to the piezoelectric behavior, more polymer in the composite rings will dilute the piezoelectric properties of the composite.

2. Low planar mode coupling factor should be obtained to avoid other modes being coupled to the thickness resonance.

3. The mechanical quality factor Q_M should be reduced to give a broader bandwidth. This will make it easier to lock the operating frequency in a designated range.

4. A region of operating frequencies should give pure resonances in order to avoid mode coupling.

From Fig. 7.5, only a few cuts to the piezoelectric rings are made in order to maintain a high ceramic volume fraction of 0.86 for the 1-3 composite and 0.92 for the cake composite, respectively.

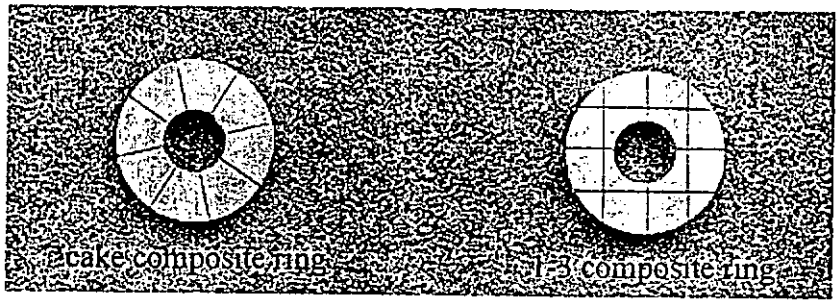

Fig. 7.5 Photograph of a cake composite ring and a 1-3 composite ring.

Comparing the impedance spectra of 1-3 and cake composite rings (Fig. 7.6 and Fig. 7.7) with that of the ceramic ring (Fig. 7.3), it can be seen that the radial mode resonance $f_{r\text{-}rad}$ in these composites has been greatly reduced and is located at a frequency about 30% lower than that of the ceramic ring. There are some radial mode harmonics in the 1-3 composite ring in the frequency ranging from 200 kHz to 400 kHz.

It is observed that the wall thickness resonance has been removed in the 1-3 composite ring. The wall thickness resonance is reduced in the cake composite and is shifts slightly to lower frequency.

The thickness resonance mode can't be identified in both composite rings. It was caused by the existence mode coupling with other resonance modes. Since the composite rings were made by coarse cutting with a diamond saw, the lateral dimensions was quite close to the thickness. The situation can be improved by using a high precision dicing saw to make finer cuts to the composite while maintaining high ceramic volume fraction.

Table 7.2 Measured resonant frequencies of a 1-3 composite ring and a cake composite ring.

Resonant frequency (kHz)	*1-3 composite*	*cake composite*	*ceramic ring*
$f_{r\text{-rad}}$	87.50	92.18	130.40
$f_{r\text{-wall}}$	---	449.85	478.25
$f_{r\text{-thk}}$	undetermined	undetermined	1170.85

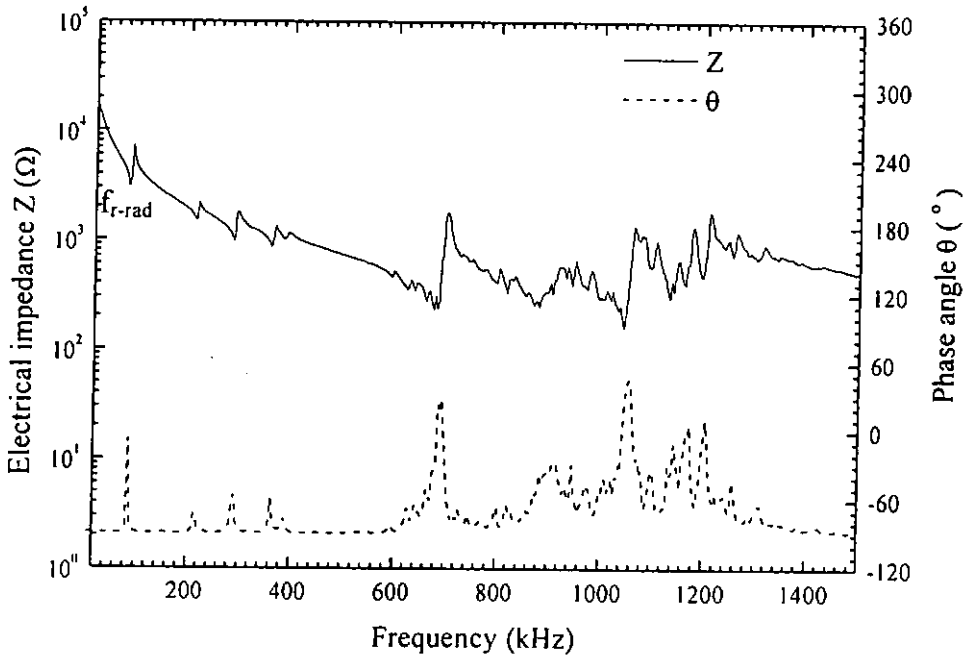

Composite ceramic volume fraction=0.86

Fig. 7.6 Electrical impedance Z and phase θ against frequency of a 1-3 composite ring of thickness = 1.78 mm.

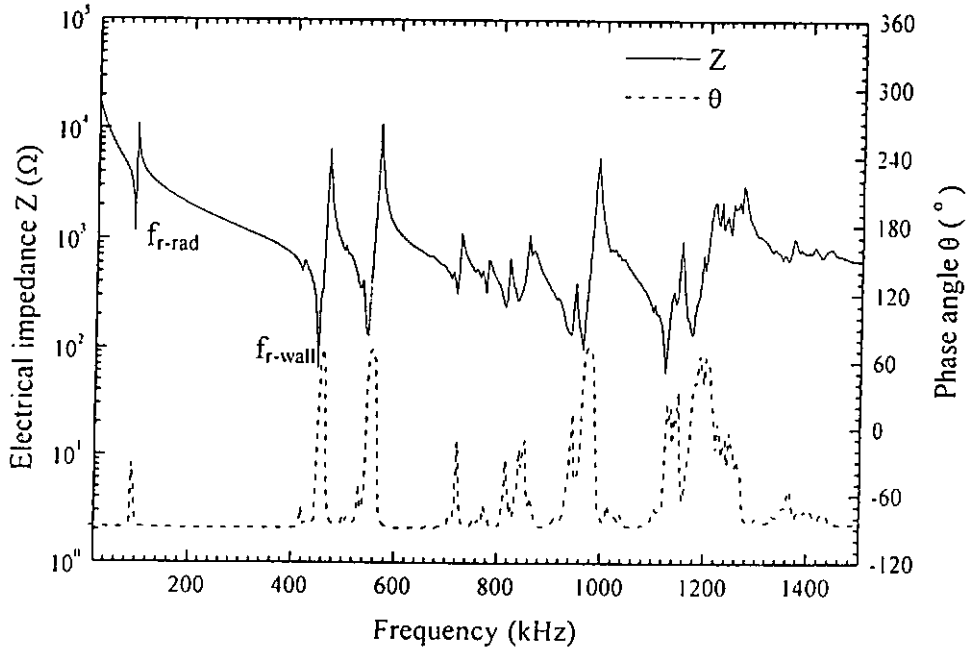

Composite ceramic volume fraction=0.92

Fig. 7.7 Electrical impedance Z and phase θ against frequency of a cake composite ring of thickness = 1.78 mm.

7.5 Structural design of a Langevin sandwich-type transducer

The function of a Langevin sandwich-type transducer is to convert electrical energy into longitudinal vibration energy based on the converse piezoelectric effect [Langevin, 1921]. It was designed to have a half-wave resonance to provide maximum power efficiency [Burgt, 1963]. Basically, the driver (Fig. 7.8) was formed by four piezoelectric rings stacked and clamped together with a bolt. The bolt was used to mechanically prestress the sandwich driver in the axial direction as a result of providing good mechanical coupling between the piezoelectric elements and metal plates. The front and end plates used were made by stainless steel to provide high power capability [Frederick, 1965]. The diameter of the metal plates is slightly larger than that of the piezoelectric rings in order to clamp the rings properly [TP-235, Morgan].

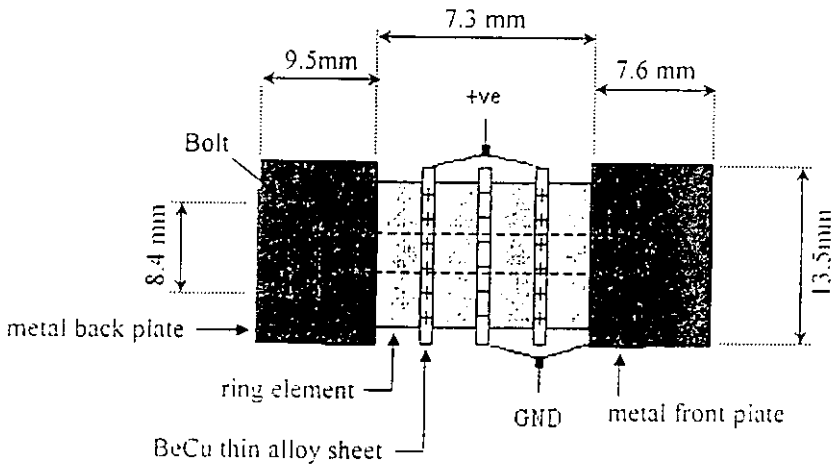

Fig. 7.8 Schematic diagram of a Langevin sandwich-type transducer.

The design of a sandwich type driver was used in applications such as ultrasonic cleaner and wire bonding. Several pieces of piezoelectric rings were stacked together and the whole sandwich structure resonated at about 62 kHz. Another advantage of the design is that by connecting the rings electrically in parallel can lower the electrical impedance [Blitz, 1971]. From Fig. 7.8, four piezoelectric rings were polarized in their thickness directions and were electrically connected in parallel. The mechanical vibration generated by the four piezoelectric rings in series can give increased total output displacement [Neppiras, 1973].

7.6 Electrical characterization of composite transducers

Piezoelectric, 1-3 composite and cake composite drivers were fabricated based on the Langevin sandwich structure as shown in Fig. 7.8. Electrical characteristics of the composite drivers were measured and compared with that of the piezoelectric driver. It is noted that after the drivers were assembled immediately, the electrical impedance and resonant frequency drifts with time and take up to one month before it reaches a steady value. The applied pressure during assembling can also affect its performance. So, a sufficient compressive pressure of 20 MPa was applied to the drivers to make sure that the drivers would vibrate as a whole system. Furthermore, the electrical properties of the drivers were obtained after the drivers had been kept under short-circuit condition for one month to make sure that the performance of the drivers had reached a stable condition.

From the electrical impedance spectra (Figs. 7.9-7.11), strong fundamental resonance mode corresponding to the longitudinal vibration along the axial direction of the drivers can be seen at about 62 kHz. The resonant frequencies of the composite drivers (Table 7.3) shifted slightly to lower frequency comparing with that of the PZT driver. In terms of material parameters, mechanical quality factors Q_M of the composite drivers were both lowered by about 20%. Electromechanical coupling factor k_{eff} of the composite drivers were not greatly affected comparing with that of the PZT driver.

On the other hand, the effect of planar mode coupling in the composite drivers declined. It is observed that the strong planar resonance mode at 130 kHz is greatly damped in both composite drivers. Therefore, an additional advantage of using the composite to fabricate driver operated at 130 kHz or above is that the operating axial mode will not coupled easily to the radial mode of the ring. Apart from the resonance modes of below 140 kHz, the resonance modes located at 170 kHz, 260 kHz and 390 kHz are harmonics of the thickness mode. Many small spurious modes were excited which may be due to non-uniform thickness of the hand-polished rings stacked in series.

Table 7.3 Material parameters of 1-3 composite, cake composite and piezoelectric sandwich drivers.

Material parameters		*1-3 composite driver*	*cake composite driver*	*piezoelectric driver*
Mechanical quality factor	Q_M	129	121	159
Fundamental resonant frequency (kHz)	f_r	61.16	61.19	63.39
Electromechanical coupling factor	k_{eff}	0.36	0.37	0.38
Electrical impedance At f_r (Ω)	Z_m	233.86	215.66	152.89

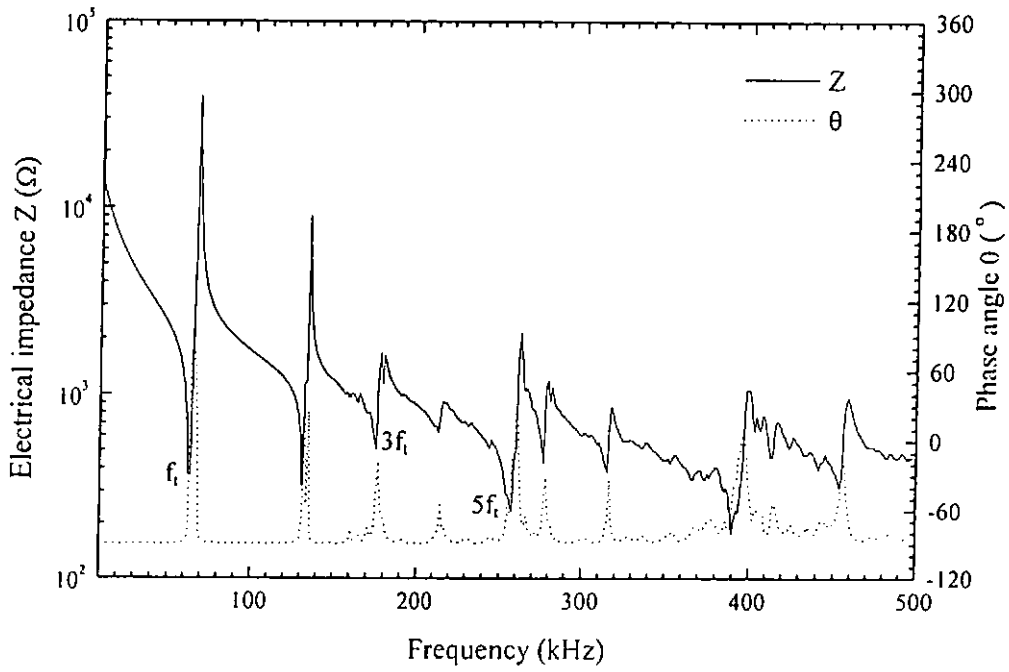

Fig. 7.9 Electrical impedance Z and phase θ against frequency of the PZT driver.

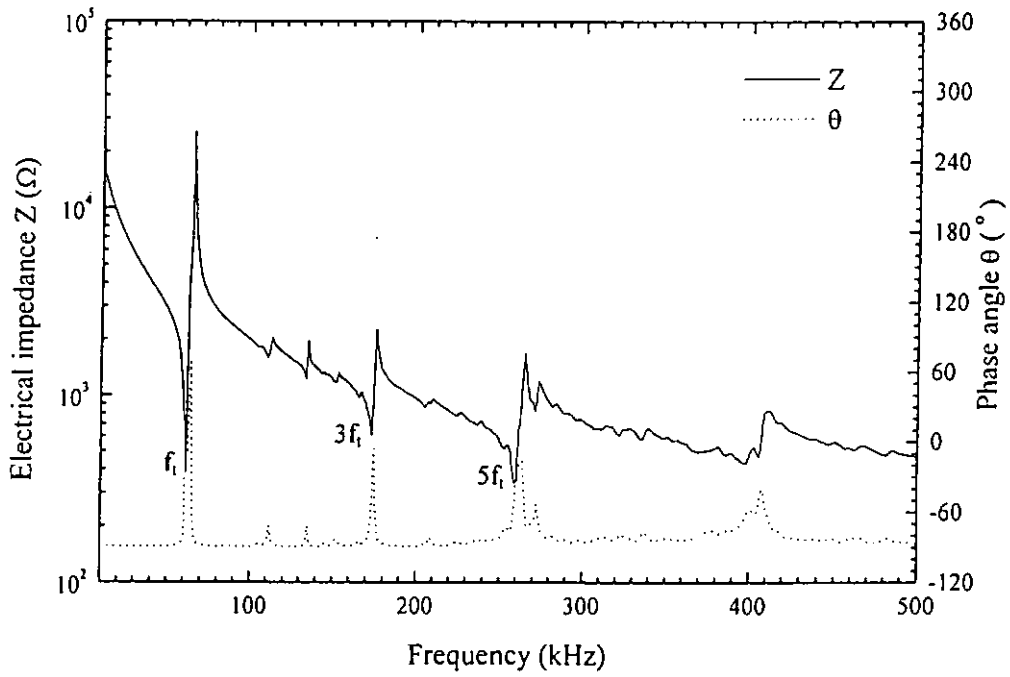

Fig. 7.10 Electrical impedance Z and phase θ against frequency of the 1-3 composite driver.

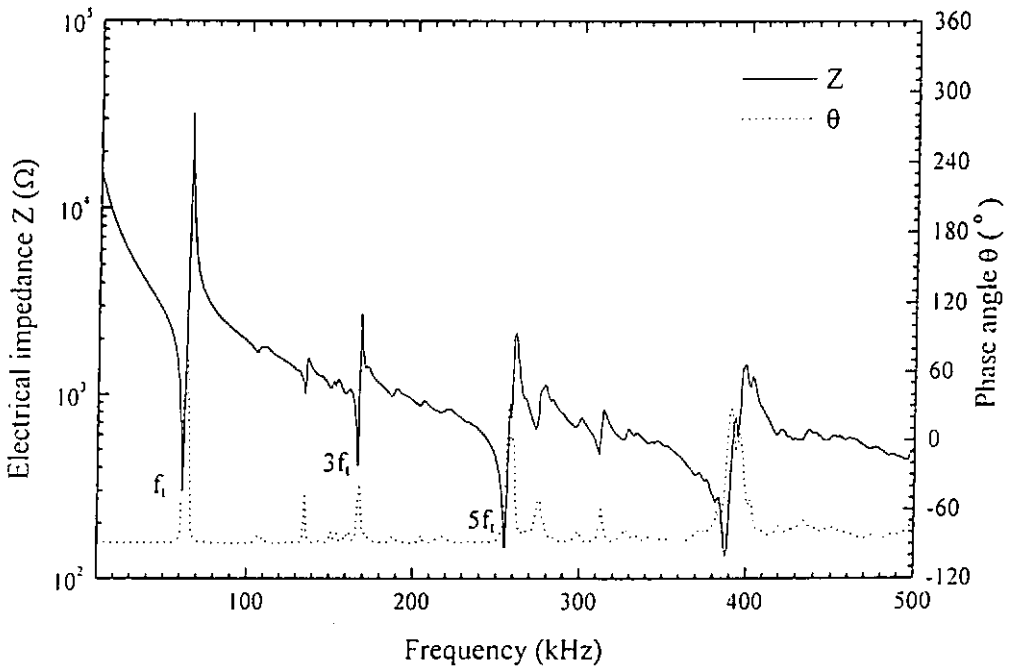

Fig. 7.11 Electrical impedance Z and phase θ against frequency of the cake composite driver.

CHAPTER 8

CONCLUSIONS AND SUGGESTIONS FOR FUTURE WORK

8.1 Conclusions

In this work, a 1-3 PMN-PT/epoxy composite and PZT/epoxy composite drivers for ultrasonic transducer applications have been fabricated and their electrical characteristics have been studied. In order to study the resonance characteristics of the 1-3 PMN-PT/epoxy and PZT/epoxy composites, material parameters of PMN-PT single crystals and PZT ceramics, namely, the elastic, piezoelectric and dielectric properties, have been evaluated with the resonance technique according to the IEEE standard (std. 76). The material parameters of PZT samples agree quite well with that of commercial PZT from the PKI and Morgan, indicating that the rings fabricated in our laboratory have good properties and that the measurement technique is valid. Furthermore, the material parameters of PMN-PT single crystal, (except k_{33}, d_{33} and $\varepsilon_{33}/\varepsilon_0$) which are not available in the literature have been reported in this work. Original data on the variation of materials parameters as a function of temperature change for the PMN-PT single crystals have also been found. Larger variation of material parameters for PMN-PT single crystals are found, presumably, due to its lower Curie temperature.

Elastic and electrical properties of epoxy used in the composite fabrication have been characterized. By using an ultrasonic immersion method, the acoustic properties such as the longitudinal velocity υ_L, shear velocity υ_S and longitudinal attenuation coefficient α have been determined. With the knowledge of υ_L, υ_S and α, other material parameters such as stiffness constants, compliance, mechanical quality factor have been evaluated and these are useful data that cannot be found in the manufacturer's data sheet. Furthermore, the variation of its properties with temperature has also been studied.

Piezoelectric coefficients d_{33}, d_{31} and hydrostatic charge coefficient d_h of the PMN-PT single crystals and PZT ceramics have been determined by using heterodyne interferometry and by subjecting the samples to hydrostatic pressure, respectively. The results have reasonable agreement with that measured by the resonance method.

In Chapter 6, resonance characteristics of the 1-3 PMN-PT/epoxy composite and the PMN-PT disc have been studied. There are four resonance modes in the 1-3 PMN-PT/epoxy composite. They are the planar-mode resonance f_p, thickness-mode resonance f_t, lateral-mode resonance f_L and stopband resonance f_s. Strong thickness mode and planar mode resonances and their harmonics exist in the PMN-PT disc. Comparing the resonance modes in PMN-PT and 1-3 PMN-PT/epoxy composite discs, a pure planar mode with a lower amplitude is found at the lowest frequency for the 1-3 composite whereas the strong planar mode with many harmonics exist in the PMN-PT disc. The thickness mode resonance with a broader bandwidth can be found in the 1-3 composite. Furthermore, material parameters of the 1-3 composite and the

PMN-PT disc have been evaluated. The mechanical quality factor Q_M in 1-3 composite was greatly reduced and the electromechanical coupling factor k_{33} was enhanced, indicating that the 1-3 composite is well suited for broad bandwidth transducer applications. On the other hand, in order to finely tailor material properties of the 1-3 composite for specific requirements of the device, thinning tests have been carried out. From the results of thinning tests, the shiftings and couplings in various resonance modes of the 1-3 composite have been observed.

In Chapter 7, by thinning tests of the PZT ring, mode coupling and the electromechanical properties have been studied. Optimal thickness of the PZT ring has been found for the ultrasonic wire bonding application. The electrical characteristics of two types of PZT/epoxy composite rings (cake and 1-3) with the optimized thickness had been fabricated. With four identical composite rings of each type, two composite drivers have been fabricated and characterized comparing with that of the PZT driver. Damping in planar mode vibrations and lower mechanical quality factor with a wider bandwidth are observed in the composite drivers.

8.2 Suggestions for future work

The characterization of 1-3 PMN-PT/epoxy composites with different single crystal volume fractions is a promising area to be studied in on-going research. PMN-PT single crystals are well-suited for applications that utilize their high d_{33} and d_{31} values. The cymbal actuator [Fernandez, 1998] is one possible application as it couples the d_{33} and d_{31} to give a high displacement. Using PMN-PT/epoxy to fabricate a dual-frequency transducer following the work of Chan et al [1989] will also be pursued in the near future.

LIST OF PUBLICATIONS

1. Or, S.W.; Chan, H.L.W.; Cheng, K.C.; Cheung, Y.M.; Yuen, C.W. and Liu, P.C.K. "Effect of tool drop on the performance of a high-frequency piezoelectric wire-bonding transducer system", *Ferroelectrics*, Vol.232, pp.217-222 (1999)

2. Chan, H.L.W.; Or, S.W.; Cheng, K.C. and Choy, C.L. "Ultrasonic Transducer", *US Patent, filed in USA*, serial no.09/296,801 (April,1999)

3. Cheng, K.C.; Chan, H.L.W.; Or, S.W. and Choy, C.L. "Mechanical Quality Factor of Lead Zirconate Titanate/Epoxy Composites", *Proc. MRS*, Vol.6.28 (2000)

4. Cheng, K.C.; Chan, H.L.W.; Choy, C.L.; Yin, Q.R.; Luo, H.S. and Yin, Z.W. "Piezoelectric coefficients of PMN-0.33PT Single Crystals", to be presented at *the 2000 Intl. Symp. On Application of Ferroelectrics*, Hawaii, U.S.A.

5. Cheng, K.C.; Chan, H.L.W.; Choy, C.L.; Yin, Q.R.; Luo. H.S. and Yin, Z.W. "Electromechanical Properties of PMN-PT Single Crystals", to be presented at *the 2000 Electroceramics conference*, Slovenia.

REFERENCES

Auld,B.A. "High frequency piezoelectric resonators", *Proc. IEEE International Symposium on Applications of Ferroelectrics (ISAF)* pp.288-295 (1986)

Berlincourt, D.A. and Krueger, H.H.A. *TP-226: Important properties of Morgan Matroc piezoelectric ceramics*, Morgan Matroc Limited, England (1987)

Berlincourt, D.A.; Curran, D.R. and Jaffe,H. "Piezoelectric and piezomagnetic materials and their function in transducers", In Mason, W.P., ed., *Physical Acoustics*, Vol.1, Part A, Academic Press, New York, pp.169-270 (1964)

Berlincourt, D.A. and Jaffe, H. "Elastic and piezoelectric coefficients of single-crystal barium titanate", *Physical Review*, Vol.111 (1958)

Blitz, J. "Ultrasonics methods and applications", *Butterworths*, London (1971)

Boas, M.L., *Mathematical Methods in the Physical Sciences*, Wiley, New York, pp.509-518 (1983)

Bond, W.L.; Mason, W.P. and McSkimin, H.J "Elastic and electromechanical coupling coefficients of single-crystal barium titanate", *Physical Review*, Vol.82 (1951)

Burgt, C.M. and Stuijts,A.L. "Motional positive feedback systems for ultrasonic power generators", *IEEE Transactions on Ultrasonic Engineering*, UE-10, No.2 (1963)

Chan, H.L.W.; Chan, W.K.; Zhang, Y.; Choy, C.L. "Pyroelectric and piezoelectric properties of lead titanate polyvinylidene fluoride-trifluoroethylene 0-3 composites", *IEEE Transactions*, Vol.5, No.4, pp.505-512 (1998)

Chan, H.L.W. and . Guy, I.L. "Piezoelectric ceramic/polymer composites for high frequency application", *Key Engineering Materials*, Vol.92-93, pp.275-300 (1994)

Chan, H.L.W. and Unsworth, J. "Simple model for piezoelectric ceramic/polymer 1-3 composites used in ultrasonic transducer applications", *IEEE Trans. on Ultra., Ferro., and Freq. Cont.*, Vol.36, No.4, pp.434-441 (1989)

Choi, S.W.; Shrout, T.R.; Jang, S.J. and Bhalla, A.S. "Dielectric and pyroelectric properties in the $Pb(Mg_{1/3}Nb_{2/3})O_3$-$PbTiO_3$ system", *Ferroelectrics*, Vol.100, pp.29-38 (1989)

Choi, S.W.; Shrout, T.R.; Jang, S.J. and Bhalla, A.S. "Morphotropic phase boundary in $Pb(Mg_{1/3}Nb_{2/3})O_3$-$PbTiO_3$ system", *Materials Letters*, Vol.8, pp.253-261 (1989)

Creedon, M.J.; Gopalakrishnan, S.; Schulze, W.A. "3-3 composite hydrophones from distorted reticulated ceramics", *Applications of Ferroelectrics, Proc. Of the Ninth IEEE International Symposium*, pp.299-302 (1994)

Cui, C.X.: Banghman, R.H.; Iqbal, Z.; Kazmar, T.R. and Dahlstorm,D.K. "Improved piezoelectrics for hydrophone applications based on calcium-modified lead titanate/poly(vinylidene fluoride) composites", *Seneors & Actuators*, A65, pp.76-85 (1998)

Fernandez, J.F.; Uchino, K.; Newnham, R.E.; Dogan, A. and Fielding, J.T. "Tailoring the performance of ceramic-metal piezocomposite actuators, Cymbals", *Sensors & Actuators*, A65, pp.228-237 (1998)

Frederick, J.R. *Ultrasonics Engineering*, John Wiley & Sons, New York (1965)

Geng, X., and Zhang, Q.M., "Resonance modes and losses in 1-3 piezocomposites for ultrasonic transducer applications", *J. Appl. Phys.*,Vol.85, No. 3, pp.1342-1350 (1999)

Geng, X.; Ritter, T.A. and Park, S.E. "Characterization of electromechanical properties of relaxor-PT piezoelectric single crystals", *IEEE Ultrasonics Symposium*, (1998)

Gupta, S.M. and Viehland, D. "Tetragonal to rhombohedral transformation in the lead zirconium titanate lead magnesium niobate-lead titanate crystalline solution", *J. Appl. Phys*, Vol.83, pp.407-415 (1998)

Gururaja, T.R.; Safari, A.; Newnham, R.E. and Cross, L.E. ,*Electronic Ceramics*, In Levinson, L.M. ed., Vol.92, Marcel Dekker, New York (1987)

Gururaja, T.R.; Schulze, W.A.; Cross, L.E.; Newnham, R.E.; Auld, B.A. and Wang, Y.J. "Piezoelectric composite materials for ultrasonic transducer applications. Part I: resonant modes of vibration of PZT rod-polymer composites", *IEEE Transactions on Sonics and Ultrasonics*, Vol.32 pp.481-498 (1985)

Hartmann,B. "Ultrasonic measurements", *Method of Experimental Physics*, Vol. 16C, Academic Press, pp.59-90 (1980)

Hayward, G. and Bennett, J. "Assessing the influence of pillar aspect ratio on the behavior of 1-3 connectivity composite transducers", *IEEE Transactions on Ultrasonics, Ferroelectrics and Frequency Control*, Vol.43, No.1, pp.98-108 (1996)

Heterodyne Probe SH-120 user manual, B.M. industries

Hueter, T.F. and Bolt R.H. *Sonics*, John Wiley & Sons (1955)

Igarashi, H. Mem. *Natl. Def. Acad.*, Vol.22, pp.27-31 (1982)

Ikeda, T. *Fundamentals of piezoelectricity*, Oxford University Press-Tokyo, pp.119-121 (1990)

IEEE standard on piezoelectricity, ANSI/IEEE Std. 176-1987.

"Guide to dynamic measurements of piezoelectric ceramics with high electromechanical coupling", *IEC standard* (1976)

"Measurement of piezoelectric ceramics", *IRE standards on piezoelectric crystals Proc. IRE, Vol. 49*, pp.1161-1169 (1961)

"Determination of the elastic, piezoelectric, and dielectric constants-the electromechanical coupling factor", *IRE standards on piezoelectric crystals, Proc. IRE46*, pp.764-778 (1958)

Jaffe, B.; Cook Jr, W.R. and Jaffe, H. "Historical Introduction", *Piezoelectric Ceramics*, Academic Press London and New York (1971)

Jaffe, B.; Roth, R.S. and Marzullo, S. *J. Appl. Phys*, Vol.25, pp.809-810 (1954)

Langevin, P. *British patent 145691* (1921)

Kwok, K.W.; Chan, H.L.W. and Choy, C.L. "Lead zirconate titanate/poly(vinylidene fluoride-trifluoroethylene composites for ultrasonic transducer applications", *IEEE Transactions, Ultra., Ferro. And Freq. Cont.*, Vol.3, pp.626-637 (1999)

Liu, S.F.; Park, S.E.; Shrout, T.R. and Cross, L.E. "Electric field dependence of piezoelectric properties for rhombohedral $0.955Pb(Zn_{1/3}Nb_{2/3})O_3$-$0.045PbTiO_3$ single crystal", *J. Appl. Phys.*, Vol.85, No.5, pp.2810-2814 (1999)

TP-235: The design of piezoelectric sandwich transducers, Morgan Matroc Limited, England (1987)

Mason, W.P. and Jaffe, H. "Methods for measuring piezoelectric, elastic, and dielectric coefficients of crystals and ceramics", *Proceeding of the IRE*, pp. 921-930 (1954)

Meyer, R.J., Jr.; Lopath, P.; Yoshikawa, S.; Shrout, T.R. "High frequency 1-3 composite transducers fabricated from alkoxide-derived PZT fibers", *IEEE Proc. Ultrasonics Symposium*, Vol.2, pp.915-918 (1997)

Neppiras,E.A. "The pre-stressed piezoelectric sandwich transducer", *Ultrasonic International Conference Proceedings* (1973)

Newnham, R.E. and Troliermckinstry S. "Crystals and composites", *J. Appl. Crystallography*, Vol.23, pp.447-457 (1990)

Newnham, R.E.; Bowen, L.J.; Klicker, K.A. and Cross, L.E. *Mat. Eng,* Vol.2, pp.93-97 (1980)

Newnham, R.E.; Skinner, D.P. and Cross, L.E. , "Connectivity and piezoelectric-pyroelectric composites", *Mat. Res,* Bull. Vol.13 ,pp.525-534 (1978)

Nye, J.F. *Physical properties of crystals*, Oxford at the Clarenoon Press, 322pp (1967)

Park, S.E. and Shrout, T.R. "Ultrahigh strain and piezoelectric behavior in relaxor based ferroelectric single crystals", *J. Appl. Phys.*, Vol.82, No.4, pp.1804-1811 (1997)

Park, S.E. and Shrout, T.R. "Characteristics of relaxor-based piezoelectric single crystals for ultrasonic transducers", *IEEE Trans. Ultrason., Ferroelect., Freq. Contr.*, Vol.44, No.5, pp.1140-1147 (1997)

Piezoelectric ceramics data book for designers, Morgan Matroc Limited, England (1987)

The data book of Piezo Kinetics Inc.

Read, B.E. and Dean, G.D. "The ultrasonic immersion method", *The Determination of Dynamic Properties of Polymers and Composite*, Adam Hilger (1978)

Ritter, T.; Shung, K.K.; Geng, X.; Wang, H.; Shrout, T.R. "30MhZ medical imaging arrays incorporating 2-2 composites", *IEEE Proc. Ultrasonics Symposium*, Vol.2, pp.1851-1855 (1998)

Rosen, C.Z.; Hiremath, B.V. and Newnham,R.E. *Piezoelectricity*, American Institute of Physics, New York (1992)

Royer, D. and Kmetik, V. "Measurement of piezoelectric constants using an optical heterodyne interferometer", *Electronics Letters*, Vol.28, pp.1828-1830 (1992)

Specification of product overview of Ciba Specialty Chemicals

Shrout, T.R.; Chang, Z.P.; Kim, N. and Markgraf, S. "Dielectric behavior of single crystals near the (1-x) $Pb(Mg_{1/3}Nb_{2/3})O_3$-(x) $PbTiO_3$ morphotropic phase boundary", *Ferroelectric Letters*, Vol.12, pp.63-69 (1990)

Shrout, T.R. and Fielding, J. "Relaxor ferroelectric materials", *Proc. IEEE. Ultra. Symp.*, Vol.2, pp.711-720 (1990)

Smith, W.A. and Auld, B.A. "Modeling 1-3 composite piezoelectrics-thickness mode oscillations", *IEEE Trans. Ultrason. Ferroelectrics Freq. Controls* Vol.38, pp.40-47 (1991)

Smith, W.A. "The role of piezocomposites in ultrasonic transducers", *Proc. IEEE Ultrasonics Symposium*, pp.755-766 (1989)

Smith, W.A. "Composite piezoelectric materials for medical ultrasonic imaging transducers – A review", *Proc. IEEE International Symposium on Application of Ferroelectrics (ISAF)*, pp.249-256 (1986)

Standard test method for water absorption, bulk density, apparent porosity, and apparent specific gravity of fired whiteware products C373-72.

Tanaka, T. "Piezoelectric devices in Japan", *Ferroelectrics*, Vol.40, pp.167-187 (1982)

Tancrell, R.H.; Wilson, D.T. and Ricketts, D. "Properties of PVDF polymer for sensor", *Proc. IEEE Ultrasonic Symposium*, pp.624-629 (1985)

Tummala, R.R. and Rymaszewski, E.J., *Microelectronic Packaging Handbook*, Van Nostrand Reinhold (1989)

Xu, Y. "Perovskite-type ferroelectrics: part I", *Ferroelectric materials and their applications*, pp.101-162, North-Holland (1991)

Yin, J.; Jiang, B. and Cao, W. "Elastic, piezoelectric, and dielectric properties of $0.955Pb(Zn_{1/3}Nb_{2/3})O_3$-$0.45PbTiO_3$ single crystal with designed multidomains", *IEEE Transactions of UFFC.*, Vol.47, pp.285-291 (2000)

Yin, Z.W.; Luo, H.S.; Wang, P.C. and Xu, G.S. "Growth characterization and properties of relaxor ferroelectric PMN-PT single crystals", *Ferroelectrics*, Vol 231, pp.97-102 (1999)

Zhang, Q.M.; Pan, W.Y. and Cross, L.E. "Laser interferometer for the study of piezoelectric and electrostrictive strains", *J. Appl. Phys*, Vol.63, pp.2492-2497 (1988)

Zhao, Z.; Chan, H.L.W. and Choy, C.L. "Determination of the piezoelectric coefficient d_{33} at high frequency by laser interferometry", *Ferroelectrics*, Vol.195 pp.35-38 (1997)

Zhao, J.Z. and Zhang, Q.M. "Effect of mechanical stress on the electromechanical performance of PZT and PMN-PT ceramics", *IEEE Trans. Ultrason., Ferroelect., Freq. Contr.*, pp.971-974 (1996)

Appendix A

Vibration modes in piezoelectric samples

A.1 Lateral extensional mode of a bar

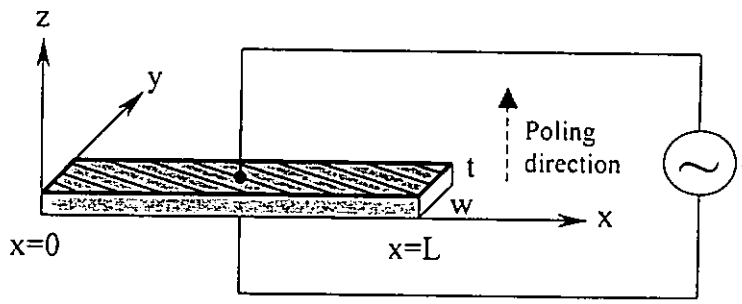

Fig. A.1 A length-expander bar with the electric field perpendicular to its length.

A long piezoelectric bar with electroded surfaces normal to the z direction which is parallel to the poling direction as shown in Fig. A.1 is used in determining s_{11}^E and k_{31}.

Assume the cross-sectional dimensions are very small compared with its length,

$$L >> w, t$$

Since the bar is free to vibrate in the x and y directions and its electroded surfaces form equipotential surfaces in the z direction, constant-T & constant-E are thus chosen as independent variables respectively. The following piezoelectric equations are given [Berlincourt,1964]:

$$S = s^E T + dE \tag{A.1}$$

$$D = dT + \varepsilon^T E \tag{A.2}$$

Since the thickness t is negligibly small, the following conditions apply:

$$E_1 = E_2 = 0$$

$$T_2 = T_3 = T_4 = T_5 = T_6 = 0$$

$$\frac{\partial E_3}{\partial x} = \frac{\partial E_3}{\partial y} = 0$$

$$S_1 = s_{11}^E T_1 + d_{31} E_3 \tag{A.3}$$

$$D_3 = d_{31} T_1 + \varepsilon_{33}^T E_3 \tag{A.4}$$

According to Newton's 2nd law, $F = ma$ (A.5)

Substitute the force acting on a yz plane $F = \frac{\partial T_1}{\partial x} dx \cdot dy \cdot dz$,

mass $m = \rho \cdot dx \cdot dy \cdot dz$, strain in the x direction $S_1 = \frac{\partial \xi_1}{\partial x}$

and acceleration $a = \frac{\partial^2 \xi_1}{\partial t^2}$ into Eq. (A.5).

The wave equation is derived as follows:

$$\rho \frac{\partial^2 \xi_1}{\partial t^2} dxdydz = \frac{\partial T_1}{\partial x} dxdydz \tag{A.6}$$

where ξ_1 is the particle displacement

Substituting $S_1 = \frac{\partial \xi_1}{\partial x}$ into Eq.(A.3), thus giving

$$S_1 = s_{11}^E T_1 + d_{31} E_3$$

$$T_1 = \frac{1}{s_{11}^E} S_1 - \frac{d_{31}}{s_{11}^E} E_3$$

$$T_1 = \frac{1}{s_{11}^E} \cdot \frac{\partial \xi_1}{\partial x} - \frac{d_{31}}{s_{11}^E} E_3 \tag{A.7}$$

$$\frac{\partial T_1}{\partial x} = \frac{1}{s_{11}^E} \cdot \frac{\partial^2 \xi_1}{\partial x^2} - \frac{d_{31}}{s_{11}^E} \cdot \frac{\partial E_3}{\partial x}$$

From the above condition, $\frac{\partial E_3}{\partial x} = 0$, the electroded surfaces are equipotential surfaces making E_3 independent of x, hence

$$\frac{\partial^2 \xi_1}{\partial t^2} = \frac{1}{\rho s_{11}^E} \frac{\partial^2 \xi_1}{\partial x^2} = \left(\upsilon_b^E\right)^2 \frac{\partial^2 \xi_1}{\partial x^2} \tag{A.8}$$

where $\upsilon_b^E = (\frac{1}{\rho \cdot s_{11}^E})^{\frac{1}{2}}$ v_b^E is the velocity of longitudinal waves in a bar (at constant-E condition).

For a sinusoidal excitation $E_3 = E_0 e^{j \cdot \omega \cdot t}$ and $\xi_1 = \xi 0 e^{j \cdot \omega \cdot t}$ with

$$\frac{\partial^2 \xi_1}{\partial t^2} = -\omega^2 e^{j \cdot \omega \cdot t} \xi_0 \qquad \text{and} \qquad \frac{\partial^2 \xi_1}{\partial x^2} = \frac{\partial^2 \xi_0}{\partial x^2} \cdot e^{j \cdot \omega \cdot t}$$

substituting into Eq. (A.8), giving

$$\frac{\partial^2 \xi_0}{\partial x^2} + (\frac{\omega}{\upsilon_b^E})^2 \cdot \xi_0 = 0 \tag{A.9}$$

The solution to Eq. (A.9) is

$$\xi_0 = \left[A \sin(\omega \ x / \upsilon_b^E) + B \cos(\omega \ x / \upsilon_b^E)\right]$$

$$\xi_1 = \left[A \sin(\omega \ x / \upsilon_b^E) + B \cos(\omega \ x / \upsilon_b^E)\right] e^{j \omega t} \tag{A.10}$$

To solve for A:

At x=0 and L, which is located at the free surfaces , the stress T_1=0,

From Eq. (A.10) gives

$$\frac{\partial \xi_0}{\partial x} = A \cdot \frac{\omega}{\upsilon_b^E} \cos(\frac{\omega \cdot x}{\upsilon_b^E}) - B \cdot \frac{\omega}{\upsilon_b^E} \sin(\frac{\omega x}{\upsilon_b^E})$$

When x=0, $$B \cdot \frac{\omega}{\upsilon_b^E} \sin(\frac{\omega \cdot 0}{\upsilon_b^E}) = 0$$

Such that $$\frac{\partial \xi_0}{\partial x} = A \cdot \frac{\omega}{\upsilon_b^E} \tag{A.11}$$

According to Eq. (A.3), when x=0, T_1=0,

Then $$S_1 = d_{31}E_3$$

$$S_1 = \frac{\partial \xi_1}{\partial x} = \frac{\partial \xi_0}{\partial x} e^{j\cdot\omega\cdot t} = d_{31}E_3 = d_{31}E_0 e^{j\cdot\omega\cdot t}$$

$$\frac{\partial \xi_0}{\partial x} = d_{31}E_0$$

Put the above Equations into Eq. (A.11), A can be found.

$$A = \frac{d_{31}E_0 \upsilon_b^E}{\omega} \tag{A.12}$$

To solve for B:

$$\frac{\partial \xi_0}{\partial x} = A \cdot \frac{\omega}{\upsilon_b^E}\cos(\frac{\omega \cdot x}{\upsilon_b^E}) - B \cdot \frac{\omega}{\upsilon_b^E}\sin(\frac{\omega \cdot x}{\upsilon_b^E}) \tag{A.13}$$

When x=L, T_1=0, put Eq. (A.12) into Eq. (A.13)

$$B = \frac{\upsilon_b^E d_{31}E_0\left[\cos(\omega L/\upsilon_b^E) - 1\right]}{\omega \sin(\omega L/\upsilon_b^E)} \tag{A.14}$$

Since $\xi_1 = \xi_0 e^{j\cdot\omega\cdot t}$, put solution of A and B into Eq. (A.10),

$$\xi_1 = \frac{\upsilon_b^E}{\omega}\left\{\sin\frac{\omega x}{\upsilon_b^E} + \frac{\left[\cos(\omega L/\upsilon_b^E) - 1\right]}{\sin(\omega L/\upsilon_b^E)}\cos\frac{\omega x}{\upsilon_b^E}\right\} d_{31}E_0 e^{j\omega t} \tag{A.15}$$

Strain $$S_1 = \frac{\partial \xi_1}{\partial x} = \{\cos(\frac{\omega \cdot x}{\upsilon_b^E}) + \frac{(1-\cos(\omega \cdot L/\upsilon_b^E))}{\sin(\omega \cdot L/\upsilon_b^E)} \cdot \sin(\frac{\omega \cdot x}{\upsilon_b^E})\} \cdot d_{31}E_3 \tag{A.16}$$

The admittance (=1/Impedance Z) of the vibrating bar is given by

$$\frac{1}{Z} = \frac{I}{V} = \frac{w\int_0^L \frac{dD_3}{dL}\,dx}{\int_0^t E_3\,dz} \tag{A.17}$$

Put Eq. (A.7) in Eq. (A.4),

$$D_3 = (\frac{S_1}{s_{11}^E} - \frac{d_{31}E_3}{s_{11}^E})d_{31} + \varepsilon_{33}^T E_3 \tag{A.18}$$

Substituting Eq. (A.16) and Eq. (A.20) into Eq. (A.18)

$$D_3 = \left\{\varepsilon_{33}^T(1-k_{31}^2) + \varepsilon_{33}^T k_{31}^2\left[\cos\frac{\omega x}{\upsilon_b^E} - \frac{\cos(\omega L/\upsilon_b^E)-1}{\sin(\omega L/\upsilon_b^E)}\sin\frac{\omega x}{\upsilon_b^E}\right]\right\}E_0 e^{j\omega t} \tag{A.19}$$

where the coupling factor k_{31} is given by

$$k_{31}^2 = (d_{31}^2 / s_{11}^E \varepsilon_{33}^T) \tag{A.20}$$

$$\frac{dD_3}{dt} = \{\varepsilon_{33}^T \cdot k_{31}^2(\cos(\frac{\omega\cdot x}{\upsilon_b^E}) + \frac{1-\cos(\omega\cdot L/\upsilon_b^E)}{\sin(\omega\cdot x/\upsilon_b^E)}\sin(\frac{\omega\cdot x}{\upsilon_b^E})) + \varepsilon_{33}^T(1-k_{31}^2)\}\frac{dE_3}{dt}$$

since $I = W\int_0^L \frac{dD_3}{dt}\,dx$

$$I = j\omega E_0 e^{j\cdot\omega\cdot t} W\cdot L\cdot\varepsilon_{33}^T\{(1-k_{31}^2) + k_{31}^2\cdot\frac{tg(\omega\cdot L/2\upsilon_b^E)}{\omega\cdot L/2\upsilon_b^E}\} \tag{A.21}$$

$$(\because\ \mathrm{tg}\frac{\alpha}{2} = \frac{(1-\cos\alpha)}{\sin\alpha})$$

It should be noted that $\varepsilon_{33}^T(1-k_{31}^2)$ is the longitudinally clamped permittivity.

Since $$V = \int_0^t E_3\,dz = t\cdot E_0 e^{j\cdot\omega\cdot t} \tag{A.22}$$

The admittance of the vibrating bar can then be obtained by substituting Eq. (A.21), (A.22) into Eq. (A.17),

$$\frac{1}{Z} = j\omega \frac{L\omega}{t} \varepsilon_{33}^{T} \left\{ (1-k_{31}^2) + k_{31}^2 \frac{\tan(\omega L / 2\upsilon_b^E)}{\omega L / 2\upsilon_b^E} \right\} \tag{A.23}$$

Free permittivity ε_{33}^T can be obtained directly from an impedance measurement at low frequency (eg. 1 kHz).

At resonance of an unloaded bar with no loss, the admittance becomes infinite, such that $\tan \frac{\omega L}{2\upsilon_b^E} = \infty$

$$f_r = \frac{\upsilon_b^E}{2L} = \frac{1}{2L} \cdot \sqrt{\frac{1}{\rho \cdot s_{11}^E}} \tag{A.24}$$

This is followed by a zero admittance at anti-resonance f_a given by

$$\frac{\tan[(\pi/2)(f_a/f_r)]}{(\pi/2)(f_a/f_r)} = \frac{k_{31}^2 - 1}{k_{31}^2} \tag{A.25}$$

Conversely, k_{31} can be calculated from the measured values of f_r and f_a using Eq. (A.25).

s_{11}^E can be determined by

$$s_{11}^E = \frac{1}{\rho (2Lf_r)^2} \tag{A.26}$$

A.2 Length extensional mode of a rod

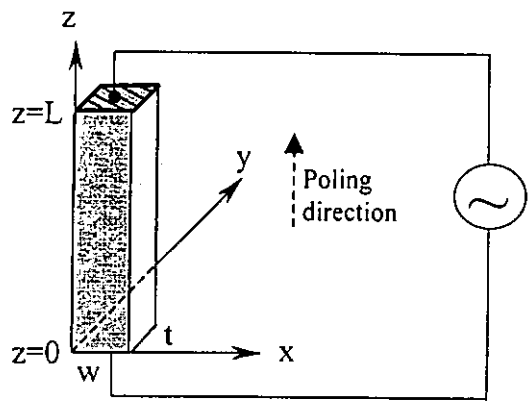

Fig. A.2 A long rod with the electric field parallel to its length.

A long piezoelectric rod with electroded surfaces normal to the z (poling) direction as shown in Fig. A.2 is used in determining s_{33}^E, $s_{33}^D$and k_{33}.

Consider the rod is so long that the permittivity of the bar is sufficiently greater than that of its surroundings to prevent fringing electric fields, electric flux lines will also be parallel to its length, such that $D_1 = D_2 = 0$, $\partial D_3/\partial z=0$. With negligible cross-sectional dimensions, all stresses will be zero except T_3. Hence, D and T are chosen as independent variables, giving piezoelectric equations as: [Berlincourt,1964]

$$S_3 = s_{33}^D T_3 + g_{33} D_3 \tag{A.27}$$

$$E_3 = -g_{33} T_3 + \varepsilon_{33}^T D_3 \tag{A.28}$$

From Eq. (A.27),

$$T_3 = \frac{1}{s_{33}^D} S_3 - \frac{g_{33}}{s_{33}^D} D_3 \tag{A.29}$$

According to Newton's 2nd law,

$$\rho \frac{\partial^2 \xi_3}{\partial t^2} = \frac{\partial T_3}{\partial z} \tag{A.30}$$

where ξ_3 is the particle displacement in the z direction. Substituting Eq. (A.29) into Eq. (A.30) and recalling $S_3 = (\partial \xi_3 / \partial z)$,

$$\rho \frac{\partial^2 \xi_3}{\partial t^2} = \frac{1}{s_{33}^D} \cdot \frac{\partial^2 \xi_3}{\partial z^2} \tag{A.31}$$

Solution of ξ_3 is given by

$$\xi_3 = \{A \cdot \sin(\frac{\omega \cdot z}{\upsilon_b^D}) + B \cdot \cos(\frac{\omega \cdot z}{\upsilon_b^D})\} \cdot e^{j \cdot \omega \cdot t} \tag{A.32}$$

where $\upsilon_b^D = (\frac{1}{\rho s_{33}^D})^{\frac{1}{2}}$ is the longitudinal velocity in a rod (constant D-conditions).

At the ends of a rod (z=0, z=L), T_3=0,

$$\frac{\partial \xi_3}{\partial z} = \{\frac{\omega}{\upsilon_b^D} \cdot A \cdot \cos(\frac{\omega \cdot z}{\upsilon_b^D}) - \frac{\omega}{\upsilon_b^D} \cdot B \cdot \sin(\frac{\omega \cdot z}{\upsilon_b^D})\} \cdot e^{j \cdot \omega \cdot t} \tag{A.33}$$

To solve for A:

When z=0, $\sin(\frac{\omega \cdot z}{\upsilon_b^D}) = 0$

Such that Eq. (A.33) would become

$$\frac{\partial \xi_3}{\partial z} = \frac{\omega}{\upsilon_b^D} \cdot A \cdot e^{j \cdot \omega \cdot t} \tag{A.34}$$

as at z=0, T_3=0, Eq. (A.27) gives

$$\frac{\partial \xi_3}{\partial z} = g_{33} D_3 \tag{A.35}$$

Put $D_3 = D_0 e^{j \cdot \omega \cdot t}$ and Eq. (A.35) into Eq. (A.34), A can be solved.

$$A = \frac{g_{33} \cdot \upsilon_b^D \cdot D_0}{\omega} \tag{A.36}$$

To solve for B:

When z=L, T_3=0,

Put Eq. (A.35) and Eq. (A.36) into Eq. (A.33), giving

$$\{\frac{\omega}{\upsilon_b^D} \cdot \frac{g_{33} D_0 \upsilon_b^D}{\omega} \cdot \cos(\frac{\omega \cdot L}{\upsilon_b^D}) - \frac{\omega}{\upsilon_b^D} \cdot B \cdot \sin(\frac{\omega \cdot L}{\upsilon_b^D})\} e^{j \cdot \omega \cdot t} = g_{33} D_0 e^{j \cdot \omega \cdot t}$$

$$B = \frac{g_{33} D_0 \upsilon_b^D \cos(\omega \cdot L / \upsilon_b^D) - g_{33} \upsilon_b^D D_0}{\omega \cdot \sin(\omega \cdot L / \upsilon_b^D)} \tag{A.37}$$

Substituting Eq. (A.36) and Eq. (A.37) into Eq. (A.32),

$$\xi_3 = \{\frac{g_{33} \upsilon_b^D D_0}{\omega} \sin(\frac{\omega \cdot z}{\upsilon_b^D}) + \frac{g_{33} \upsilon_b^D D_0 \cos(\omega \cdot L / \upsilon_b^D) - g_{33} \upsilon_b^D D_0}{\omega \cdot \sin(\omega \cdot L / \upsilon_b^D)} \cdot \cos(\frac{\omega \cdot z}{\upsilon_b^D})\} \cdot e^{j \cdot \omega \cdot t}$$

Since $tg \frac{\alpha}{2} = \frac{1 - \cos\alpha}{\sin\alpha} = -\frac{\cos\alpha - 1}{\sin\alpha}$

$$\xi_3 = \frac{\upsilon_b^D g_{33} D_0}{\omega} \cdot \{\sin(\frac{\omega \cdot z}{\upsilon_b^D}) - tg \frac{\omega \cdot L}{2\upsilon_b^D} \cos(\frac{\omega \cdot z}{\upsilon_b^D})\} \tag{A.38}$$

From Eq. (A.27) and Eq. (A.28),

$$T_3 = \frac{S_3}{s_{33}^D} - \frac{g_{33}}{s_{33}^D} D_3 \tag{A.39}$$

$$E_3 = -\frac{g_{33}}{s_{33}^D} S_3 + (\frac{g_{33}^2}{s_{33}^D} + \beta_{33}^T) D_3 \tag{A.40}$$

$$S_3 = \frac{\partial \xi_3}{\partial z} = \frac{\upsilon_b^D g_{33} D_3}{\omega} \cdot \frac{\omega}{\upsilon_b^D} \{\cos(\frac{\omega \cdot z}{\upsilon_b^D}) + tg(\frac{\omega \cdot L}{2\upsilon_b^D}) \sin(\frac{\omega \cdot z}{\upsilon_b^D})\} \tag{A.41}$$

Substituting Eq. (A.41) into Eq. (A.40),

$$E_3 = -\frac{g_{33}^2 D_3}{s_{33}^D}\{\cos(\frac{\omega \cdot z}{\upsilon_b^D}) + tg(\frac{\omega \cdot L}{2\upsilon_b^D}) \cdot \sin(\frac{\omega \cdot z}{\upsilon_b^D})\} + (\frac{g_{33}^2}{s_{33}^D} + \beta_{33}^T)D_3 \qquad \text{(A.42)}$$

Since

$$V = \int_0^L E_3 dz = \{L(\frac{g_{33}^2}{s_{33}^D} + \beta_{33}^T) - \frac{2g_{33}^2 \upsilon_b^D}{s_{33}^D \omega} \cdot tg(\frac{\omega \cdot L}{2\upsilon_b^D})\}D_3 \qquad \text{(A.43)}$$

The impedance equation of the rod vibrating along the z direction is given by:

$$Z = \frac{V}{I} = \frac{1}{j\omega} \cdot \frac{L}{w \cdot t} \cdot \{(\frac{g_{33}^2}{s_{33}^D} + \beta_{33}^T) - \frac{g_{33}^2}{s_{33}^D} \cdot \frac{2\upsilon_b^D}{L \cdot w} tg(\frac{\omega \cdot L}{2\upsilon_b^D})\}$$

$$Z = \frac{1}{j\omega C_s}\{1 - k_{33}^2 \frac{\tan(\omega L / 2\upsilon_b^D)}{\omega L / 2\upsilon_b^D}\} \qquad \text{(A.44)}$$

where

$$C_s = \frac{A}{L\beta_{33}^S} = \frac{A\varepsilon_{33}^S}{L} \qquad \text{(A.45)}$$

$$\beta_{33}^S = \beta_{33}^T(1 + \frac{g_{33}^2}{\beta_{33}^T s_{33}^D}) \qquad \text{(A.46)}$$

$$k_{33}^2 = \frac{g_{33}^2}{\beta_{33}^T s_{33}^D + g_{33}^2} \qquad \text{(A.47)}$$

$$\upsilon_b^D = (\frac{1}{\rho s_{33}^D})^{\frac{1}{2}} \qquad \text{(A.48)}$$

$$k_{33}^2 = \frac{d_{33}^2}{s_{33}^E \varepsilon_{33}^T} = \frac{\varepsilon_{33}^T g_{33}^2}{s_{33}^E} \qquad \text{(A.49)}$$

where A is the cross-sectional area w·t . C_s is the clamped capacitance.

At anti-resonance f_a, $z \rightarrow \infty$

From Eq. (A.44), $$tg\frac{\omega_a \cdot L}{2\upsilon_b^D} = \infty \quad \text{or} \quad \frac{\omega_a \cdot L}{2\upsilon_b^D} = \frac{\pi}{2}$$

Therefore, $$f_a = \frac{\upsilon_b^D}{2L} = \frac{1}{2L(\rho \cdot s_{33}^D)^{1/2}}$$

s_{33}^D can be calculated using

$$s_{33}^D = \frac{1}{\rho(2Lf_a)^2} \tag{A.50}$$

At resonance f_r, z=0,

From Eq. (A.44), $$1 - k_{33}^2\left(\frac{2\upsilon_b^D}{\omega \cdot L}\right) \cdot tg\left(\frac{\omega \cdot L}{2\upsilon_b^D}\right) = 0$$

$$k_{33}^2 = \frac{\pi}{2}\frac{f_r}{f_a}\tan\left(\frac{\pi}{2}\frac{f_a - f_s}{f_a}\right) \tag{A.51}$$

s_{33}^E can be calculated using

$$s_{33}^E = \frac{s_{33}^D}{(1 - k_{33}^2)} \tag{A.52}$$

A.3 Radial mode of a thin disc

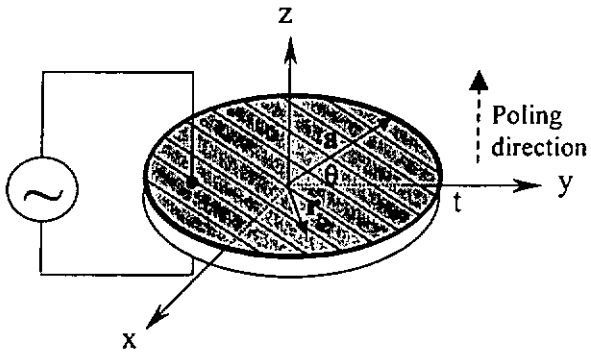

Fig. A.3 A thin disc with the electric field parallel to its thickness.

A thin piezoelectric disc with electroded surfaces perpendicular to the poling direction as shown in Fig. A.3 is used for determining k_p and σ^P.

Assume the disc radius *a* is large compared to its thickness *t*, (a/t > 20). Consider strong mode vibration existing in the plane normal to the poling direction and the thickness t is negligibly small, such that $T_{33}=T_{r3}=T_{\theta 3}=0$ and $\xi_\theta=\xi_3=0$, $T_{r\theta}=0$, throughout the disc. Electric field is applied along the z direction such that $D_r=D_\theta=0$. constant-T & constant-E are thus chosen as independent variables respectively.[Ikeda, 1990]

The constitute equations of the system are given by:

$$S_{rr} = s_{11}^E T_{rr} + s_{12}^E T_{\theta\theta} + d_{31} E_3 \tag{A.53}$$

$$S_{\theta\theta} = s_{12}^{E\,E} T_{rr} + s_{11}^E T_{\theta\theta} + d_{31} E_3 \tag{A.54}$$

$$D_3 = d_{31}(T_{rr} + T_{\theta\theta}) + \varepsilon_{33}^T E_3 \tag{A.55}$$

From Eqs. (A.53) and (A.54),

$$T_{rr} = c_{11}^{P} S_{rr} + c_{11}^{P} \sigma^{P} S_{\theta\theta} - e_{31}^{P} E_3 \tag{A.56}$$

$$T_{\theta\theta} = c_{11}^{P} \sigma^{P} S_{rr} + c_{11}^{P} S_{\theta\theta} - e_{31}^{P} E_3 \tag{A.57}$$

where

$$\sigma^{P} = -\frac{s_{12}^{E}}{s_{11}^{E}} \tag{A.58}$$

$$c_{11}^{P} = \frac{1}{s_{11}^{E}(1-(\sigma^{P})^2)} = \frac{s_{11}^{E}}{(s_{11}^{E})^2 - (s_{12}^{E})^2} \tag{A.59}$$

$$e_{31}^{P} = \frac{d_{31}}{s_{11}^{E} + s_{12}^{E}} \tag{A.60}$$

Substituting Eqs. (A.56), (A.57), (A.58), (A.59), (A.60) into (A.55),

$$D_3 = e_{31}^{P} S_{rr} + e_{31}^{P} S_{\theta\theta} + \varepsilon_{33}^{P} E_3 \tag{A.61}$$

where

$$\varepsilon_{33}^{P} = \varepsilon_{33}^{T} - 2e_{31}^{P} d_{31} = \varepsilon_{33}^{T}(1-k_p^2) \tag{A.62}$$

$$k_p^2 = \frac{2d_{31}^2}{s_{11}^{E}(1-\sigma^{P})\varepsilon_{33}^{T}} \tag{A.63}$$

By Newton's 2nd law for the case of radial mode vibration,

$$\rho \frac{\partial^2 \xi_r}{\partial t^2} = \frac{\partial T_{rr}}{\partial r} + \frac{T_{rr} - T_{\theta\theta}}{r} \tag{A.64}$$

where ξ_r is the particle displacement in the radial direction. By substituting Eqs. (A.56) and (A.57) and using $S_{rr} = \dfrac{\partial \xi_{rr}}{\partial r}$ (A.65)

$$S_{\theta\theta} = \frac{1}{r} \cdot \frac{\partial \xi_{\theta\theta}}{\partial \theta} + \frac{\xi_r}{r} \tag{A.66}$$

into Eq. (A.64)

As ξ_θ=0,

$$\rho \frac{\partial^2 \xi_r}{\partial t^2} = c_{11}^{P} \frac{\partial^2 \xi_r}{\partial r^2} + \frac{c_{11}^{P}}{r} \cdot \left(\frac{\partial \xi_r}{\partial r} - \frac{\xi_r}{r}\right) \tag{A.67}$$

Assume $E_3 = E_0 e^{j\cdot\omega\cdot t}$ and $\xi_r = \xi_0 e^{j\cdot\omega\cdot t}$

Then
$$\frac{\partial^2 \xi_0}{\partial r^2} + \frac{1}{r}\frac{\partial \xi_0}{\partial r} + (\frac{\omega^2}{(\upsilon^P)^2} - \frac{1}{r^2})\xi_0 = 0 \tag{A.68}$$

where
$$\upsilon^P = \sqrt{\frac{c_{11}^P}{\rho}} \tag{A.69}$$

Eq. (A.68) is in the form of Bessel equation and hence the general solution is given by [Boas, 1983]

$$\xi_0 = A \cdot J_1(\frac{\omega \cdot r}{\upsilon^P}) e^{j\cdot\omega\cdot t} \tag{A.70}$$

where A is a constant determined by the boundary conditions J_0 and J_1 is the zeroth and first order Bessel functions of the first kind as given in Eq. (A.71).

$$J_0(y) = \sum_{n=0}^{\infty} \frac{(-1)^n}{n!n!} (\frac{y}{2})^{2n} \tag{A.71}$$

$$J_1(y) = \sum_{n=0}^{\infty} \frac{(-1)^n}{n!(n+1)!} (\frac{y}{2})^{2n+1}$$

Therefore, from Eqs. (A.56), (A.57), (A.65), (A.66), we have

$$T_{rr} = \frac{A \cdot c_{11}^P \cdot \omega}{2\upsilon^P}[J_0(\frac{\omega \cdot r}{\upsilon^P}) - J_2(\frac{\omega \cdot r}{\upsilon^P})]e^{j\cdot\omega\cdot t} + \frac{A \cdot c_{11}^P \cdot \sigma^P}{r} J_1(\frac{\omega \cdot r}{\upsilon^P}) e^{j\cdot\omega\cdot t} - e_{31}^P E_0 e^{j\cdot\omega\cdot t} \tag{A.72}$$

where J_0 and J_2 are the zeroth and second order Bessel functions of the first kind, respectively. Since $T_{rr} = 0$ at $r = a$, then

$$A = \frac{e_{31}^P \cdot a \cdot E_0}{c_{11}^P J_1(\frac{\omega \cdot a}{\upsilon^P}) \cdot [\Im(\frac{\omega \cdot a}{\upsilon^P}) - (1 - \sigma^P)]} \tag{A.73}$$

where $\Im(y) = yJ_{0(y)} / J_1(y)$ is the modified quotient of the Bessel functions.

By substituting Eqs. (A.65), (A.66), (A.70) into Eq. (A.61),

$$D_3 = \varepsilon_{33}^P E_0 e^{j\cdot\omega\cdot t} + \frac{A\cdot e_{31}^P\cdot\omega}{\upsilon^P} J_0(\frac{\omega\cdot r}{\upsilon^P}) e^{j\cdot\omega\cdot t} \tag{A.74}$$

Since $$I = 2\pi\cdot\int_0^a \frac{\partial D_3}{\partial t} r dr$$

Then, $$I = j\cdot\omega\cdot\pi\cdot[\varepsilon_{33}^P E_0 a^2 + 2Ae_{31}^P a J_1(\frac{\omega\cdot a}{\upsilon^P})]e^{j\cdot\omega\cdot t} \tag{A.75}$$

Hence the impedance of a thin disc is

$$Z = \frac{V}{I} = \frac{t}{j\cdot\omega\cdot\pi\cdot a^2\varepsilon_{33}^T}[\frac{\Im(\omega\cdot a/\upsilon^P)+\sigma^P-1}{(1-k_p^2)\cdot\Im(\omega\cdot a/\upsilon^P)+\sigma^P-1+2k_p^2}] \tag{A.76}$$

From Eq. (A.76), the resonant frequencies were given by the roots of the transcendental equation

$$\Im(\omega\cdot a/\upsilon^P) = 1-\sigma^P \tag{A.77}$$

Defined η_1 which is the lowest root of Eq. (A.77), then

$$\eta_1 = 2\pi f_r a/\upsilon^P \tag{A.78}$$

where f_r is the fundamental resonant frequency of the radial mode.

Appendix B

Thinning tests of

the 1-3 PMN-PT/epoxy composite

Thickness=2.93mm

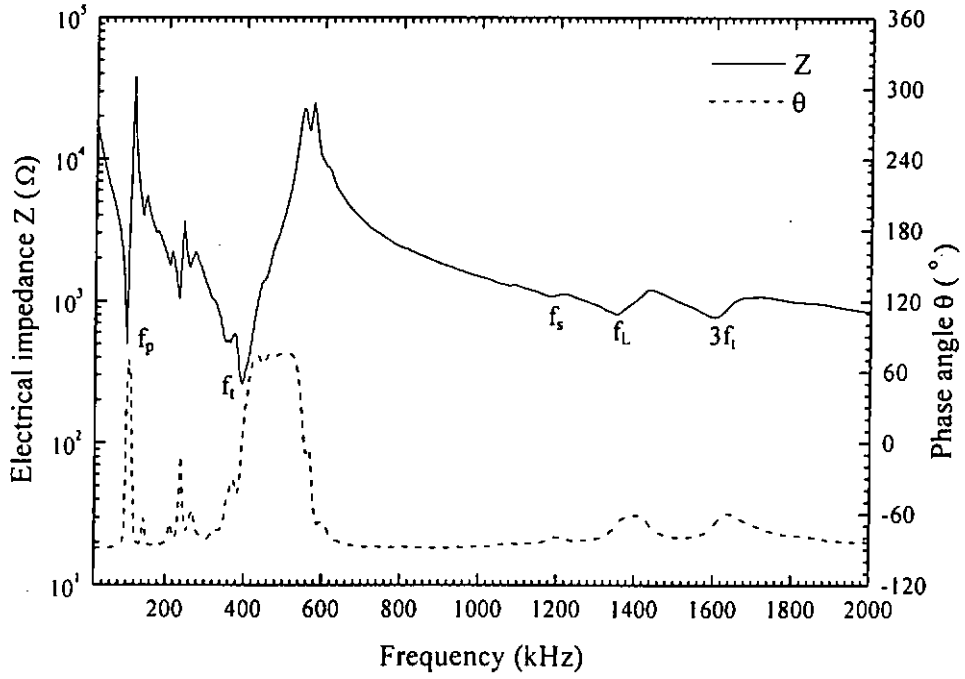

Thickness=2.71mm

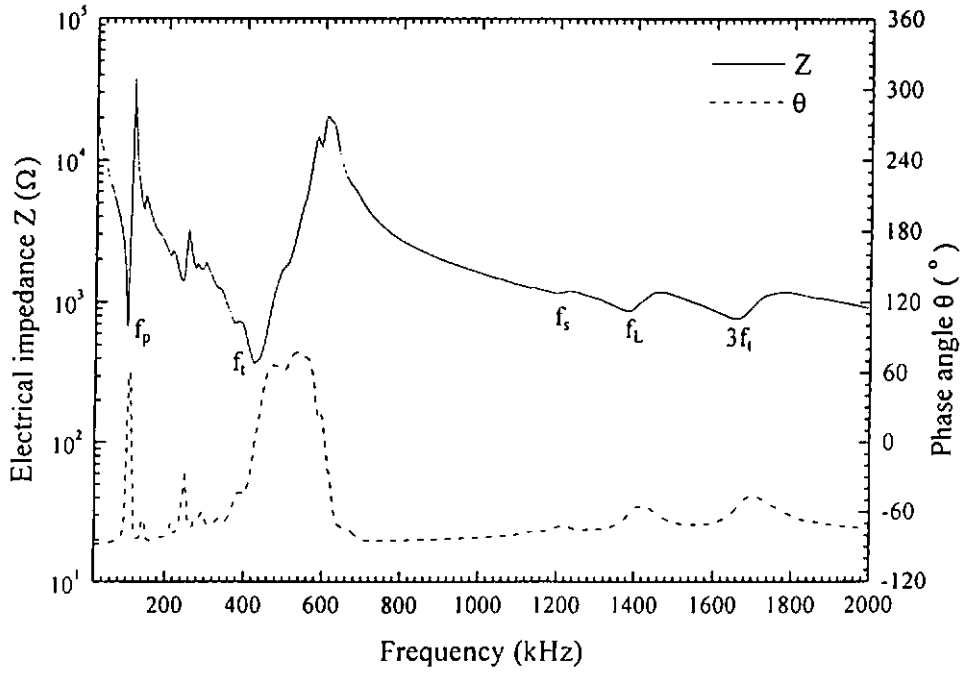

Thickness=2.43mm

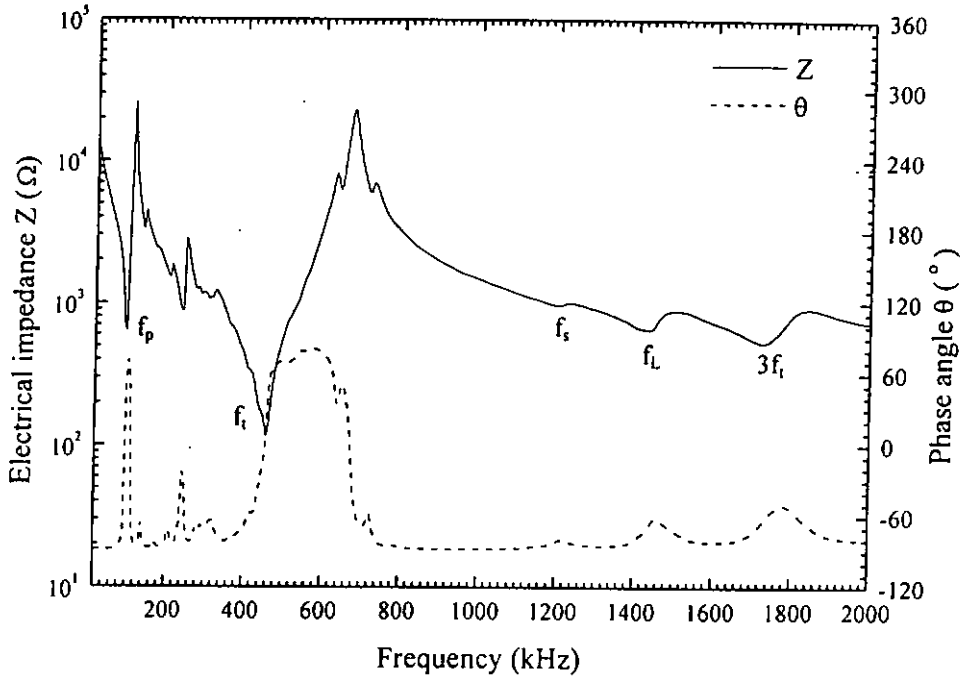

Thickness=2.24mm

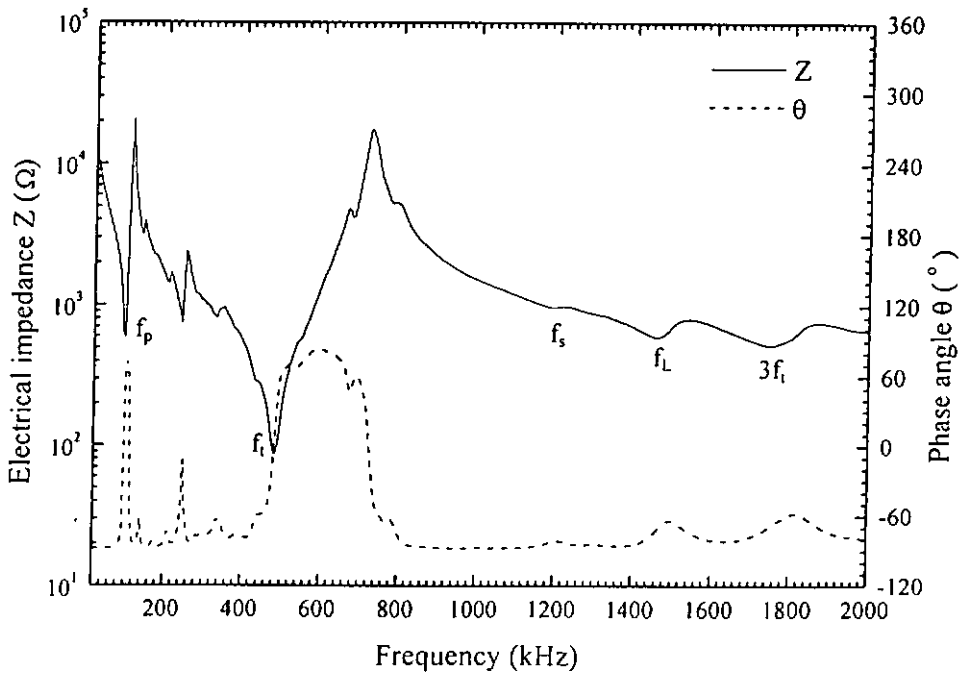

Thickness=2.12mm

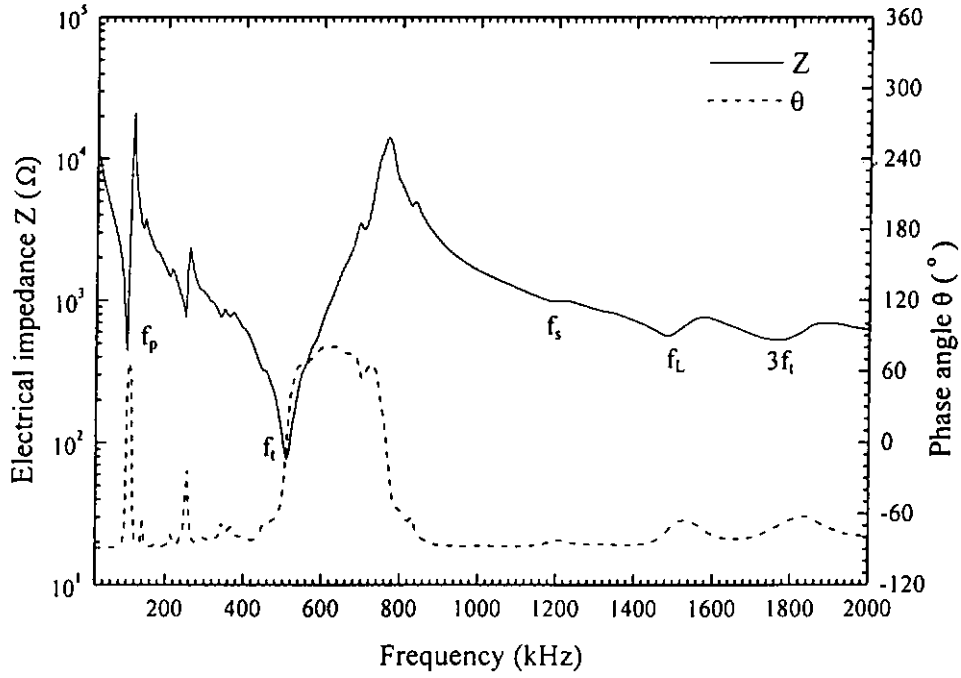

Thickness=2.09mm

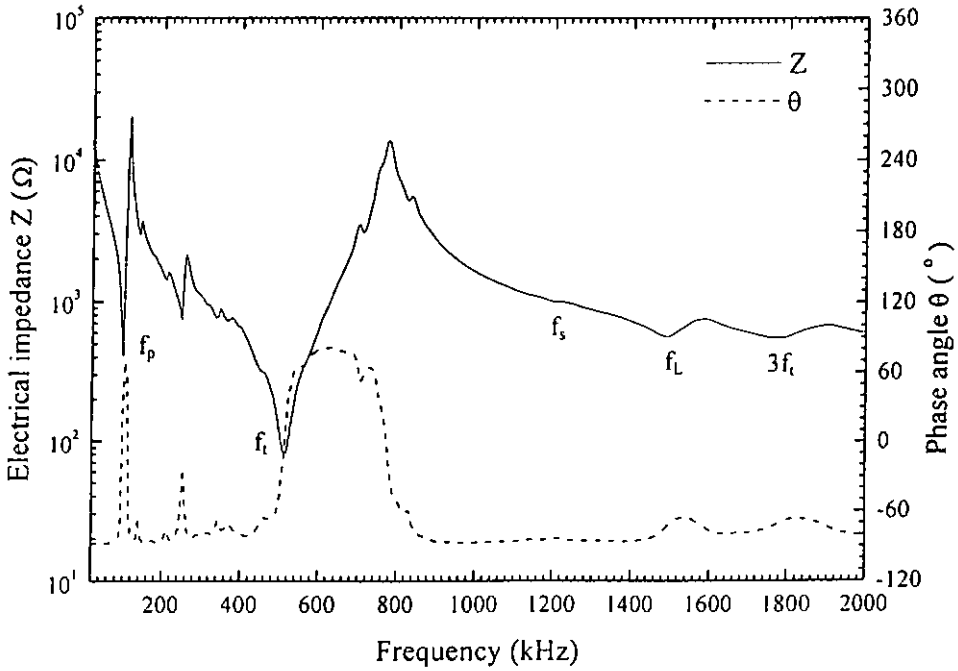

Thickness=1.99mm

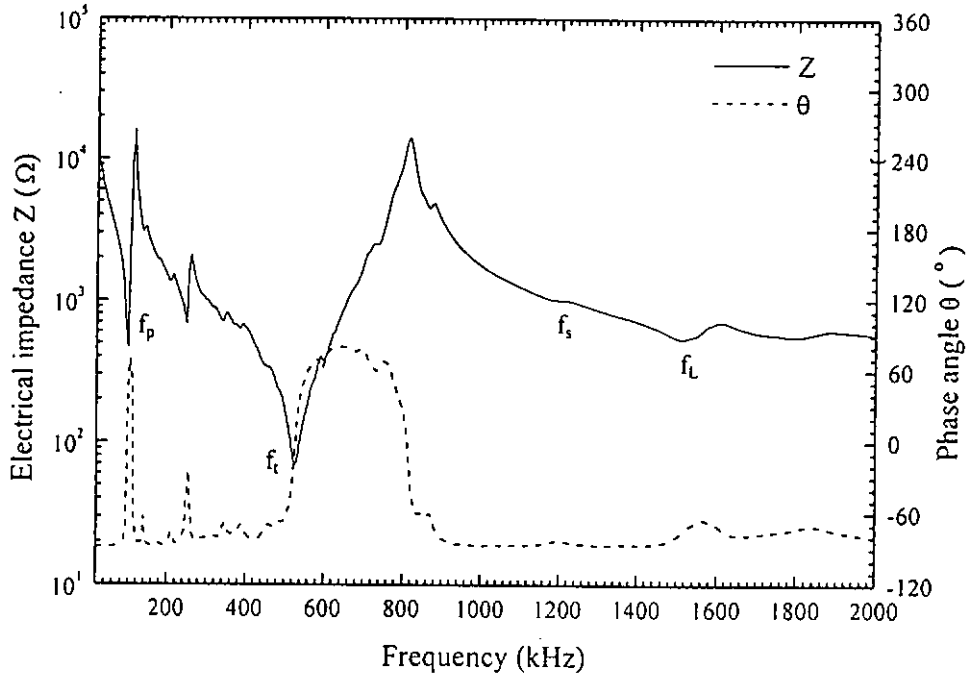

Thickness=1.89mm

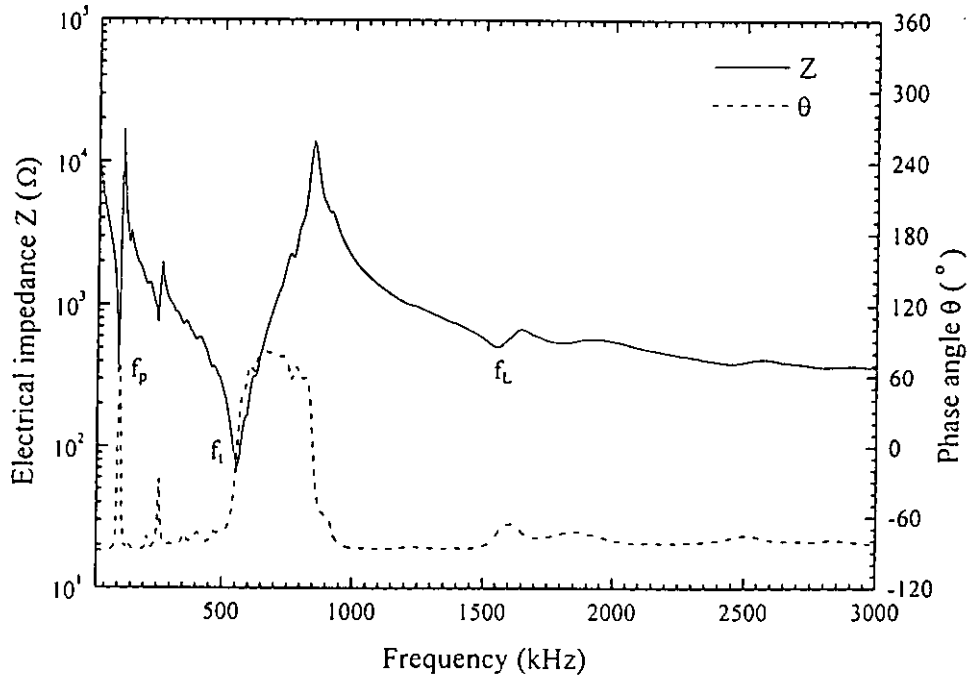

Thickness=1.78mm

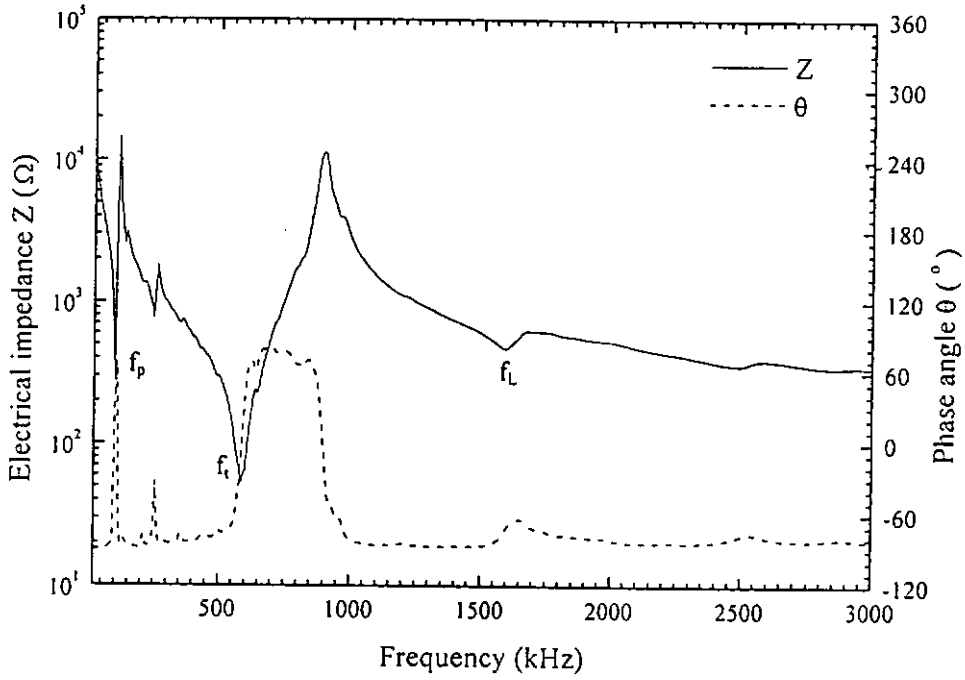

Thickness=1.69mm

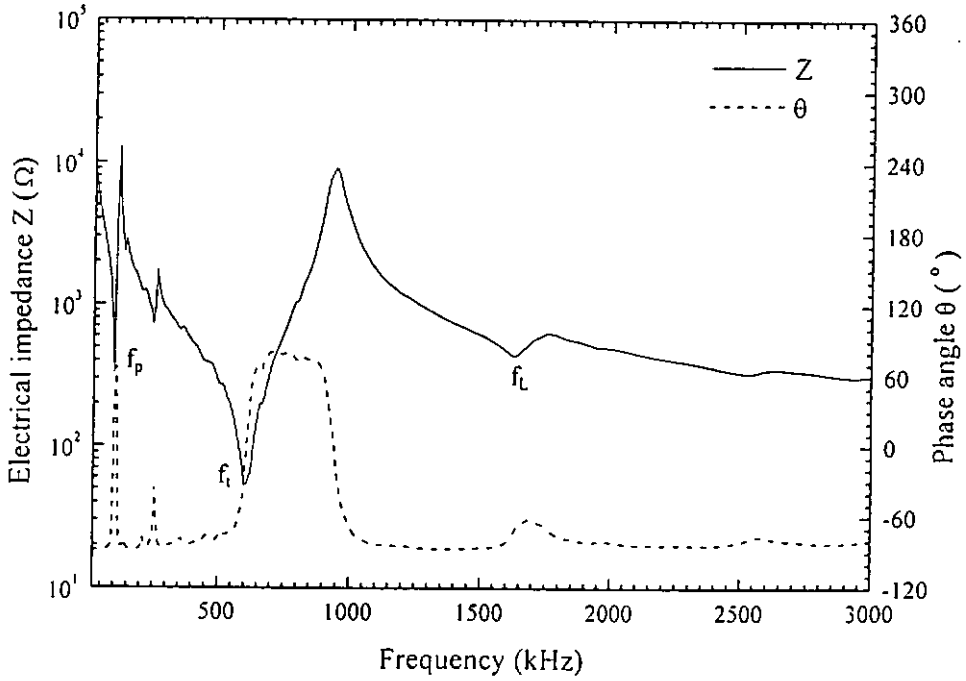

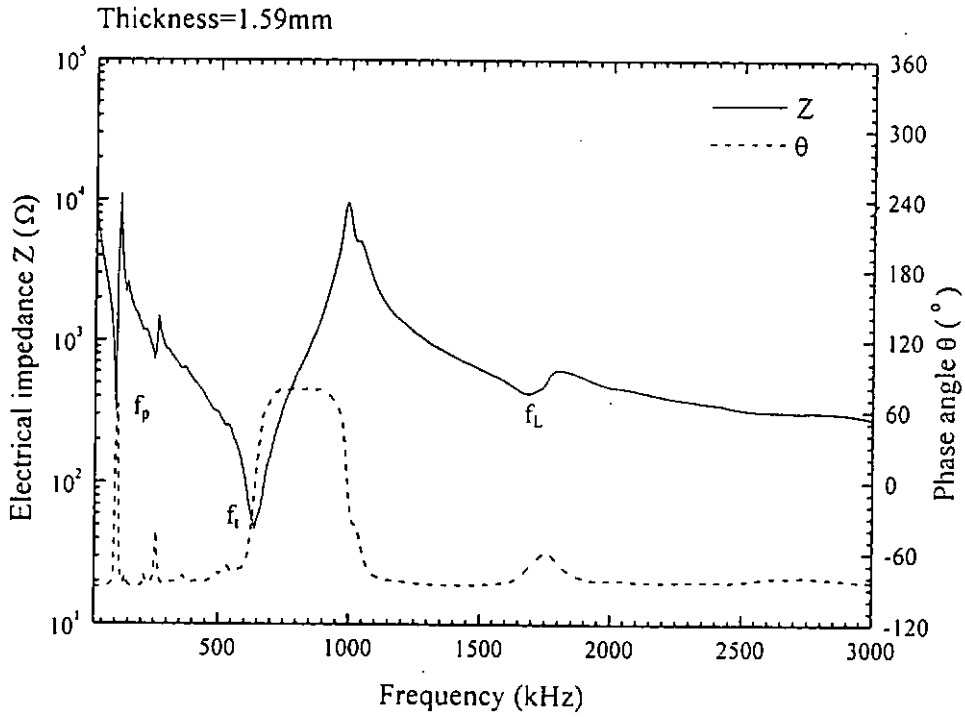
Thickness=1.59mm
Z
θ
Electrical impedance Z (Ω)
Phase angle θ (°)
Frequency (kHz)
f_p
f_t
f_L
10^5
10^4
10^3
10^2
10^1
360
300
240
180
120
60
0
-60
-120
500
1000
1500
2000
2500
3000

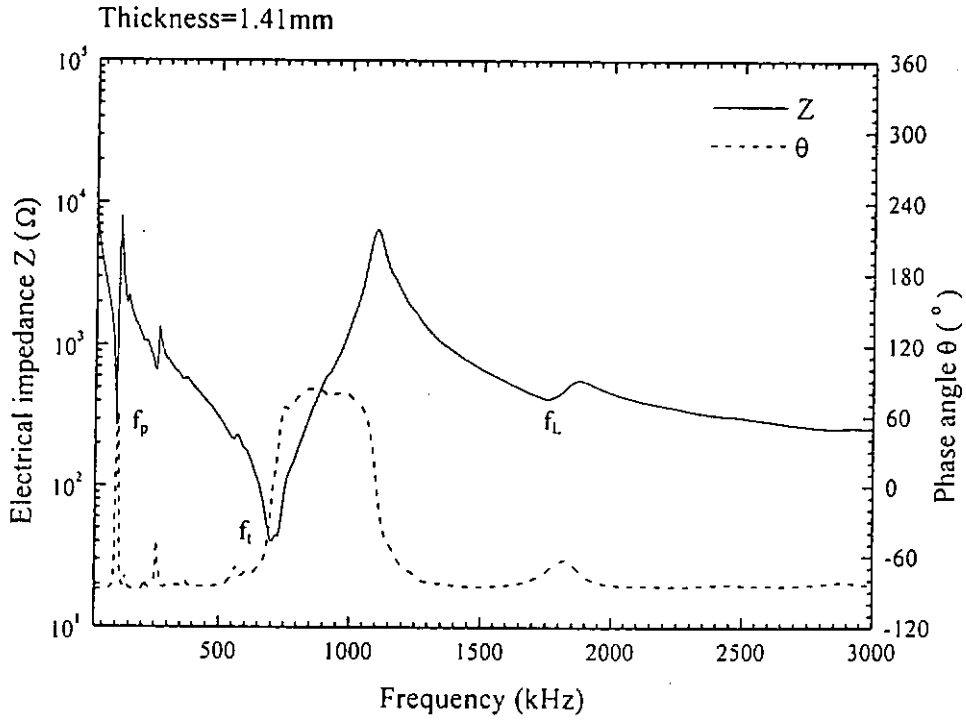
Thickness=1.41mm
Z
θ
Electrical impedance Z (Ω)
Phase angle θ (°)
Frequency (kHz)
f_p
f_t
f_L
10^5
10^4
10^3
10^2
10^1
360
300
240
180
120
60
0
-60
-120
500
1000
1500
2000
2500
3000

Thickness=1.28mm

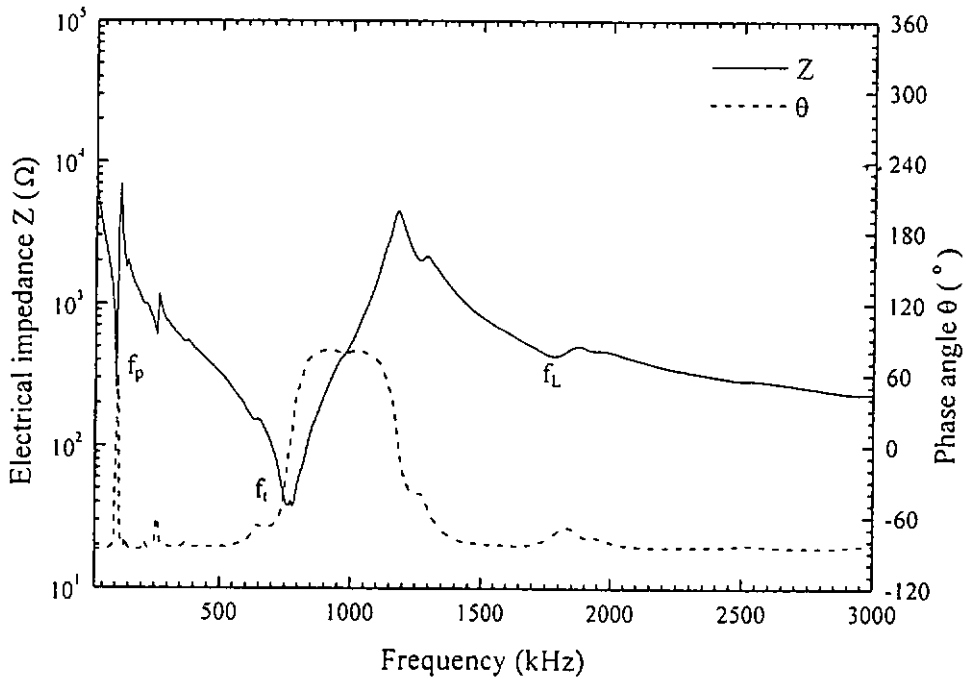

Thickness=1.18mm

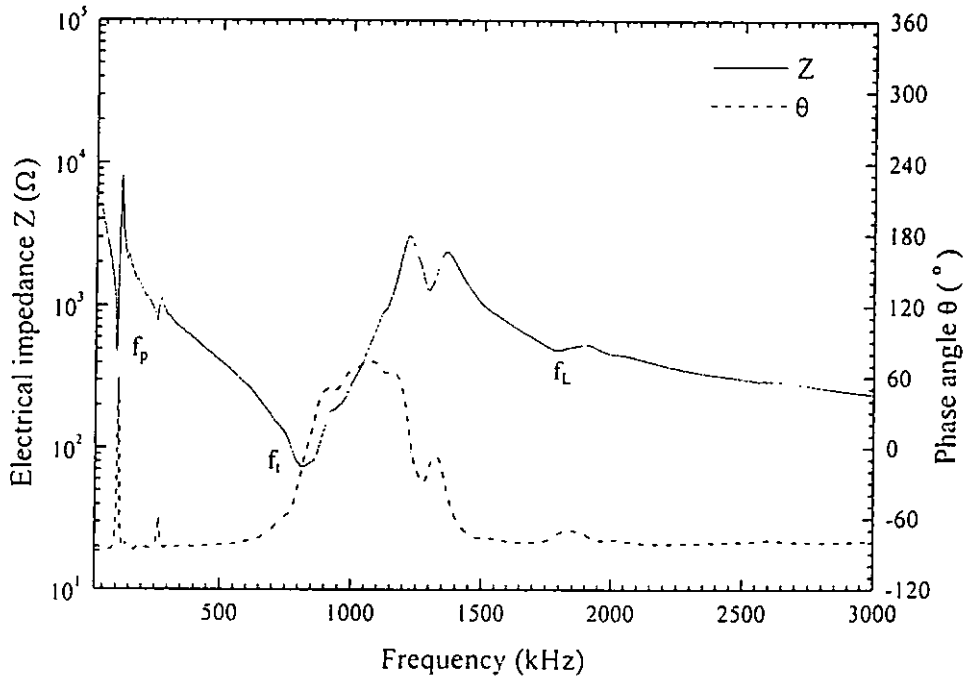

Appendix C

Thinning tests

of the PZT ring

Thickness=4.78mm

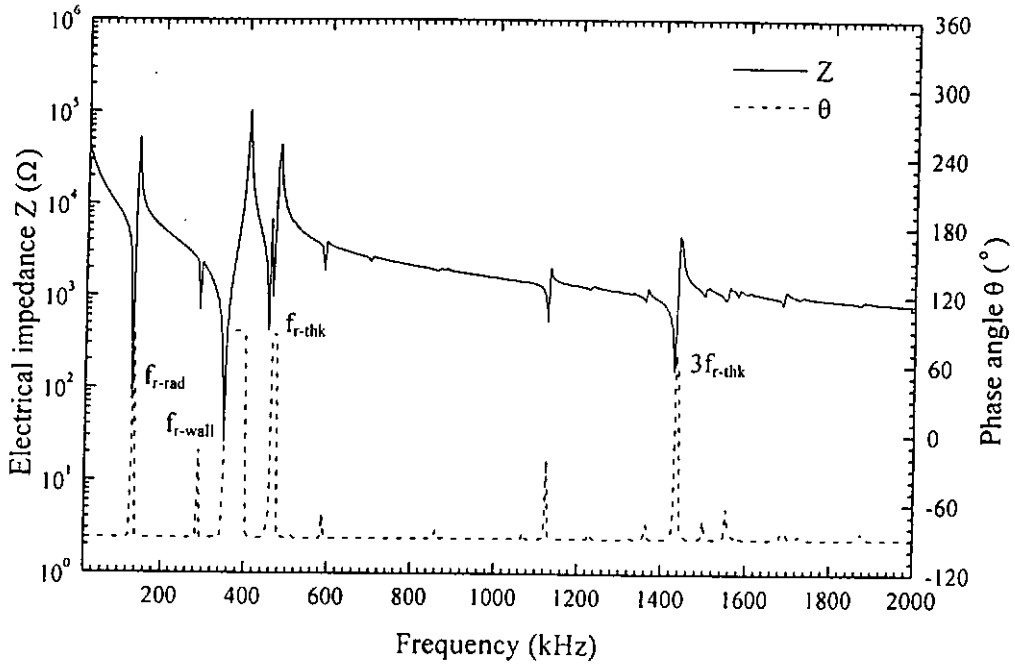

Thickness=4.33mm

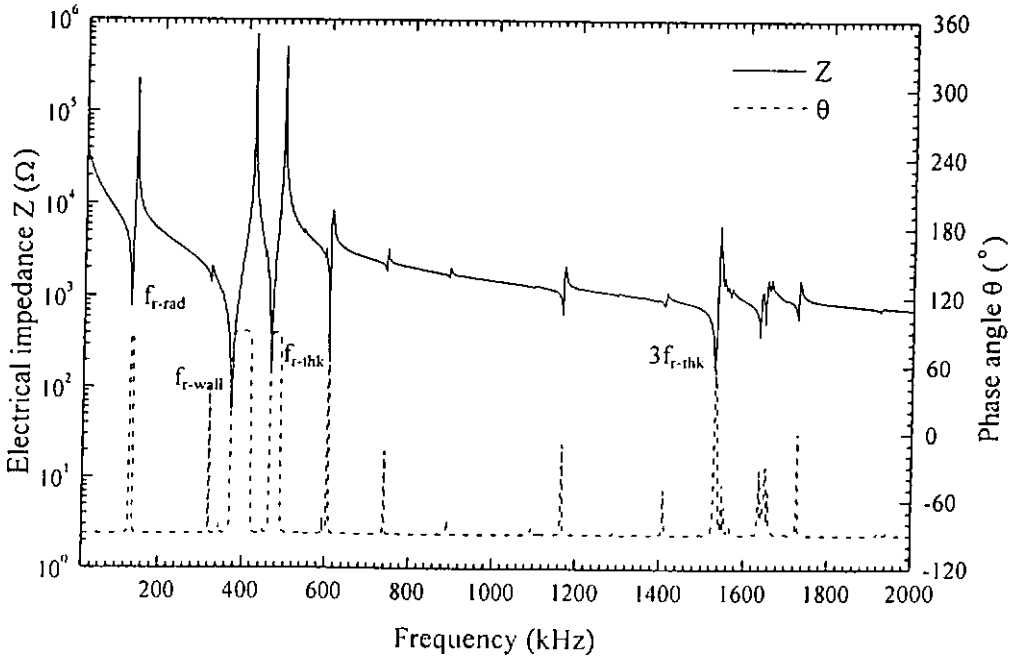

Thickness=4.16mm

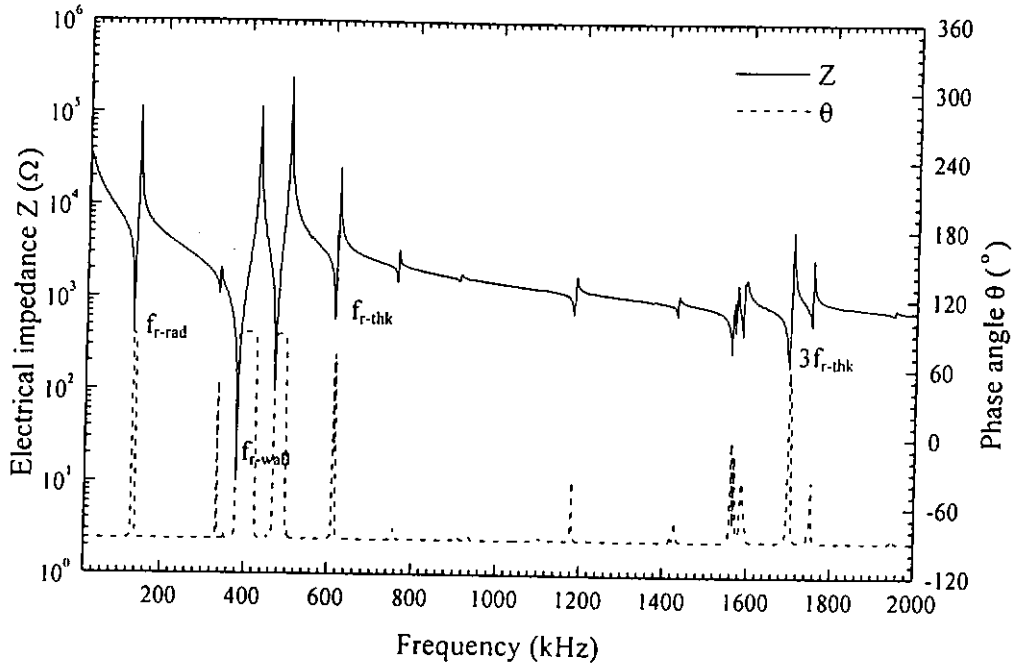

Thickness=3.92mm

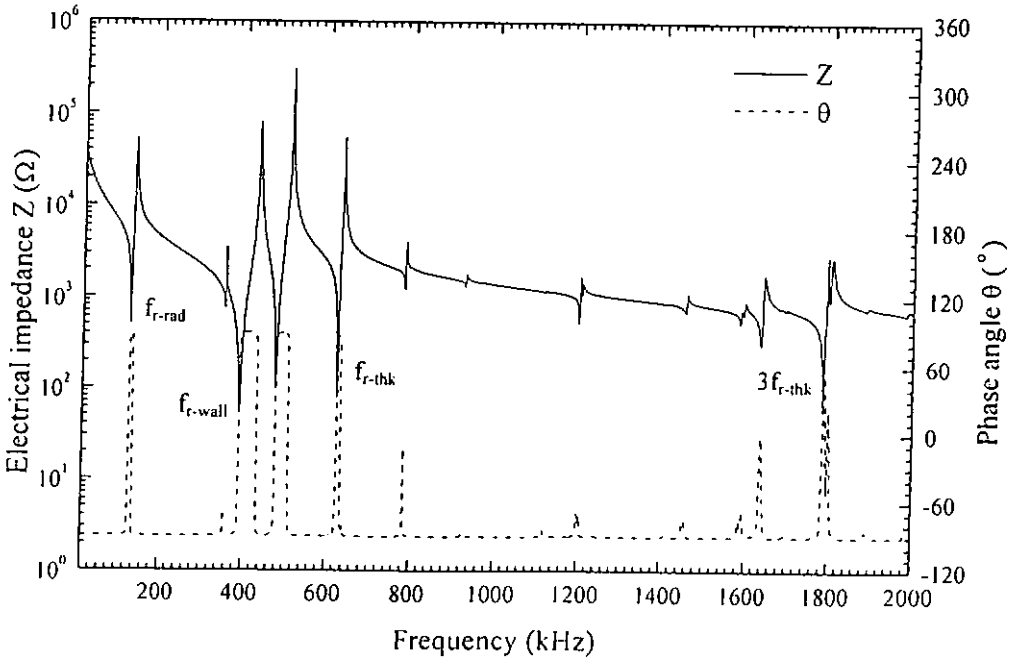

Thickness=3.77mm

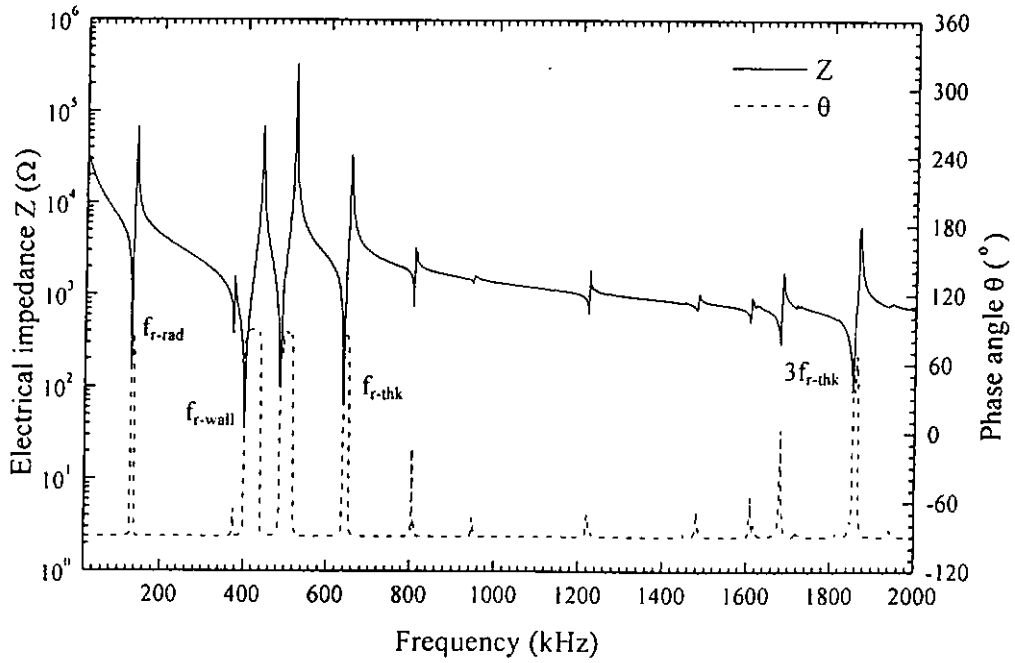

Thickness=3.59mm

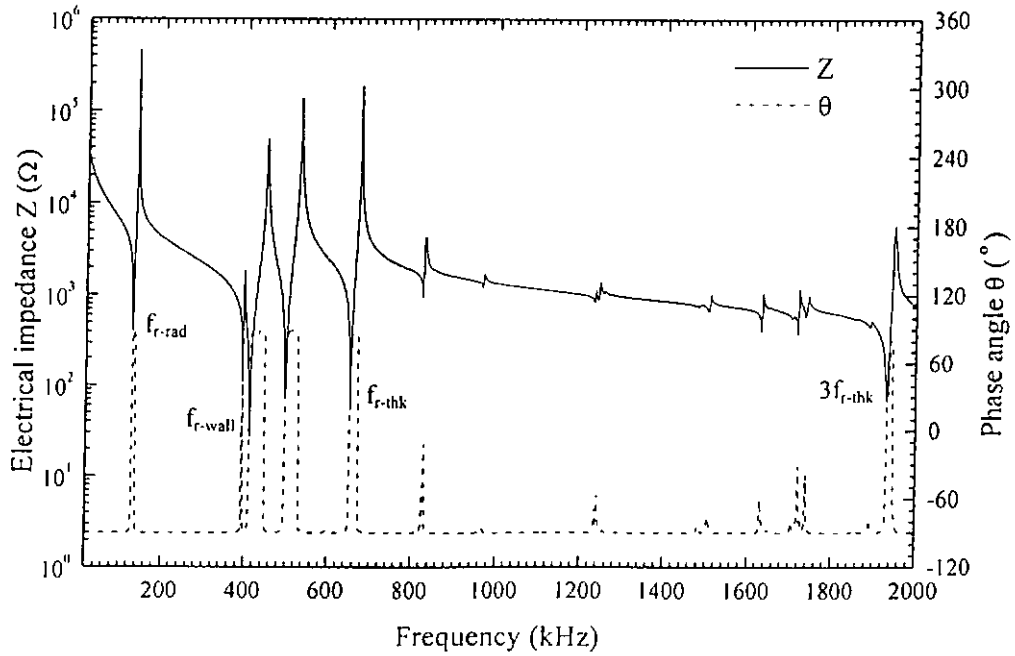

Thickness=3.35mm

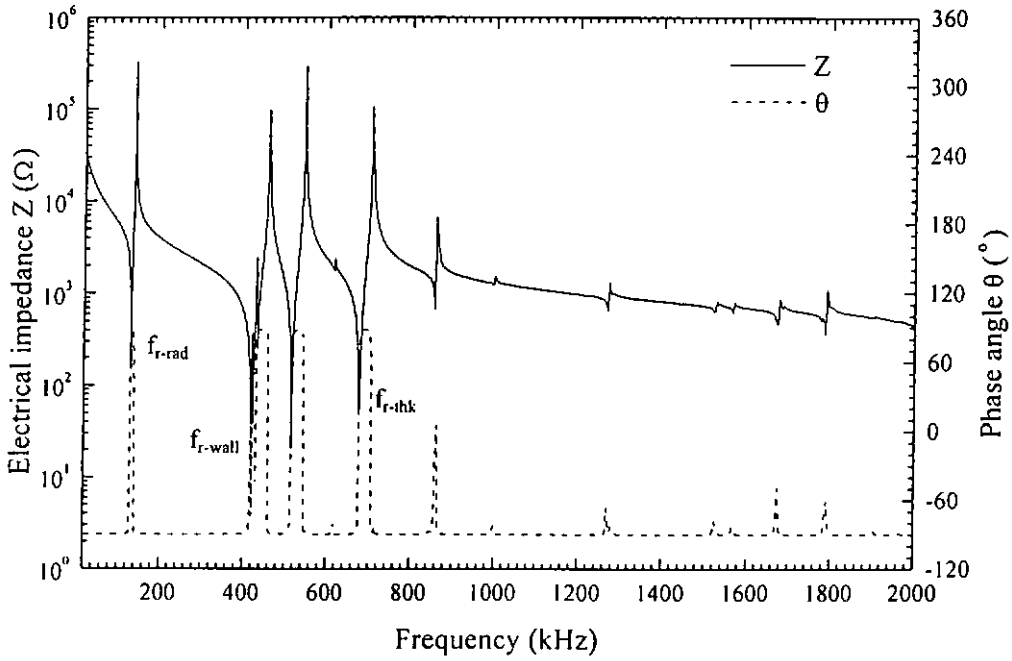

Thickness=3.11mm

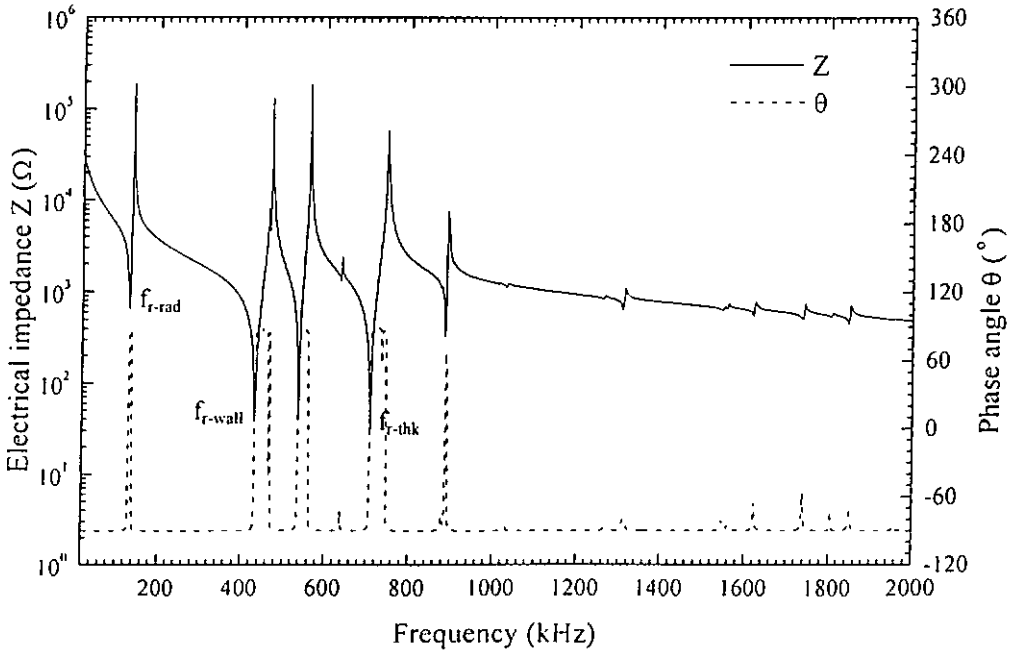

Thickness=2.90mm

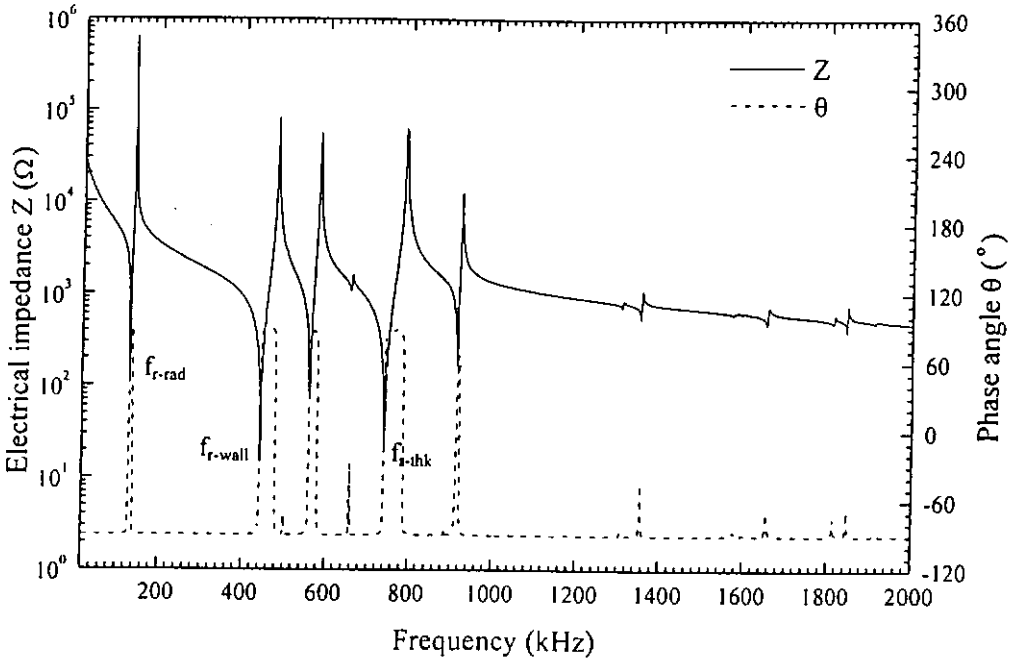

Thickness=2.72mm

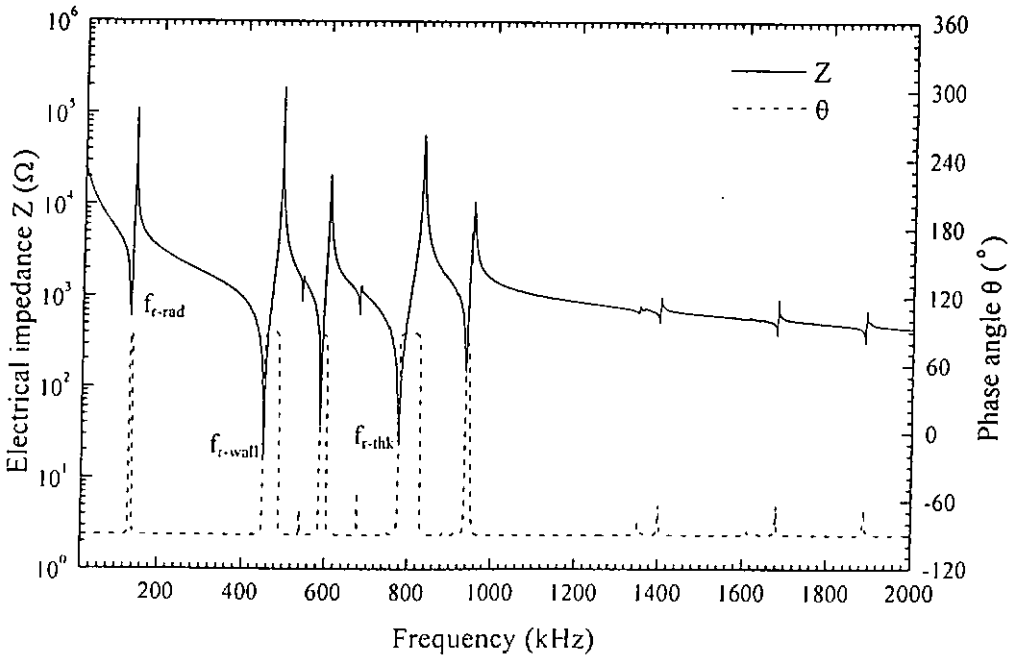

Thickness=2.52mm

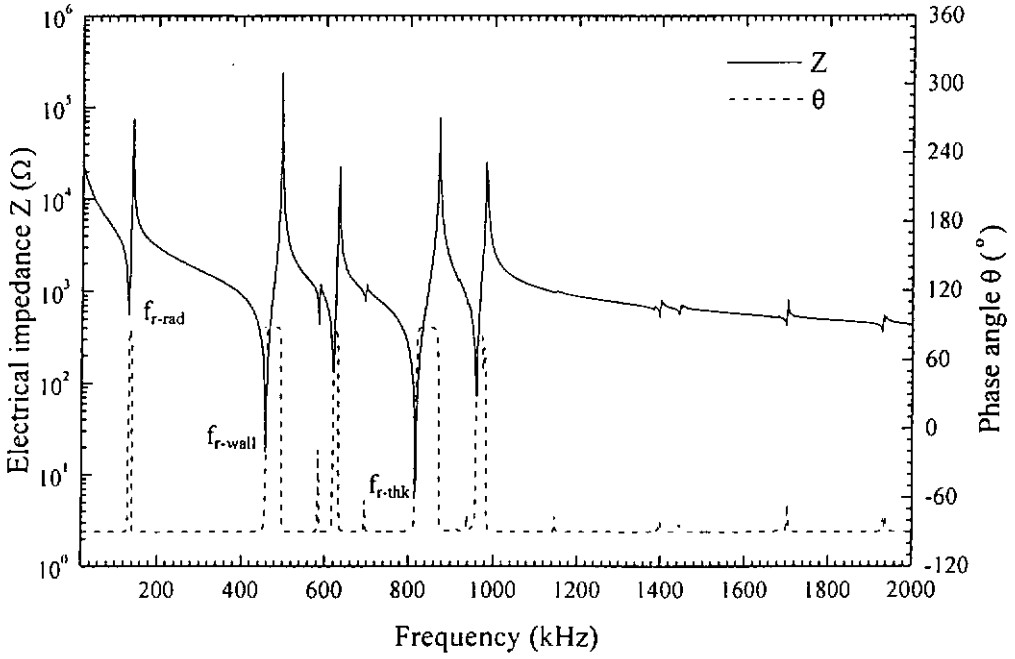

Thickness=2.47mm

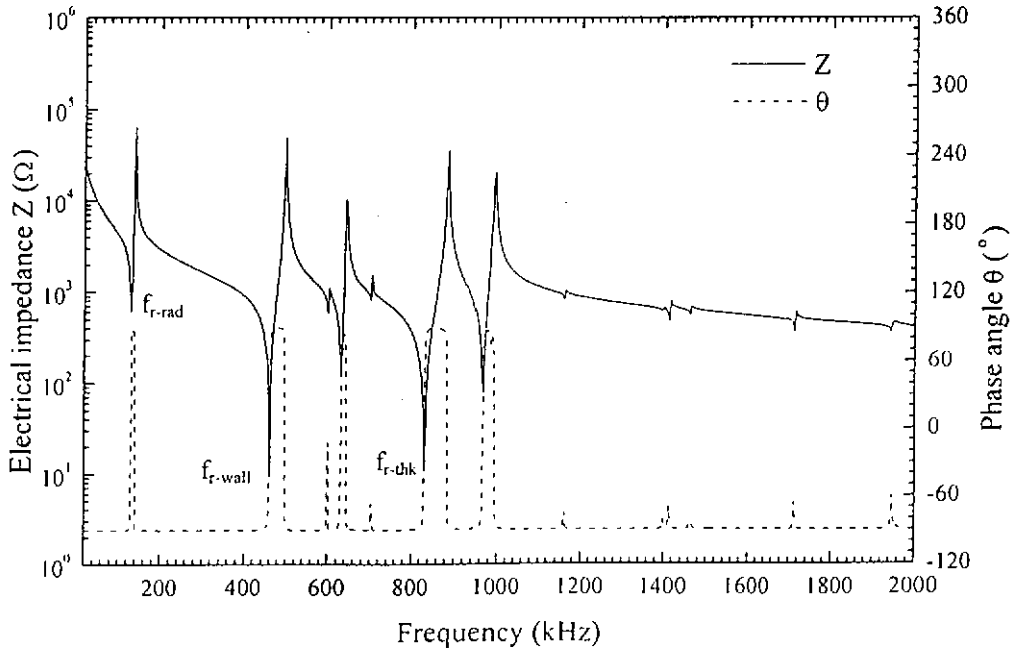

Thickness=2.27mm

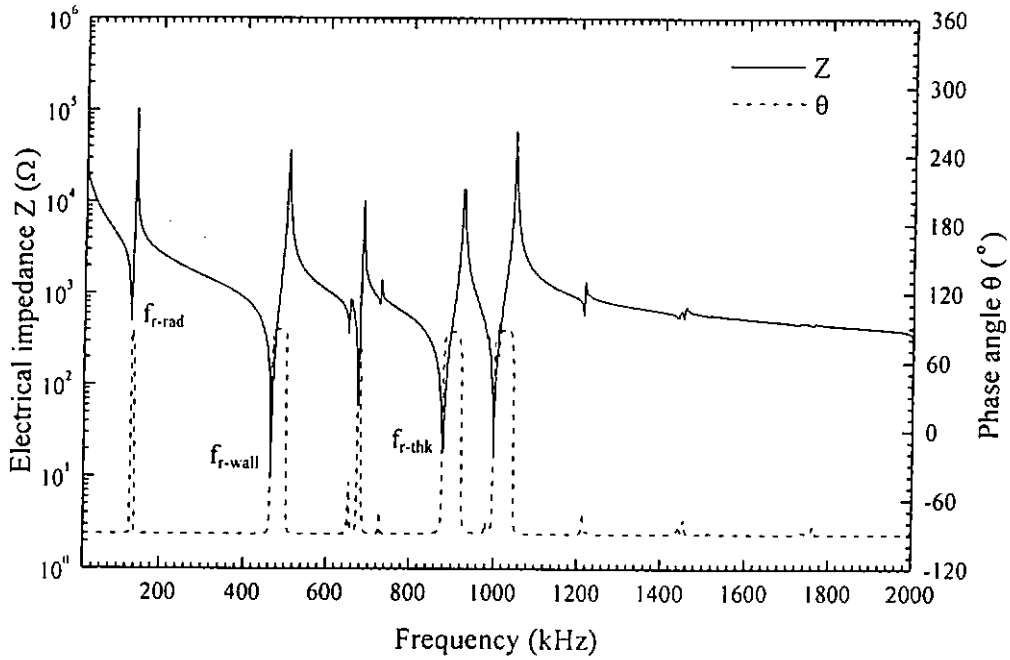

Thickness=2.04mm

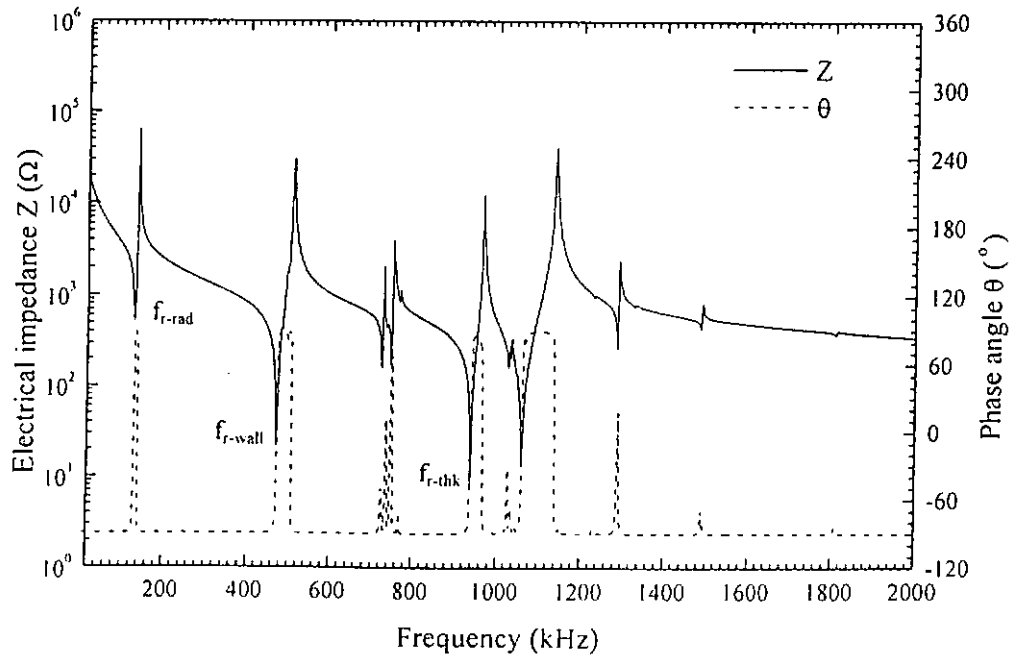

Thickness=1.78mm

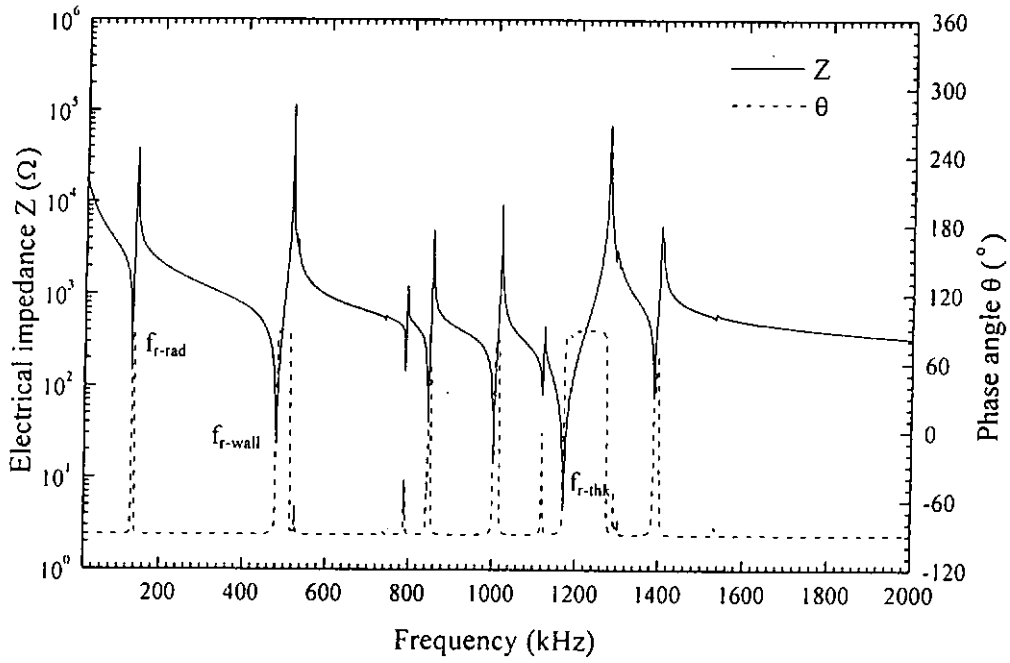

Thickness=1.56mm

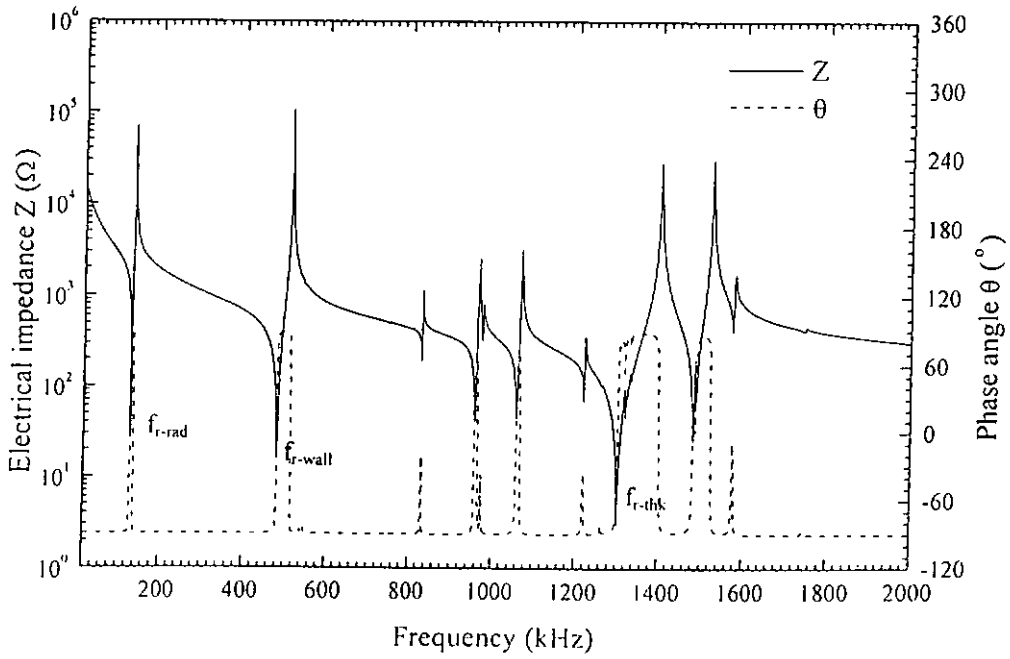

Thickness=1.29mm